WIDEBAND, DIRECTION OF ARRIVAL ESTIMATION USING SMALL-APERTURE ANTENNA ARRAYS

by

Ruyu Ma

A dissertation submitted in partial fulfillment of
the requirements for the degree of

Doctor of Philosophy

(Electrical and Computer Engineering)

at the

UNIVERSITY OF WISCONSIN–MADISON

2020

Date of final oral examination: 08/10/20

The dissertation is approved by the following members of the Final Oral Committee:
Nader Behdad, Professor, Electrical & Computer Engineering
Barry Van Veen, Professor, Electrical & Computer Engineering
Zongfu Yu, Associate Professor, Electrical & Computer Engineering
Victor Brar, Assistant Professor, Physics

For my wife Teddy Xiang.

ACKNOWLEDGMENTS

I would like to appreciate my doctoral advisor, Dr. Nader Behdad, for his valuable support and guidance in my PhD studies and in my way to a mature researcher. I would also like to appreciate my doctoral committee members, Dr. Barry Van Veen, Dr. Zongfu Yu, and Dr. Victor Brar for their helpful suggestions for improving the quality of this work.

I would like to give thanks to my friends and fellow labmates in the University of Wisconsin-Madison for their emotional support and enlightening discussions. Special thanks to Dr. Jian Dong for his guidance and encouragement.

I would like to acknowledge my sponsors. This dissertation would not have been possible without the funding from the Office of Naval Research under ONR Awards No. N00014-15-1-2207 and N00014-16-1-2098, nor that from the Army Research Office under Award No. W911NF1920273.

Finally, I would like to give my gratitude to my parents Junqun Ma and Huayun Liu for their unconditional love and support every moment of my life. Special appreciation to my wife Teddy Xiang for her irreplaceable support and love in one of the most difficulty time of my life.

CONTENTS

LIST OF TABLES

LIST OF FIGURES

ABSTRACT

The HF, VHF and UHF bands are widely used in many important civilian and military applications, direction finding (DF) systems covering these bands are of great interest in electronic warfare support applications. However, due to large wavelength in these frequency bands, practical antennas are usually electrically small and have limited bandwidth, especially when they are deployed on moving platforms with very limited space to accommodate them. What's worse, the small aperture also set a physical limitation on the accuracy of direction of arrival (DoA) estimation. This dissertation investigates four approaches to develop small-aperture antenna arrays with enhanced bandwidth and DoA estimation accuracy. The first approach focuses on optimizing the antenna structure and array geometry. I examined different array topologies and adopted the one that provides the lowest Cramer-Rao bound (CRB) and both azimuth and elevation DoA capability, and then, further optimize it to efficiently utilize an available volume. The second approach relies on selecting and exciting a group of the platform's characteristic modes (CMs) that provides the lowest CRB. The antennas are placed at multiple locations on the platform for the best excitation of the CMs. The third approach further brings the antennas to a single location on the platform. Multiple CMs can still be excited and enable the spatically-confined array to achieve DF accuracy better than the theoretical limit of standalone array. The last approach explores a compact, wideband array with multiple independent beams and vertical polarization that is suitable for both directional networking and DoA estimation applications. Finally, I discuss possible future works that are important to developing wideband, direction of arrival estimation systems using small-aperture antenna arrays.

1 INTRODUCTION

Radio direction-of-arrival (DoA) estimation (or direction finding) systems measure the directions of incoming electromagnetic waves by using collected or displaced antennas with identical or diverse radiation patterns to pickup the electromagnetic waves. Knowing the direction of incoming waves is extremely important in many military and civilian applications, such as radar interferometers, surveillance, navigation, maritime communications, and 4th and 5th generation of cellular mobile communications among others. However, some challenging requirements have been put on the antennas used in direction finding (DF) applications. For example, wideband antennas are usually preferred, as users or DF systems do not want to miss signals because of the limited bandwidth of the antennas. Moreover, small-aperture antennas are usually necessary from the practical point of view, especially when the operating frequency goes down to HF and VHF bands, due to the large wavelength of electromagnetic waves in these bands (1 – 100 m).

1.1 General Considerations of Direction-of-Arrival Estimation

The ultimate goal of a direction finding (DF) system is to estimate the direction of arrival (DoA) as accurately as possible. However, there are some other design considerations that are important in practical applications. These considerations include the field of view (FoV), the number of signals that the system can detect simultaneously, bandwidth, polarization and other feature of the signals, aperture size, number of receivers, and cost among others.

The accuracy and resolution of DoA estimation are two critical features of a DF system. The term accuracy refers to how close the estimated DoA of a received signal is to the real DoA. Resolution quantifies the minimum separation needed between two impinging signals that the system can unambiguously detect. The DoA estimation accuracy and resolution usually depends on the aperture size, antenna/array architecture, signal-to-noise ratio (SNR), and DF method. In general, using larger aperture sizes and having higher SNR improves both accuracy and resolution.

FoV refers to the angular region over which the DF system performs DoA estimation. This region, depending on the application, may be a one-dimensional plane (e.g. azimuth plane), a portion of sphere defined by a solid angle less than 2π, an entire hemisphere (2π solid angle), or the whole sphere (4π solid angle).

The number of signals that a DF system can simultaneously detect and the signals' features (e.g. polarization and correlation) put additional requirements on resolution, aperture size, number and types of receivers, and post-processing methods. The number of coherent receivers needed in each system and the complexity of post-processing algorithm may strongly impact the cost of a DF system. A DF system may be as simple as a yagi-uda antenna connected to a diode detector used in fox hunting[1] by amateur radio operators or as complex as a large antenna array in which each element is connected to a coherent receiver used in military surveillance and tracking.

1.2 Direction Finding Techniques and Systems

The radio DF dates back to 1888 when Heinrich Hertz discovered the directional characteristics of loop antennas (Travers and Hixon, 1966). In 1902, Stone proposed a method of acquiring DoA by rotating an antenna with a figure-eight shaped radiation pattern (Travers and Hixon, 1966). Since then, a number of methods based on magnitude, phase and time difference of the signals received at different elements of the DF antenna array have been proposed and thoroughly investigated. These methods include Watson-Watt/Adcock method, Doppoler method, time difference of arrival (TDOA) method, sum-difference method, and array-based methods including those using vector sensor(s). Fig. 1.1 shows a comparison

---

[1] Fox hunting is a term used in amateur radio and refers to using DF antennas to determine the location of a hidden transmitter.

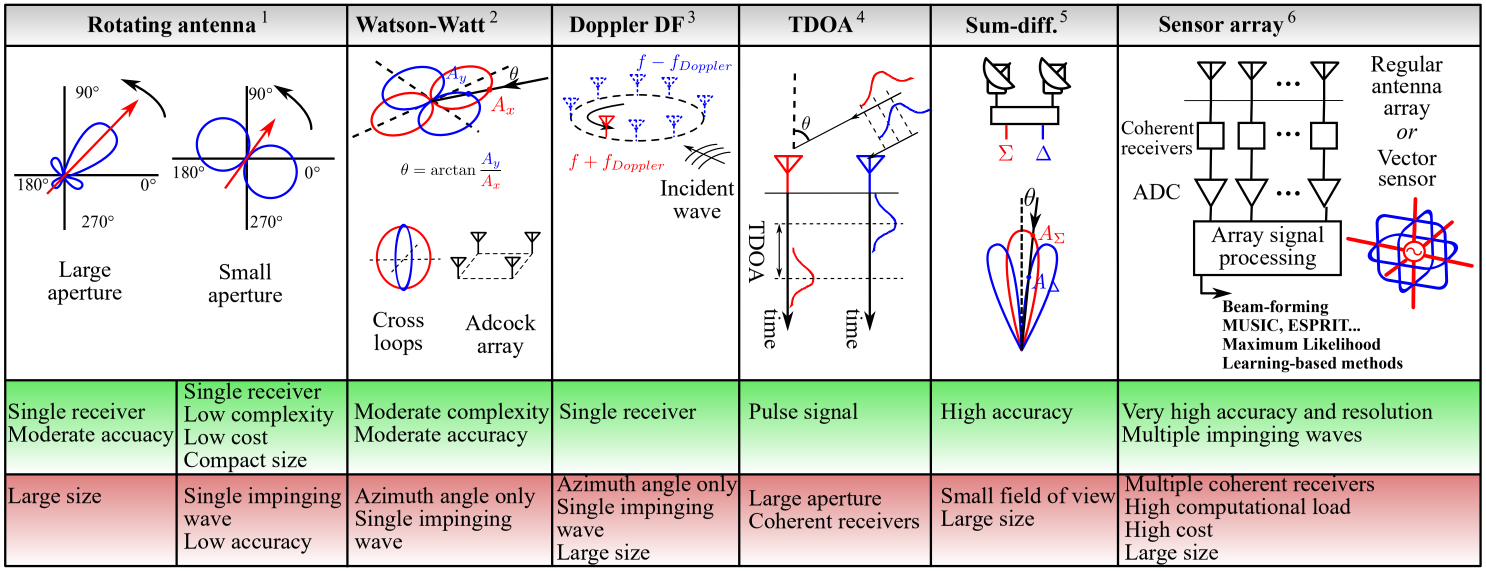

Rotating antenna[1]		**Watson-Watt**[2]	**Doppler DF**[3]	**TDOA**[4]	**Sum-diff.**[5]	**Sensor array**[6]
Single receiver Moderate accuacy	Single receiver Low complexity Low cost Compact size	Moderate complexity Moderate accuracy	Single receiver	Pulse signal	High accuracy	Very high accuracy and resolution Multiple impinging waves
Large size	Single impinging wave Low accuracy	Azimuth angle only Single impinging wave	Azimuth angle only Single impinging wave Large size	Large aperture Coherent receivers	Small field of view Large size	Multiple coherent receivers High computational load High cost Large size

Figure 1.1: figure

A graphical comparison of a number of commonly-used direction finding techniques and systems.

1. Jenkins (1991)
2. Jenkins (1991); Kratschmer (2010)
3. Steiner (1960); Peavey and Ogumfunmi (1997)
4. Carter (1993); Jenkins (1991)
5. Holder (2014); Kratschmer (2010)
6. Zoltowski and Wong (2000); Wong and Zoltowski (2000); Krim and Viberg (1996); Haykin and Liu (2010); Van Veen and Buckley (1988); Drosopoulos and Haykin (1992); Rissanen (1978); Schwarz et al. (1978); Akaike (1974); Schmidt (1986); Roy and Kailath (1989); Chen et al. (2010); Alrmah et al. (2011); Barabell (1983); Li and Compton (1991); Ferrara and Parks (1983); Du et al. (2002); Shieh and Lin (2000); Ma and Teng (1999)

between these different techniques and provides a high-level overview of their attributes.

Rotating Antenna Method

Rotating a directional antenna and measuring the magnitude of the received signal is among the earliest reported DF techniques (Travers and Hixon, 1966; Jenkins, 1991). The antenna can be rotated manually, mechanically or its pattern can be rotated electronically. One possible way to implement such antennas is to use electronically steerable parasitic array radiator antennas (Preston et al., 1998; Schlub and Thiel, 2004; Sun et al., 2004; Plapous et al., 2004; Taillefer et al., 2005, 2008). These ESPAR antennas steer the radiation pattern via shortening and opening parasitic elements. The rotating antenna methods are usually low-cost and used to find DoA of the signal in the azimuth plane. The bandwidth of this technique depend on the implementation technique. For example, DF systems using ESPAR antennas have usually narrow bandwidths (10-15%) but a mechanically rotated aperture antenna can have a very wide bandwidth.

Watson-Watt Method

Watson-Watt method is another magnitude-based DF method. This method needs two cross loops connected to two (non-coherent) receivers or a single receiver switched between the two loops. By measuring the ratio of the signal magnitudes collected by these loops, DoA can be conveniently estimated. Details of this technique can be found in many books and papers written by, e.g., Jenkins (1991) and Kratschmer (2010). An alternative antenna array used for this method is the Adcock array (Guy and Davies, 1983; Henault et al., 2008). This array is a four-element rectangular array composed of dipoles/monopoles. If the diagonal elements are fed with a phase difference of 180°, the Adcock array provides the required orthogonal figure-eight shaped patterns. This method is suitable for azimuth only DF purposes. The cross loops can be electrically small but are usually narrow band, whereas the Adcock array's diagonal elements are usually separated with about a quarter to a half wavelength. Moreover, using dipoles/monopoles to generate the figure-eight shaped radiation patterns offers better polarization purity particularly for signals with high elevation angles.

Doppler Direction Finder

When an antenna is moving while receiving a signal, the received signal experiences a Doppler shift based on the relative orientation of the movement of the antenna and the direction of arrival of the electromagnetic wave. Doppler shift is maximum if the antenna is moving towards (or away from) the direction of arrival of the signal and is zero if it is moving orthogonal to it. If the antenna is moved around a circle when it is illuminated by a plane wave, the received signal will become frequency modulated due to the Doppler shift. By detecting this variation of the Doppler shift and correlating that to the location of the antenna along the circle, DoA is determined. In general, rather than physically rotating one antenna along a circle, a uniform circular array is used and the elements are sequentially sampled around the array. This method is referred to as the pseudo-Doppler method. This electronic switching simplifies some of the challenges involved in mechanically rotating an antenna around a circle and also allows for faster electronic rotations. The FoV of this method is usually the entire azimuth plane. Doppler direction finders generally have dimensions in the order of a couple of wavelength. This is due to the fact that the Doppler shift is proportional to the diameter of the circle that the antenna moves around. Details of these methods have been thoroughly discussed by Jenkins (1991); Kratschmer (2010); Steiner (1960); Peavey and Ogumfunmi (1997).

Time Difference of Arrival (TDOA) Method

Measuring the time difference of arrival (TDOA) of signals at the elements of an antenna array is another DF method. This method is usually used for pulse signals, and uses antenna arrays with long baselines. Higher TDOA accuracy requires a longer baseline and narrower pulses, which have wider bandwidth. Therefore, the TDOA method requires wideband antennas (Holder, 2014). If the waveform of these pulses is known a priori (e.g. monopulse radar), matched filters can be used to compress the pulses' widths and increase the TDOA accuracy. At the same time, this filtering further requires antennas with stable phase centers and little dispersion, so that the waveform is not distorted. Details of this method have been reported by Carter (1993); Holder (2014); Jenkins (1991).

Sum-difference Method

The sum-difference method is another DF method generally used for precise tracking of a signal in a narrow FoV. A common setup used in this method is composed of two high-gain antennas pointing towards the same direction. The distance between these antennas is usually several wavelength or more. As a result, the difference pattern of the antennas has a very sharp null in the center of its main lobe, whereas the sum pattern is still a pencil-beam pattern. By comparing the amplitudes of the sum and difference signals, the DoA can be estimated very precisely so long as the signal is within the main beam of the sum pattern. The array factor of the difference pattern may have more than one sharp null within its FoV (based on the spacing between the elements). However, this is usually not a major issue as each antenna has a high gain (narrow beam width) in which case only the null towards broadside will matter. The sum-difference method is widely used in monopulse radar and other radar interferometers for tracking purposes (Holder, 2014; Kratschmer, 2010). This method comes with a rather small FoV but has a very high accuracy.

Sensor Array Method

The above mentioned methods use relatively simple DF algorithms and need to use either one or a few receivers. Moreover, some of these techniques can be implemented at a relatively low cost and used to design compact and wideband DF systems. However, they come with limited DoA estimation accuracy (Guy and Davies, 1983; Henault et al., 2008; Steiner, 1960; Peavey and Ogumfunmi, 1997; Jenkins, 1991) and/or FoV (Holder, 2014), lack multiple signal detection capability (Steiner, 1960; Peavey and Ogumfunmi, 1997; Kratschmer, 2010; Carter, 1993), or are vulnerable to cross polarization (e.g. cross loops with Watson-watt method) (Jenkins, 1991). The most sophisticated direction finding techniques use antenna arrays consisting of numerous elements, each connected to a dedicated channel of a multi-channel coherent receiver. The array may be composed of identical or diverse antenna elements. The elements may also be collocated or scattered. Vector sensors are a spacial case of arrays used for direction finding. A vector sensor array consists of six collocated antennas, each of them detecting one component of the electric or the magnetic field of the impinging waves (Wong and Zoltowski, 2000; Zoltowski and Wong, 2000). By determining the directions of the vectors of the electric and magnetic field of the wave, the wave's direction of arrival can be calculated.

DF techniques that use sensor arrays usually use advanced array signal processing techniques in performing DoA estimation. These array-based DF techniques usually need electrically large apertures, many individual antennas and coherent receivers, high speed analog to digital converters (ADCs), and intensive computational resources. As a result, the cost and complexity of these systems are very high. As the development of active phased arrays has progressed (Krim and Viberg, 1996; Haykin and Liu, 2010), array-based DF techniques have also received a lot of attention in recent decades.

Intensive research has been done on processing the data acquired by DF antenna arrays. This signal processing area is named array signal processing or spatial spectrum estimation. Comprehensive reviews have been done by Krim and Viberg (1996); Haykin and Liu (2010), their references, as well as many other books and papers on this topic. The post-processing methods are usually divided into two categories of non-parametric and parametric methods.

Non-parametric methods (e.g. Bartlett beamformer, Capon's method (Van Veen and Buckley, 1988; Drosopoulos and Haykin, 1992)) are fundamentally beamforming or filter bank methods. Such a method linearly combines the signals received at the sensors to generate constructive interference only in a given direction. The combination coefficient is termed as beamformer or (spatial) filter. The signals received at the sensors are combined with a bank of beamformers "looking" at different directions. The combination will have a peak when there is a wave coming from the direction that the beamformer “looks” at. The non-parametric methods have a resolution limit given by the conventional diffraction limit, whereas the parametric methods are able to surpass this limit with the help of high SNR and/or by increasing the number of observations. The parametric methods start with a parametric statistical model. These parameters may include the number of impinging signals (named model order), DoA and polarization. The goal is to estimate these parameters with observations collected at the antenna ports. Among these parameters, minimum description length (MDL) (Rissanen, 1978; Schwarz et al., 1978) and Akaike information criterion (AIC) (Akaike, 1974) are commonly used to estimate the model order. To estimate the DoA and polarization, subspace and maximum likelihood estimation methods are commonly used. Popular subspace methods include multiple-signal classification (MUSIC) (Schmidt, 1986), estimation of signal parameters via rotational invariance techniques (ESPRIT) (Roy and Kailath, 1989; Chen et al., 2010), and their variations (Zoltowski et al., 1996; Ramos et al., 1999; Alrmah et al., 2011; Barabell, 1983; Li and Compton, 1991; Ferrara and Parks, 1983). MLE methods (e.g deterministic MLE and stochastic MLE) have better performance than subspace-based methods, especially when multiple coherent signals are received simultaneously (Krim and Viberg, 1996). However, these advantages come at the price of heavy computational load (D-dimensional search, where D denotes number of impinging waves), whereas subspace-based methods always require one-dimensional search.

Wideband DoA Estimation Methods

Wideband direction finding has many important surveillance and military applications. For example, UWB noise radar (Wolff, 2017; Garmatyuk and Narayanan, 2002) may provide high resolution while maintains low probability of detection (LPD). Wideband DF methods include rotating broadband antennas (Bailey et al., 2012; Liang and Chia, 2001), TDOA (Carter, 1993), and sensor array method with special broadband DoA estimation algorithms (Liberal et al., 2011; Chandran, 2005). Watson-Watt and sum-difference method can also be used for wideband cases if the radiation patterns of the DF antennas arrays are designed to be consistent over the entire bandwidth.

The array elements used in wideband DF systems are either broadband antennas or narrow-band antennas that can be tuned over a wide bandwidth. In rotating antenna and sensor array methods, the DF systems equipped with broadband antennas have lower probability of missing transient signals than those that use tunable antennas (Jenkins, 1991). Moreover, DF systems using UWB radar or TDOA method require broadband antenna elements, since the signals they are dealing with have wide instantaneous bandwidth.

Among these wideband DF methods, the sensor array methods have the best DoA estimation accuracy, but this advantage comes at the expense of having large physical dimensions, high computational load and high cost (Chandran, 2005). Moreover, as the aperture size of the array goes down, the DoA estimation accuracy and bandwidth of the antenna elements both reduce significantly. In fact, Nordebo et al. (2006) proposed a lower bound of DoA estimation error for any antenna array confined within a given sphere. However, since the DF systems are usually deployed on some platform, a possible solution to surpass this limitation is to elaborate the presence of the platform.

In contrast, the rotating antenna method costs far less since it requires a simple antenna array and a single receiver. However, the reported antenna arrays used for rotating antenna method usually have relatively large size (Bailey et al., 2012; Liang and Chia, 2001; Liberal et al., 2011) or less-directional radiation patterns (Mingjian Li, 2018).

1.3 Thesis Overview

The thesis is organized as follows.

Broadband Small-Aperture Direction Finding Array with Azimuth and Elevation Estimation Capability

A broadband, compact antenna array capable of estimating the elevation and azimuth angles of arrival (AoA) is presented. Small-aperture direction finding (DF) arrays consisting of a few receiving elements are widely used at lower frequency bands (e.g., HF and VHF bands) where the electromagnetic wavelength is large and the physical size needed to accommodate the array is small. To design the proposed compact DF array, I have examined different array topologies that provide elevation and azimuth estimation capabilities, and that are immune to errors caused by cross polarization. All of these potential candidates have the same maximum linear dimension of 19 cm. Subsequently, I adopt the topology that provides the lowest Cramer-Rao bound (CRB). The topology of this array is further optimized to efficiently utilize an available volume with side lengths of 14 cm$\times$14 cm$\times$5.5 cm. The DF performance of this array is characterized over a wide frequency range spanning from 30 MHz to 2000 MHz using computer simulations. A prototype of the array was also fabricated and characterized using field tests at a number of discrete frequencies within this band. The measurement results show very good agreement with simulations, and validate the DF capabilities and the expected accuracy levels predicted by CRB.

Design of Platform-Based HF Direction Finding Antennas Using the Characteristic Mode Theory

A systematic method for utilizing the characteristic modes of a platform to design a direction finding (DF) system operating at the high-frequency (HF) band is presented. In this band, due to the large wavelengths, practical antennas used for DF are electrically small and have limited bandwidths. When such a DF array is mounted on a platform, however, the platform's presence can be exploited to considerably improve the performance of the platform-based DF system compared to that of a stand-alone DF system. My proposed approach relies upon selecting and exciting a group of the platform's characteristic modes that provides the lowest Cramer-Rao bound for the DF system's accuracy. This approach allows for designing DF systems that canaccurately detect the direction of arrival and the state of polarization of the wave over wide fields of views. This approach is used to design and simulate an HF DF system for an airborne platform. A scaled-model prototype of this platform-based DF array is fabricated and characterized. The measurement results of this array are used to perform DF experiments in an emulated environment. Measured results are found to be in good agreement with simulations, confirming the efficacy of the proposed design approach.

A Spatially-Confined, Platform-Based HF Direction Finding Array

A spatially-confined, platform-based HF antenna array with enhanced bandwidth and direction finding accuracy is presented. As the HF band is widely used in many important civilian and military applications, HF DF systems are of great interest in electronic warfare support applications. However, due to the large wavelength, practical DF arrays mounted on moving platforms tend to be electrically small, resulting in fundamental limitations on antenna bandwidth and DF accuracy. Furthermore, many applications require mounting the array at a single location on the platform due to limited space and mobility considerations. To alleviate these issues, I employ the platform as the major radiator by exciting its multiple characteristic modes using a spatially-confined antenna array. Specifically, I examined four designs mounted on a representative, mid-size passenger airplane operating at 10 MHz in simulation, each of which is confined within a virtual sphere with a 3-m diameter. A scaled model of one design was fabricated and characterized. Cramer-Rao bounds and Monte-Carlo test results were also reported. The results demonstrate that the proposed DF array can provide a 15% lower DoA estimation error than the theoretical limit of a standalone array possessing the same volume and having the same bandwidth.

A Compact, Broadband, Multibeam VHF/UHF Antenna Array for Directional Networking and Direction Finding Applications

A compact, broadband, multibeam antenna array suitable for directional networking and direction finding applications in the 225–400 MHz band is presented. This frequency band is extensively used in land mobile/fixed and air-ground-air communications by the military and government agencies in many nations. Therefore, directional networking as a mean of improving capacity and DF systems for electronic warfare support are of great interest. Antenna arrays suitable for both applications requires radiating multiple vertically-polarized, independent beams over an octave bandwidth. However, current techniques can hardly achieve such requirements in a compact size. To solve this issue, I used a revised version of Huygens source antenna that employs multiple strategically-placing electric and magnetic dipoles and their mirrors. Simulation results demonstrate that the antenna can achieve 7–8 dBi gain within half wavelength at center frequency. Further, this antenna is used in a uniform circular array that generates eight independent beams. DF accuracy was characterized at various signal-to-noise ratio and multiple frequencies over the 225–400 MHz band with using Cramer-Rao bound and Monte-Carlo experiments. The results demonstrate a very good DF accuracy at low SNR over the entire frequency band.

2 BROADBAND SMALL-APERTURE DIRECTION FINDING ARRAY WITH AZIMUTH AND ELEVATION ESTIMATION CAPABILITY

2.1 Introduction

Broadband direction finding (DF) systems are widely used in many civil and military applications. Knowing the direction of incoming electromagnetic waves is extremely important in navigation, rescue and electronic warfare support applications among others. In some DF applications, particularly those pertaining to electronic warfare support, broadband antennas are usually preferred. For example, in surveillance applications, having DF arrays with wide instantaneous bandwidths helps increasing the probability of intercept. Moreover, having capability of estimating both azimuth and elevation angles of arrival (AoA) is necessary for 3D target localization. Furthermore, practical HF/VHF DF systems usually suffer from AoA estimation error caused by cross polarization resulting from the depolarization of wave by ionosphere, terrain and forests (Jenkins, 1991). Therefore, having the immunity to polarization error is also important. However, due to the large wavelength of electromagnetic waves in HF and VHF band, or because of the mobility and/or aerodynamic considerations, practical DF arrays need to have compact dimensions. Designing a small-aperture DF array with wideband, elevation and azimuth AoA estimation capability, and immune to cross-polarization error is indeed a challenging feat.

Over the years, a variety of broadband, compact or electrically-small antennas have been proposed (Noguchi et al., 2003; Best, 2005; Stuart and Best, 2008; Hong and Sarabandi, 2009; Erentok and Ziolkowski, 2008; Lee et al., 2002). These antennas provide bandwidths approaching the physical limitations (Chu, 1948; Gustafsson et al., 2007). However, these papers did not examine the DF capabilities of these broadband antennas. In fact, research conducted by Nordebo et al. (2006) implies that small apertures are not able to simultaneously achieve optimal bandwidth and best DF accuracy . The use of electrically-small antennas or small-aperture antenna arrays for direction finding has been extensively examined in the past. DF using a rotating electrically-small loop or dipole, whose radiation pattern has a sharp null, is one of the earliest techniques reported in this area (Terman, 1955; Schlub and Thiel, 2004). Bellini and Tosi use two orthogonal loops to detect AoA by comparing the signals' amplitude ratio received by the two loops (Bellini and Tosi, 1909; Jenkins, 1991). These antennas can be made very small by wrapping many turns around a ferrite bar. Electronically steerable parasitic radiators (ESPARs) with directional patterns have been demonstrated azimuth AoA estimation capability with up to 15% bandwidth (Preston et al., 1998; Sun et al., 2004; Taillefer et al., 2008). Similarly, electrically switching between antenna elements that have identical figure-eight-shaped radiation patterns with nulls pointing towards different directions can be implemented to achieve a much wider bandwidth with a smaller formal factor. This concept is fundamentally an extension of the Watson-Watt method and Adcock antenna array (Adcock, 1919). Recently, based on conventional Adcock array, our group reported an electrically-small array composed of four broadband hexagonal cones used to perform DF in a very broad bandwidth (Ghaemi et al., 2018). These arrays can be used to estimate azimuth AoA effectively. However, they are lack the capability of estimating the elevation AoA. Furthermore, in these arrays, if the polarization of the incoming wave is not perfectly matched with that of the DF array, significant DF errors may be caused (Jenkins, 1991). Significant cross-polarization component may exist in a DF application is situations where a wave is received through a non-line-of-sight path, such as reflection by the ionosphere (e.g., HF Skywave propagation) (Kelso, 1972; Jenkins, 1991). To estimate the elevation AoA and the state of polarization of the wave in addition to its azimuth AoA, vector sensor arrays (VSA) (Meloling et al., 2016; San Antonio et al., 2013), and B-dot sensors (Wong and Zoltowski, 1997; Archer, 2013) have been investigated. These sensors are composed of collocated orthogonal electrically small loops and dipoles, which measure the different orthogonal components of electric and magnetic fields to determine AoA and polarization. Slater et al. (2013) reported an antenna array composed of displaced miniaturized loops and dipoles. Compared with VSAs, this array can collect extra phase difference between antenna elements to improve

DF accuracy. However, the above mentioned DF arrays do not have wide instantaneous bandwidth. Antenna arrays with a variety of array geometries have been extensively investigated. Incorporated with advanced signal processing algorithms and broadband antenna elements, these arrays can provide, in a wide frequency range, highly-accurate elevation and azimuth AoA estimation capability (Remez and Ben-Ari, 2009; Holder, 2014; Tayem and Kwon, 2005; Schlub and Thiel, 2004). However, these arrays need to possess a large volume.

In this chapter, I present a compact direction finding array that provides the capability of estimating azimuth and elevation AoAs, and that is immune to cross polarization error. The proposed antenna array is designed to occupy a fixed physical volume of 14 cm $\times$ 14 cm $\times$ 5.5 cm mounted on top of a ground plane. This array is composed of four vertically placed hexagonal-cone-shaped monopole antennas and two horizontally placed bow-tie-shaped dipole antennas on top of the monopoles. This array topology is selected, among a number of other small-aperture DF array candidates that occupy the same volume, since it shows the lowest Cramer-Rao bound (CRB) on the estimation accuracy of the two parameters of interest (i.e., elevation and azimuth AoAs). The DF performance of this array is investigated in simulation and measurement by examine the CRB over a frequency range of 30–2000 MHz. A prototype of this array is fabricated and used to perform direction finding in an outdoor environment over a frequency range of 30–700 MHz. My simulation and measurement results demonstrate that the fabricated prototype has the capability of estimating the elevation and azimuth AoAs, which is insensitive to the polarization of incoming waves, and can achieve the AoA estimation accuracy predicted by the theoretical bound. In the frequency range of 400-2000MHz, the array typically has accuracy levels of $0.1°$–$1°$ for an SNR level of 25 dB and number of snapshots of 100. In the frequency range of 30 MHz - 400 MHz, the array typically has accuracy levels of $1°$–$30°$ for an SNR level of 60 dB and number of snapshots of 100.

2.2 The Design Procedure

Due to the physical restrictions, small-aperture DF arrays usually have no more than a few antenna elements packed in a small volume. These elements are generally either small dipoles or loops, since ultra-wideband antenna elements (e.g. Vivaldi, horns, etc.) and typically electrically large. Therefore, in the first step of the design procedure, I examine a number of DF array topologies to identify those that have the a better chance of meeting the desired requirements (i.e., capability of determine elevation AoA, azimuth AoA, and immunity to the AoAs estimation error caused by cross polarization of the incoming wave). Next, I compare these selected topologies and adopt the one with the lowest CRB. Finally, I optimize the shapes and locations of the antenna elements of the this topology to finalize the design.

Selecting Array Configuration Based on DF Capabilities

To determine the DF capability of a given antenna array, I examine the number of unknown parameters and the number of constraints provided by the array. Let us assume that the unknown parameters to be estimated are the azimuth AoA, the elevation AoA, and the polarization tilt angle of the impinging wave. Also, let us assume that the goal is to detect a single, linearly-polarized incident wave. Then, the number of unknown parameters is three. The constraints are the measured complex voltages (or currents) at the terminals of the antennas used in the array. If no mechanical rotation or movement of the antenna array is allowed during the entire DF procedure, having one reference element is necessary. The voltages (or current) measured at the other elements need to be compared with that measured at the reference element, and compensate the (unknown) strength and phase of the signal carried by the incident wave. Thus, M antenna elements provide no more then independent $2 * (M - 1)$ real constraints.

In Fig. 2.1, I compare several designs in terms of elevation and azimuth AoAs, and polarization tilt angle estimation capabilities. The two collocated cross loops in Fig. 2.1(a) provide one constraint, i.e., the ratio of the signal amplitude measured at the two loops. Since These two loops have the same phase center, they are always

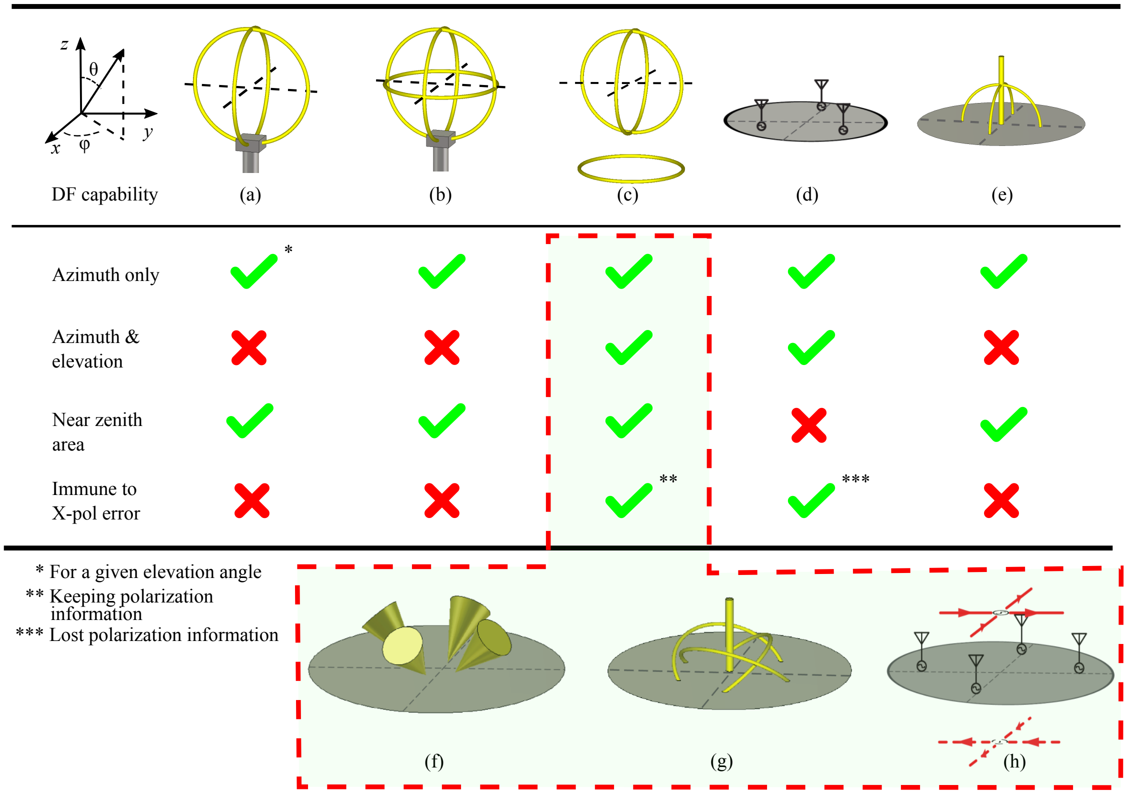

DF capability	(a)	(b)	(c)	(d)	(e)
Azimuth only	✓*	✓	✓	✓	✓
Azimuth & elevation	✗	✗	✓	✓	✗
Near zenith area	✓	✓	✓	✗	✓
Immune to X-pol error	✗	✗	✓**	✓***	✗

* For a given elevation angle
** Keeping polarization information
*** Lost polarization information

Figure 2.1: Comparison of DF capabilities of difference array topologies.

measuring the same phase. The two electrically-small loops have orthogonal figure-eight shaped radiation patterns in the azimuth plane. Therefore, given the tilt angle of an impinging wave, only the azimuth AoA can be estimated. Unknown cross polarization can introduce AoA estimation errors (Jenkins, 1991; Weiss and Friedlander, 1991). Similarly, the antenna array depicted in Fig. 2.1(b) is composed of three collocated, electrically-small loops, which provide two constraints. As a result, this array can be used to estimate the azimuth and elevation AoA if the tilt angle of an impinging wave is known a priori. However, similar to the cross loops, this array cannot be used to estimate the polarization tilt angle of the incident waves. To circumvent this issue, one of the three loops can be moved away by a small distance, as shown in Fig. 2.1 (c). This off-center loop measures a different phase of the incoming electromagnetic wave, providing one more constraint. This array has the capability of estimating the azimuth and elevation AoAs, and the polarization tilt angle of impinging waves. Two other, potential three-element arrays candidates are shown in Figs. 2.1(d) and 2.1(e). The one shown in Fig. 2.1(d) is composed of three displaced vertical monopoles. This array provides two independent constraints, because the three antennas consistently measure the same magnitude for any AoA and polarization tilt angle. Therefore, this array can be used to estimate the azimuth and elevation AoAs, and is immune to the estimation errors caused by cross polarization. The array shown in Fig. 2.1(e) is composed of two crossed loops and a monopole. This array has similar DF capability to the three-loop array shown in Fig. 2.1(b). To compensate for the lack of minimum required constraints in the arrays shown in Figs. 2.1(b) and 2.1(e), I propose an array topology composed of three collocated tilted loops and one vertical monopole as shown in Fig. 2.1(g). This array provides three constraints with diversely polarized antenna elements. Therefore, it can be used to estimate azimuth and elevation AoAs, as well as the polarization tilt angle of incident waves.

I also consider the DF capability in near zenith area, where AoA estimation is usually challenging (Jenkins, 1991). All the above-mentioned arrays except the one shown in Fig. 2.1(d) are potential candidates for covering the near zenith area, because their elements can efficiently receive signals from this area, and have diverse radiation patterns there. To mitigate this coverage issue of the array shown in Fig. 2.1(d), I tilt the vertical monopoles of the array outwards as shown in Fig. 2.1(f). This way, the monopoles are not only able to receive signals more efficiently from the near zenith area, but also respond differently as a function of the polarization tilt angle of incoming waves. As a result, this array is also able to detect the tilt angle. Another way to mitigate the coverage issue is to put horizontal dipoles over the vertical monopoles as shown in Fig. 2.1(h). The added dipoles are positioned to receive signals coming from the near-zenith area.

To sum up, I considered the elevation AoA, azimuth AoA, and polarization tilt angle estimation capability of eight possible array topologies. Four of them provide all these DF capabilities as well as near-zenith coverage. Due to the relatively large dimension of the array shown in Fig. 2.1(c), I finally choose the three arrays shown in Fig. 2.1(f)–2.1(h) for further evaluation.

Selecting a Suitable Array Topology Based on CRB

Cramer-Rao bound (CRB) is a theoretical error bound of any unbiased (zero bias) estimator. It is a good predictor of the AoA estimation accuracy provided by an antenna array (Weiss and Friedlander, 1991). The calculation of CRB completely follows the procedure presented in (Weiss and Friedlander, 1991). According to this paper, CRB is the inverse of Fisher Information Matrix (FIM).

$$\mathbf{CRB} = \mathbf{F}^{-1} \tag{2.1}$$

Each element of the FIM can be written as:

$$F_{mn} = K \cdot \mathrm{tr}\left\{ \mathbf{R}_x^{-1} \frac{\partial \mathbf{R}_x}{\partial p_m} \mathbf{R}_x^{-1} \frac{\partial \mathbf{R}_x}{\partial p_n} \right\} \tag{2.2}$$

where K denotes number of snapshots, p_m is the m^{th} parameter of the model, and $\mathrm{tr}\{\cdot\}$ represents the trace of the matrix. These parameters, in our case, include the elevation and azimuth AoAs (denoted by θ and ϕ respectively), and the polarization tilt angle of the impinging waves (denoted by γ). $\mathbf{R}_x$ is given by:

$$\mathbf{R}_x = \mathbf{A}\mathbf{R}_s\mathbf{A}^H + \sigma^2\mathbf{I} \tag{2.3}$$

where the $M \times 2N$ matrix $\mathbf{A} = [\mathbf{A}_\phi, \mathbf{A}_\theta]$ is the ϕ and θ components of the radiation patterns of the antenna array; M is the number of array elements; N is the number of impinging waves; the $2N \times 2N$ matrix $\mathbf{R}_s$ is signal covariance matrix. The real, positive number σ^2 denotes the variance of Gaussian white noise. The $M \times M$ matrix $\mathbf{I}$ is identity matrix.

Let us assume that we aim to detect one incident wave, i.e. $N = 1$. Then, $\mathbf{R}_s$ is a scalar, i.e. $\mathbf{R}_s = 1$. To calculate the CRB correctly, it is necessary to consider all unknown parameters even if not all of them are of interest (Weiss and Friedlander, 1991). In this specific design, there are three unknown parameters – the azimuth and elevation AoAs are of interest and the tilt angle of the impinging wave is also unknown. Therefore, we calculate the CRBs of the selected arrays as a function of azimuth AoA, elevation AoA, and tilt angle. Then, the CRBs are 3×3 matrices. During the calculation, we assume that the available signal-to-noise ratio (SNR) is 25 dB (i.e. $\mathbf{R}_s/\sigma^2 = 10$ dB). In other words, the SNR of the data fed into the AoA estimation algorithm is 25 dB if the antenna's realized gain is 0 dBi. Notice that in this analysis, the variations in the realized gains of the antennas as a function of frequency is taken into account and a reduction in the realized gain of the antenna below 0 dBi causes a reduction of the effective SNR. Since the performance comparison of these arrays is performed over a very wide bandwidth, the realized gains of the antennas will vary and towards the lower end of this range, the antennas will be electrically-small and hence, impedance mismatched. Furthermore, we assume the number of snapshots $K = 1$ for $ka = 0.99$ and 1.40, and $K = 100$ for $ka = 0.4$, to present reasonable CRB values. Since CRB is inversely proportional to the number of snapshots, this assumption dose not effect the generality of the analysis presented (Weiss and Friedlander, 1991).

Fig. 2.2 compares the CRB patterns of four different array topologies. All arrays are placed on infinite ground planes. As a benchmark of the DF performance, Fig. 2.2(a) depicts the CRB of a known wideband electrically-small antenna array (Ghaemi et al., 2018). The other three subfigures show the array topologies selected in Section 2.2. Similar to the array topology shown in Fig. 2.1(d), the benchmark array is composed of four vertical monopoles. As can be seen, only the ϕ component of the CRB in near horizon region is small. This means that the array can only be used to detect azimuth AoA in the region far away from the zenith. The azimuth AoA estimation capability agrees with the qualitatively analysis on the array shown in Fig. 2.1(d) discussed in Section 2.2. For the elevation AoA, the array has very poor estimation accuracy in the entire upper hemisphere (2π solid angle). In the near horizon region, this poor performance is due to the array geometry–the derivative of phase difference between the antenna elements with respect to elevation angle is zero. In the near zenith region, this is due to the nulls of the radiation

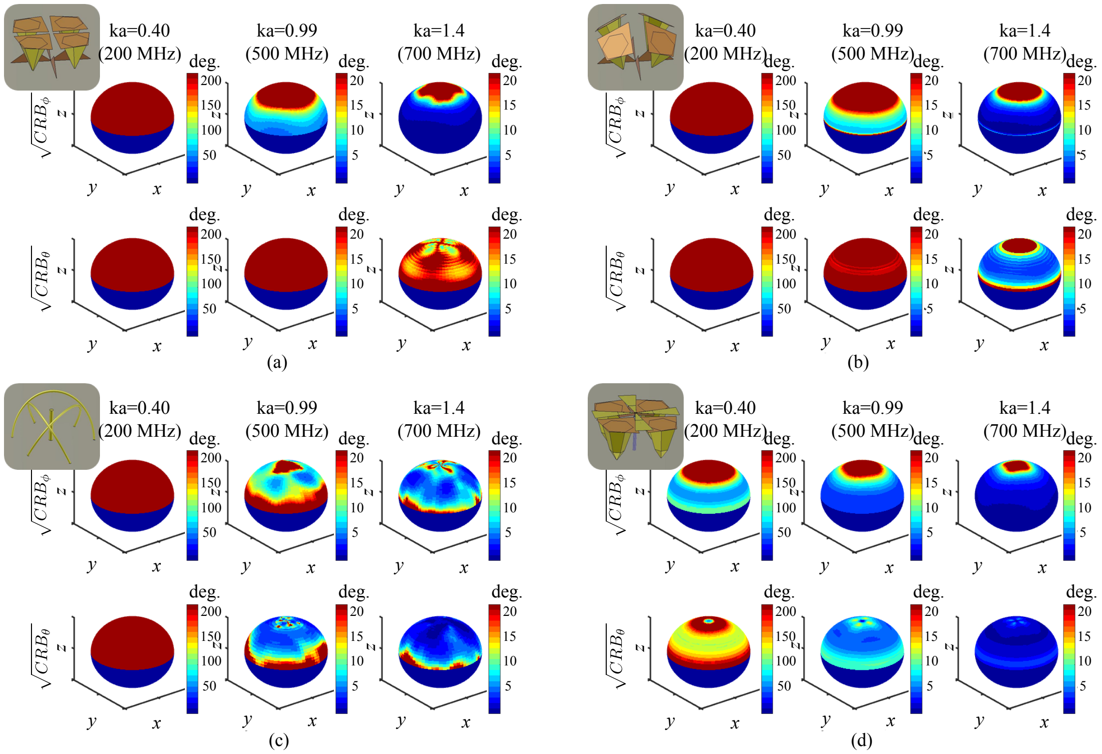

Figure 2.2: CRB patterns of (a) four vertical monopoles, (b) tilted monopoles, (c) collocated tilted loops and vertical monopole, and (d) vertical monopoles and horizontal dipoles. (a) is a reported wideband electrically small antenna array with azimuth AoA estimation capability (Ghaemi et al., 2018). (b)–(d) are the selected arrays with elevation and azimuth AoAs estimation capability.

patterns of the monopoles (Holder, 2014). Also, it can be seen that as frequency increases CRB values decrease, which indicate a higher DF accuracy. This is due to two distinct factors. First, as frequency increases, the electrical dimensions of the aperture also increase enhancing the contrast between the signals received at the different antennas. Secondly, as frequency increases, the impedance matching of each element improves resulting in a significant increase in the realized gain of the element and enhancement of the effective SNR (i.e,. available SNR plus the realized gain of the element in dB scale).

As shown in Fig. 2.2(b), using the array consisting of the tilted monopoles improves the elevation AoA estimation accuracy (at $ka = 2.6$) while slightly sacrificing the azimuth performance. In this array, the tilted angle of the monopoles is 30°. This angle is a trade-off between diversity and the impedance matching of the antenna elements. Tilting the monopoles can improve their diversities, but tilting the monopoles too much makes them close to horizontal dipoles placed near an infinite PEC ground, making it difficult to impedance-match them. However, the improvement of elevation AoA estimation accuracy dose not happen in high elevation region. The array shown in Fig. 2.2(c) which uses the tilted loops with a monopole has better elevation AoA estimation performance. However, this improvement is not uniform across the entire space. Additionally, the azimuth AoA estimation capability of this array topology does not provide a uniform accuracy level across the entire azimuth plane, either. The non-uniformity of the coverage is due to the fact that the elements are as large as 120° separated along azimuth direction, and that their radiation patterns along the azimuth plane are not omni-directional. Consequently, the CRB patterns reveal 120° rotational symmetry. Furthermore, this array topology tends to have a narrower bandwidth compared to the others shown in Fig. 2. This is primarily due to the poor impedance matching of the electrically-small loops used in the array. The mismatch reduces realized gain and the effective SNR, resulting in an increase in the CRB values. Fig. 2.2(d) depicts the CRB pattern of the array topology shown in Fig. 2.1(h). This array is composed of four vertical monopoles and two horizontal dipoles placed at a very small distance on top of the vertical monopoles. The CRB patterns demonstrate better AoA estimation accuracy over a relatively wide frequency range and for a wide field of view.

Finalized Design

Following the discussion presented in the previous section, the array topology shown in Fig. 2.2(d) was adopted. To enhance the bandwidth of the array while maintaining a low profile, I use hexagonal-shaped cones to implement the monopoles, and use bow-tie shaped horizontal dipoles as shown in Fig. 2.3. Full-wave electromagnetic simulations and optimizations were performed to maximize the impedance bandwidth of the antennas (-6 dB reflection coefficient). The monopoles are optimized by starting from a known, recently reported design (Ghaemi et al., 2018). However, because of the presence of the horizontal dipoles on top of the monopoles, the dimensions of the hexagonal-shaped monopoles were modified. Specifically, the waist of each hexagonal-shaped monopole was increased compared to those reported in (Ghaemi et al., 2018). The tophats on the monopoles are used to capacitively load the monopoles and to further reduce their length. Each bow-tie arm is made out of a 0.26 mm thick layer of copper supported by a smaller section of 3.0-mm thick layer of copper close to the feed point. The 3.0 mm thick copper around the center of the bow-tie is used to provide structural rigidity to the horizontal bow-tie arms and facilitate the connection of the feed lines to the center of the bow-tie antennas. Additionally, this 3.0-mm thick copper also is used to improve the impedance matching of the bow-tie antennas. Each arm of the bow-tie antennas are connected to the inner conductor of a coaxial cable. The outer conductor of the four coaxial cables are soldered together and connected to the ground plane. Then, the terminals of the two coaxial cables corresponding to each bow-tie antenna are fed with a balun. For the baluns, I used two commercially available 2-way 180° power splitters (Mini-Circuit ZFSCJ-2-232-S+). The dipoles were placed at a distance of 5.0 mm above the top surface of the monopoles to maintain a low profile.

Fig. 2.4 shows the simulated S-parameters of the antennas used in this array. The monopoles show an impedance matching better than -6 dB from 443 MHz to over 3000 MHz, and the dipole show an impedance matching better than -6 dB from 369 MHz to 1459 MHz. In simulation, I used the measured S parameters of the two power splitters actually used in the fabricated prototype, resulting in small difference of the reflection coefficients of the two dipoles in Fig. 2.4(b). The mutual coupling between the antenna elements is less than -8 dB over the entire simulated frequency range. The strongest mutual coupling happens at around 500 MHz.

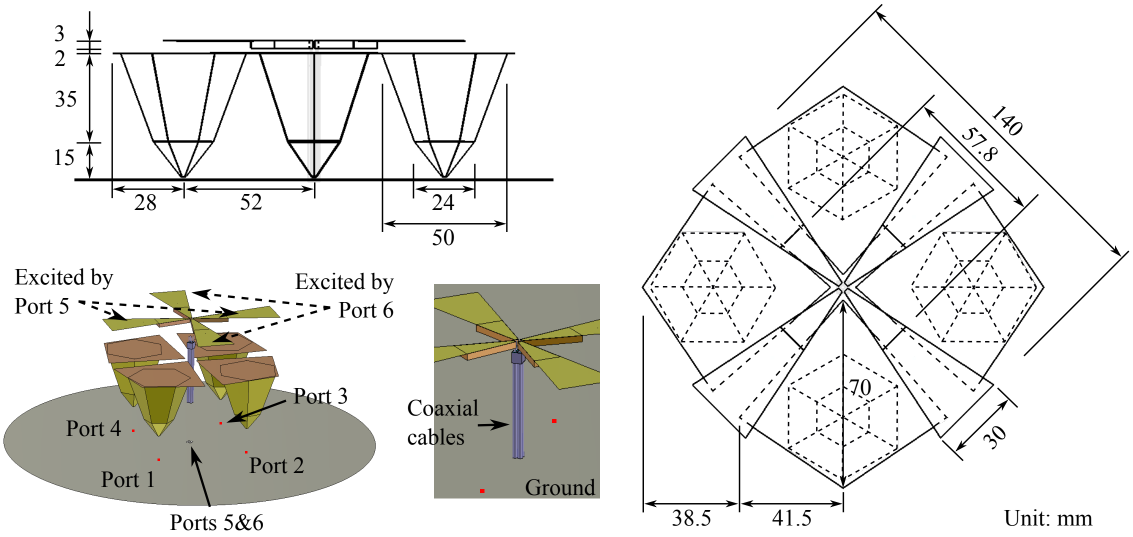

Figure 2.3: Side view and top view of the finalized design, with dimensions marked. This antenna array was fabricated, measured and used to do direction finding field tests.

2.3 Fabrication and Measurement

A prototype of the proposed array was fabricated and experimentally characterized. Fig. 2.5 shows a photograph of the fabricated prototype in the test chamber used to perform radiation pattern measurement in the frequency range of 430 MHz-2000 MHz. The DF array is mounted on an octagon-shaped ground plane with a diameter of 740 mm.

The S-parameters of the antenna were measured using a calibrated network analyzer and the results are presented along with the simulated S-parameters in Fig. 2.4. In general, the measurement results have a good agreement with the simulation results. , Compared with the simulation results, the measured reflection coefficients of the monopoles demonstrate a similar triple-resonant feature. The measured mutual coupling between the monopoles and dipoles show a very similar trend and level to the simulated results. Observe that the measured reflection coefficients of the two dipoles show two notches at around 1 GHz, which are notably

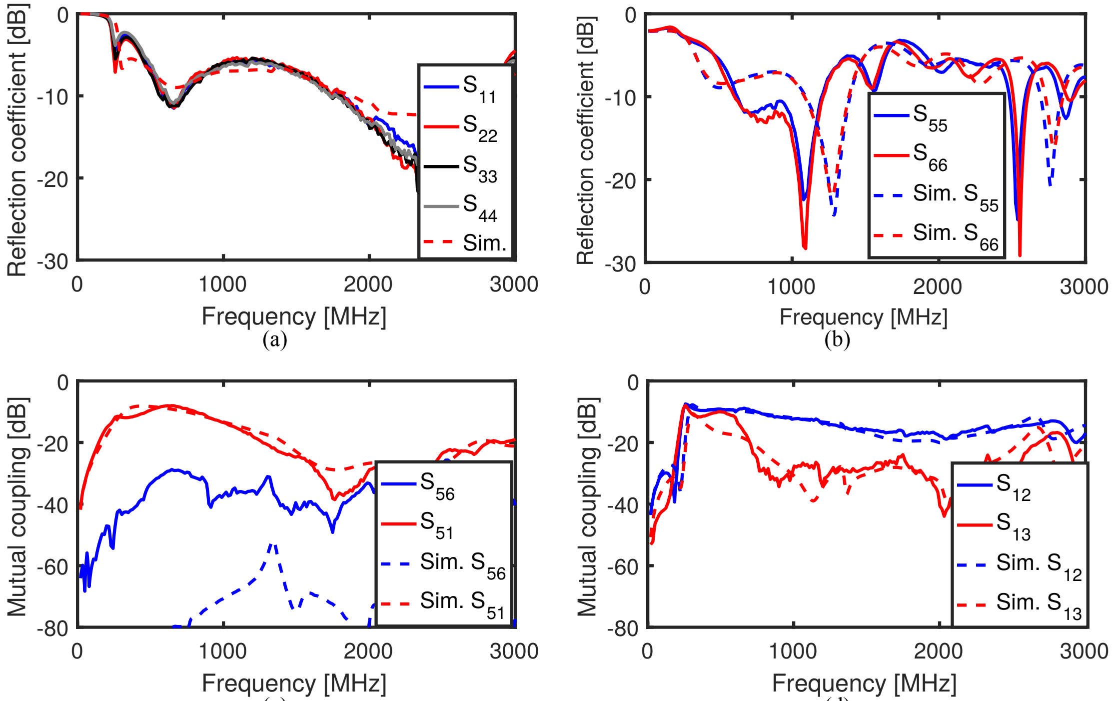

(a) (b) (c) (d)

Figure 2.4: Simulated and measured reflection coefficients of (a) the vertical monopoles and (b) the horizontal dipoles.

closer than the simulation results. The reason for this disagreement is that the dipoles are very closely placed on top of the monopoles. This small distance strongly effects the resonant feature of the dipoles. However, limited by the fabrication precision in our lab, I did not have good control over this small distance, resulting a shift of the two resonances. Besides, owing to the fabrication precision, the measured mutual coupling between the dipoles (S_{56}) is around -40 dB. This is already a rather low mutual coupling level in measurement while not as low as the simulated result.

The radiation patterns of the antenna were measured with a near-field spherical measurement system (SATIMO StarLab) for frequencies above 430 MHz. Since the lowest frequency of operation of our near-field system is 430 MHz, radiation pattern measurements at lower frequencies could not be performed. Selected measured and

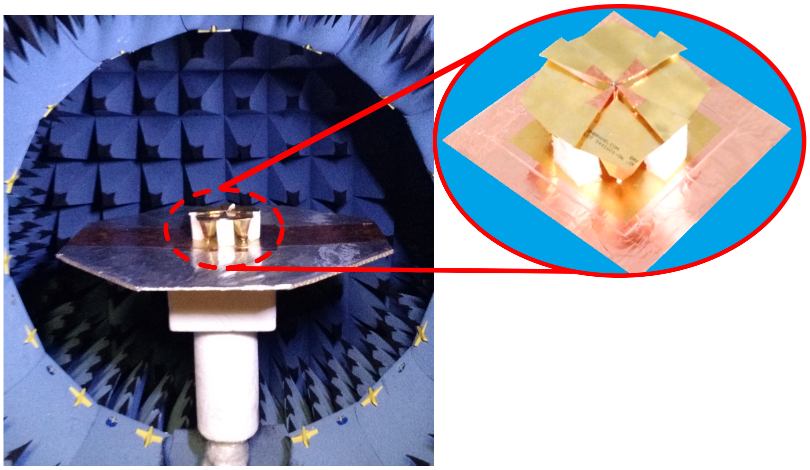

Figure 2.5: Fabricated antenna prototype and measurement setup with SATIMO StarLab near-field test station.

simulated realized gain patterns are show in Fig. 2.6. In general, a good agreement between the simulated and measured radiation patterns in this frequency range is observed. Observe that the monopoles have strong radiation away from zenith whereas the dipoles have strong radiation towards zenith over most of the frequency band. This amplitude contrast primarily contributes to the improved elevation AoA information. Additionally, over most of the upper hemisphere, the polarizations of the monopoles and the dipoles are different. This enhances the capability of the array in determining the polarization tilt angle of the incoming wave. Moreover, the radiation patterns of each monopole is not symmetric due to the close proximity of the other array elements. Finally, the directions of maximum radiation of the monopoles is tilted upwards from the azimuth plane due to the finite dimensions of the ground plane (Balanis, 2016).

Following these standard antenna measurements, I calculated the corresponding CRB patterns of the array with formulas (2.1)–(2.3). I assumed that the available SNR is 25 dB, and that the number of snapshots is $K = 1$. Note that the CRB is inversely proportional to K (see (2.2)), and the readers can easily scale the CRB results by choosing proper number of snapshots in his applications. Therefore, the

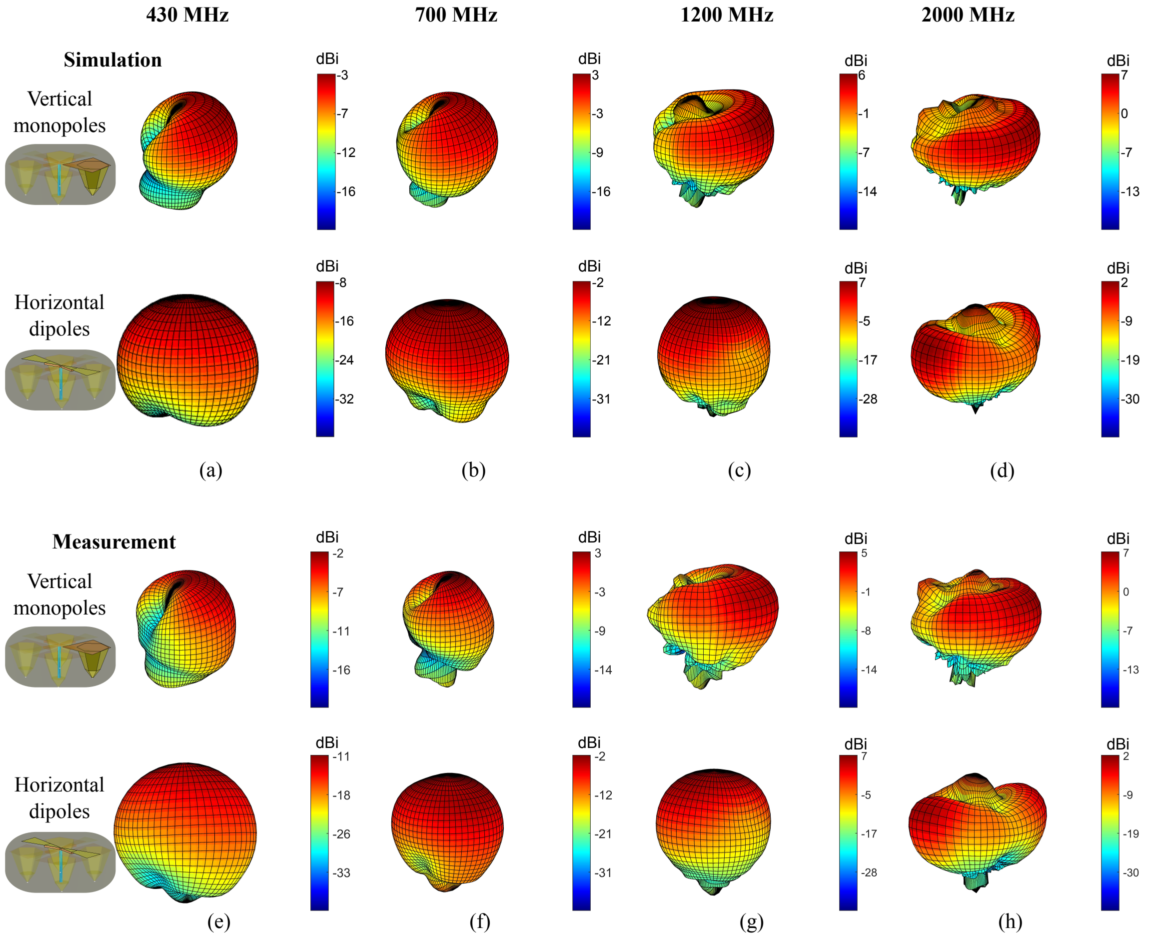

Figure 2.6: (a)–(d) Simulated and (e)–(h) measured realized-gain radiation patterns at (a, e) 430 MHz, (b, f) 700 MHz, (c, g) 1200 MHz and (d, h) 2000 MHz.

choice of $K = 1$ does not effect the generality of the shown results. For frequencies from 430 MHz to 2000 MHz, the CRB patterns were calculated with both simulated and measured radiation pattern. These CRB patterns are compared in Fig. 2.7. $\sqrt{\text{CRB}}$ greater than the marked range in the color bar is drawn in red color. It can be seen, the fabricated prototype shows very similar CRB patterns to those of the simulated model, indicating their similar DF accuracy. At 700 MHz, the CRB calculated with measured radiation patterns is slightly lower than that calculated with simulated radiation patterns. This is because of the better impedance matching of the fabricated prototype at 700 MHz (as shown in Fig. 2.4), which results in a higher realized gain. Therefore, for the same available SNR, the fabricated prototype provides better effective SNR for AoA estimation algorithms.

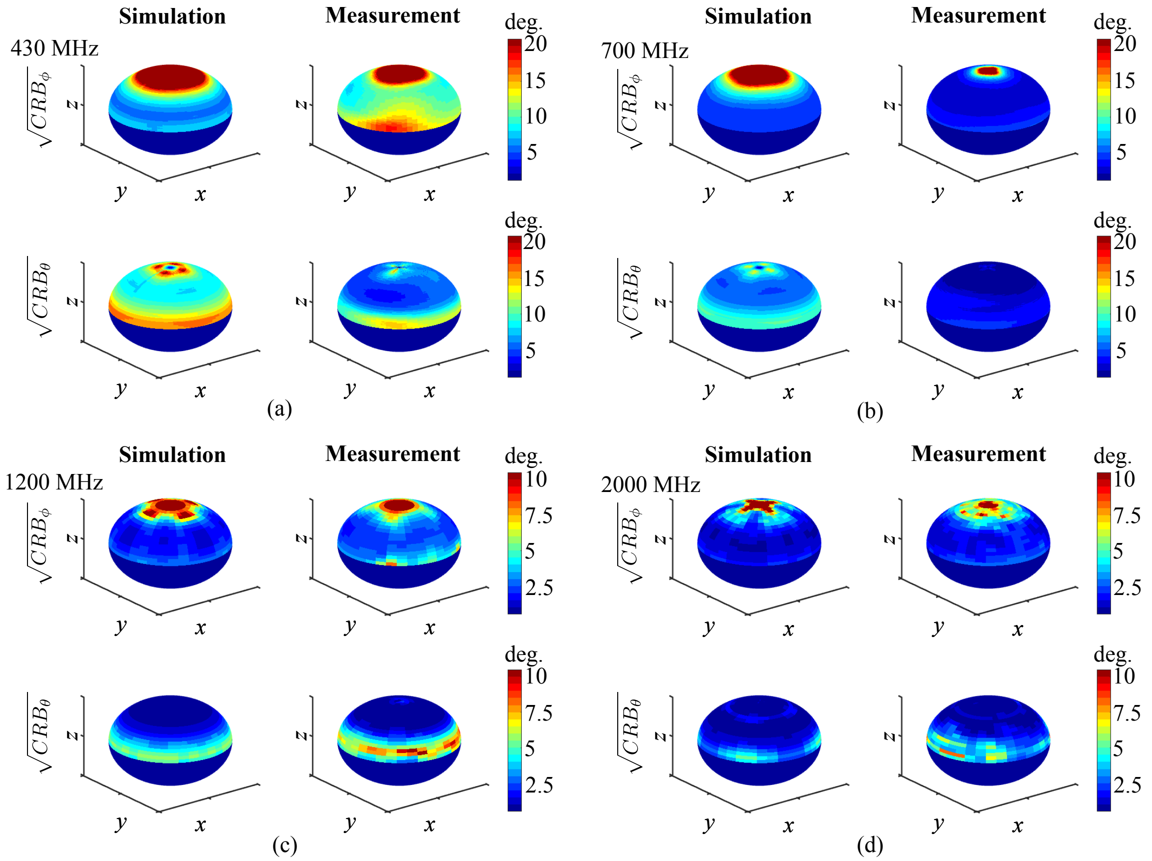

Figure 2.7: CRB computed with measured and simulated radiation patterns at (a) 430 MHz, (b) 700 MHz, (c) 1200 MHz, and (d) 2000 MHz. In each figure, $\sqrt{\mathrm{CRB}_\theta}$ denotes the CRB of elevation angle of arrival (AoA) while $\sqrt{\mathrm{CRB}_\phi}$ denotes the CRB of azimuth AoA. Available SNR is 25 dB, number of snapshots $K = 1$.

For frequencies below 400 MHz, because of the limitation of our antenna characterization facilities, measured radiation patterns were not available. Thus, simulated radiation patterns were used to calculate the CRB patterns. To demonstrate more reasonable CRB values, available SNR is change from 25 dB to 60 dB only for the CRB patterns presented in Fig. 2.8. The number of snapshots is $K = 1$. Given the

SNR is large, if using SNR of 25 dB, similar CRB performance can be expected with $K = 3200$ (or 35 dB). Observe that at lower frequencies (e.g. 50 MHz or below), the CRB values are rather large. This indicates that the DF accuracy of this array drastically reduces for very low frequencies. This is expected because at these frequencies, the antennas are severely impedance mismatched and have extremely low realized gain values. This results in the degradation of the effective SNR of the array that in turn reduces the DF accuracy of the system. Additionally, at these frequencies, the electrical dimensions of the aperture are very resulting in very small contrast between the signals received at the different antenna terminals.

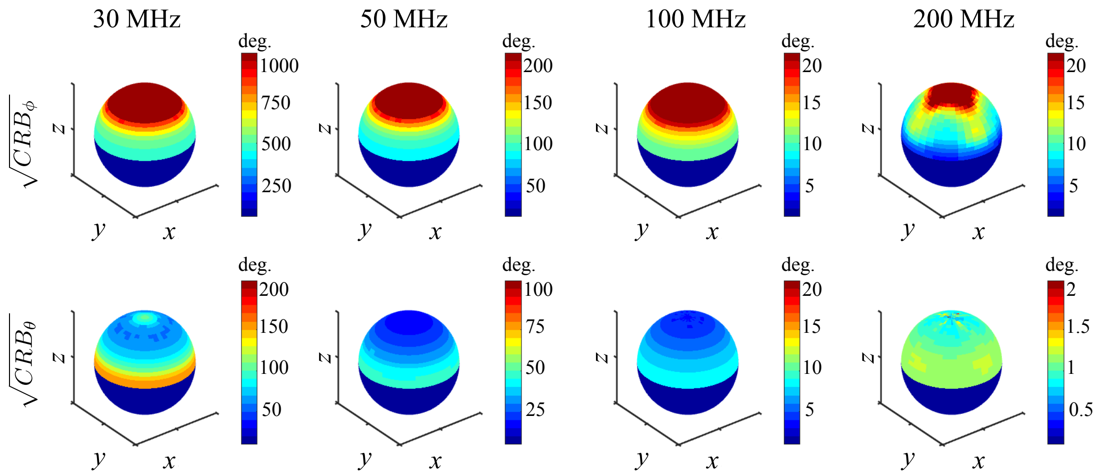

(a) (b) (c) (d)

Figure 2.8: CRB computed with simulated radiation patterns at (a) 30 MHz, (b) 50 MHz, (c) 100 MHz and (d) 200 MHz. In each figure, $\sqrt{\text{CRB}_\theta}$ denotes the CRB of elevation angle of arival (AoA) while $\sqrt{\text{CRB}_\phi}$ denotes the CRB of azimuth AoA. Available SNR is 60 dB, and number of snapshots $K = 1$.

2.4 Direction Finding Field Test Results

Using the DF array prototype discussed in the previous section, I also performed a series of direction finding experiments in an outdoor environment. The DF field tests were performed in a grass field next to a multi-story parking building. Similar

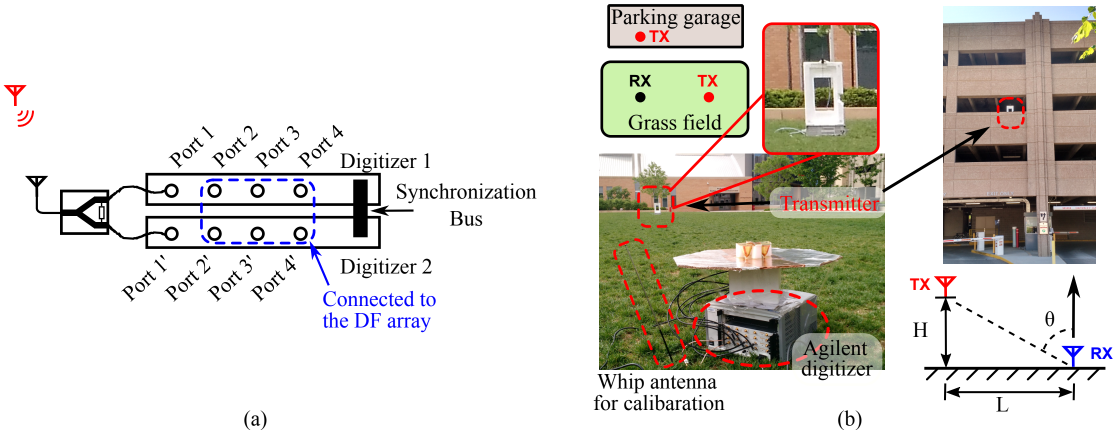

(a) (b)

Figure 2.9: (a) Schematic diagram of the inter-digitizer calibration. (b) Photo and setups of outdoor field tests. The transmitter is placed on the ground, and on the ledge of the concrete barrier on the 3rd and 5th floor of a parking garage to create different elevation AoAs. The receiver together with the fabricated DF array was placed on the ground, and was rotated every 15°, from 0° to 90°, to create different azimuth AoAs.

to the field test method studied by Jenkins (1991), I fixed the transmitter and rotated the receiver to change the azimuth angle of arrival of the wave relative to the receiving DF array. To change the elevation angle of arrival of the wave, the transmitter was moved to different floors of the parking building, allowing me to test the system performance for a finite set of elevation angles. The test configuration is shown in Fig. 2.9. On the transmitter part, a regular half-wave dipole antenna was connected to a signal generator (Agilent E4400B). The signal generator provides a single tone with a maximum power of 20 dBm. On the receiver part, the fabricated prototype is connected to the two synchronized quad-channel digitizers (Agilent U1065A). I connected Ports 2–4 of the one digitizer to Ports 1–3 of the DF array, and connected Ports 2–4 of the other digitizer to Port 4–6 of the DF array. The remaining Port 1 of the digitizers was used for calibration.

In the calibration of the digitizers, I connected a whip antenna to a two-way power splitter (Mini-Circuit ZX10-2-252-S+), and connected the outputs of this power splitter to the Port 1 of the digitizers. This connection is illustrated in

Fig. 2.9(a). Then I sent a signal from the transmitter, and measured the phase difference between the Port 1 of the digitizers. This phase difference will be removed in the following DF tests. Moreover, the phase difference between the outputs of the power splitter was also measured by using a vector network analyzer (VNA), and removed in the DF tests. This calibration procedure needs to be done once whenever the digitizers are turned on, because the two synchronized digitizers maintain a certain phase difference while they are on and running. However, when they get restarted, the phase difference will change. The reason for this phenomenon is that the digitizers have their own clocks which are synchronized via an external bus. Each time the power is turned on, the clocks will have a different initial phase difference. Moreover, the four channels within one digitizer also have certain phase differences caused by the slight difference of the intern circuit between channels. These phase differences do not change when the digitizer is restarted, as the circuit components have not changed. Therefore, I did a one-time calibration in lab to calibrate this phase difference, and then did the inter-digitizer calibrations at the beginning of the field DF tests to remove the phase difference between digitizers. Using a whip antennas, instead of a signal source, for the inter-digitizer calibration is for convenience because the CW signal is always transmitted for DF tests anyway. This also enable me to monitor the synchronization status of the digitizers over the entire DF field test. Besides, all the power splitters and cables used in the field test and the calibration process mentioned above were characterized with VNA over the frequency range and calibrated for ideal components. Specifically, the S-parameters of the two-way and four-way 0° power splitters used in the calibration were measured with a VNA. Any unbalance between their outputs were calibrated. Furthermore, the paired coaxial cables used for connecting the DF array/power splitter outputs and the digitizers were calibrated in a similar way such that they had completely identical electrical length.

The digitizers provide a maximum sampling rate of 2 GS/s. They support a maximum signal frequency of around 800 MHz, assuming the sampling rate is 2.5 times the signal frequency. The flat grass field is 25 meter wide and 70 meter long without significant scatters, and the nearby scatters are symmetrically located.

For the test cases where the transmitter located on the ground (i.e., $\theta = 90^\circ$), this test field is a symmetric one. For the cases where the transmitter is located at the third and fifth floor of the parking garage, there are stationary obstructions close to the transmitter. The obstructions scatter electromagnetic waves in a stationary way. This may introduce bias in the AoA estimation and create cross polarization. However, this was the best test field available to me to perform these measurements. Using this setup, I performed several field tests at frequencies of 29.6 MHz, 109 MHz, 429 MHz and 697 MHz. These frequencies are selected near 30 MHz, 100 MHz, 400 MHz and 700 MHz. The specific frequencies were chosen by collecting background signals and manually checking the level of interference in 1 MHz intervals near the desired frequencies. In each case, these specific frequencies where found to be void of any strong interferer enabling me to perform these continuous-wave (CW) direction finding experiments in a reasonably quiet radio environment.

In the field tests, at each frequency, I put the transmitter on the ground, on the third floor, and on the fifth floor (the roof) of the garage. This created elevation AoA of 90°, 74° and 65°, respectively. For each of these elevation AoA, to create different azimuth AoAs, I rotated the receiver every 15° from 0° to 90°. At every combination of frequency, elevation AoA and azimuth AoA, I collected 3000 time sequences. Each sequence contains 10000 samples at sampling rate of 2 GS/s. During the entire field test, I kept the transmitting dipole vertically placed, intending to make the tilt angle 0°.

In the postprocessing stage, I first applied fast Fourier Transform (FFT) to the time sequences, and extracted the complex signal at the corresponding frequency. Then, I implemented the MUSIC algorithm reported by Ferrara and Parks (1983), and fed these measured voltages into the algorithm to estimate azimuth and elevation angle of the impinging wave. The MUSIC algorithm requires the knowledge of radiation patterns of the DF array as a template to estimate the AoA. In my experiments, I fed algorithm with the measured radiation patterns at 429 and 697 MHz (where measurements were available), and the simulated radiation patterns at 29.6 and 109 MHz. Each estimation was made with 15 extracted signals, i.e., the number of snapshots is 15 ($K = 15$). I also used minimum description length

(MDL) criteria (Rissanen, 1978; Schwarz et al., 1978) to determine the number of impinging waves. Mostly, the criteria indicated one impinging wave which is the transmitted signal. In a few instances, when strong interference caused more than one signal being detected, I dropped the estimation. Finally, for each direction and frequency, at least 50 estimations were collected to calculate the mean values and root mean square (RMS) errors.

Fig. 2.10(a)–(c) give results at 30 MHz, (d)–(f) 109 MHz, (g)–(i) 429 MHz and (j)–(l) 697 MHz. The left column shows test results with transmitter on the ground, the middle column shows results with transmitter on the third floor of the garage ($H = 9.3$ m, $\theta = 74^\circ$ in Fig. 2.9(b)), and the right column on the fifth floor ($H = 14.6$ m, $\theta = 65^\circ$ in Fig. 2.9(b)). It can be seen that the mean value of the azimuth AoA, ϕ, increases roughly with a 15 degree step in each figure, and elevation AoA for each transmitter location, θ, drops from 90° to 65° accordingly, while keeping the same value for the same transmitter location.

For 429 MHz and 697 MHz tests, the RMS error decreases as the elevation angle decreases. For each elevation angle, the RMS error keeps a flat trend along azimuth angles. This agrees with the prediction of CRB pattern shown in Fig. 2.7. For 109 MHz, the RMS error is much larger when the transmitter is placed on the ledge of the concrete barrier on the third and fifth floor of the parking garage. This is due to the strong blockage caused by the building's walls. Specifically, at 429 MHz and 697 MHz, the length of transmitting antenna is much smaller than the distance between the ledge of the concrete barrier and the ceiling. However, at 109 MHz, the dipole is about 1.5 meter long and is roughly this distance, resulting in strong blockage and poor available SNR. The available SNR for the tests are shown in Table 2.1.

Also, the CRB values and the measured RMS errors of each elevation AoA and frequency are compared in Table 2.1. The CRB values are calculated with measured available SNR values and number of snapshots ($K = 15$) in the field tests. The CRB values and RMS errors are averaged over $\phi \in [0^\circ, 90^\circ]$ to get more comprehensive evaluation of the AoA estimation performance of the DF array. It is valid to do so because these values have been shown rather consistent at the azimuth angles.

Table 2.1: Available SNR, CRB and measured RMS errors in the field tests. These values are averaged over the azimuth angles

Freq. [MHz]	Elev. AoA [deg.]	CRB [deg.] θ	CRB [deg.] ϕ	RMSE [deg.] θ	RMSE [deg.] ϕ	SNR [dB]
29.6	90	11.0	30.6	7.1	63.9	71
	74	9.1	29.6	4.4	58	71
	65	8.5	33.4	4.9	66.2	70
109	90	3.4	4.2	1.2	2.4	53
	74	8.4	12.1	5.1	15.6	45
	65	4.9	8.7	3.9	4.1	49
429	90	1.0	0.8	0.8	0.9	36
	74	0.5	0.4	0.4	0.7	40
	65	0.3	0.3	0.2	0.0	40
699	90	1.1	0.9	0.2	1.0	35
	74	0.6	0.6	0.2	0.5	38
	65	0.4	0.6	0.8	0.8	37

The measured RMS errors and CRB values are within the same magnitude, and demonstrate a similar trend.

2.5 Conclusion

In this chapter, I proposed an electrically-small antenna array that provides the direction finding (DF) capability of estimating elevation and azimuth angles of an incident electromagnetic wave. This DF capability is free of error caused by cross polarization of the incident wave. I compared many candidate topologies of small-aperture antenna array to pick up those with the proposed DF capability. Then, I calculated their CRB over a wide frequency range and selected the topology with the lowest CRB. This selected array is composed of four vertical monopoles and two horizontal dipoles. The antenna elements of the array were carefully optimized in fullwave simulation to make better use of the volume and to obtain better impedance matching especially at the lower frequencies. The proposed

DF array can be enclosed by a box with dimensions of 14 cm×14 cm×5.5 cm. I evaluate the array's AoA estimation accuracy in simulation and measurement over a frequency range of 30–2000 MHz by examining the Cramer-Rao bound (CRB). Further, I did DF field tests in an outdoor environment with the fabricated prototype at many AoAs, from 30 to 700 MHz. In the frequency range of 400–2000MHz, the array typically has accuracy levels of 0.1°–1° for an SNR level of 25 dB and number of snapshots of 100. In the frequency range of 30–400 MHz, the array typically has accuracy levels of 1°–30° for an SNR level of 60 dB and number of snapshots of 100.

Throughout the design procedure, many factors related to both DF and antenna array design are considered. These factors include the capability of estimating azimuth AoA, elevation AoA and polarization of impinging waves, near-zenith field of view (FoV), Cramer-Rao bound (CRB), antenna bandwidth, and electrically-small antenna design. The design procedure can be a good reference of other related research.

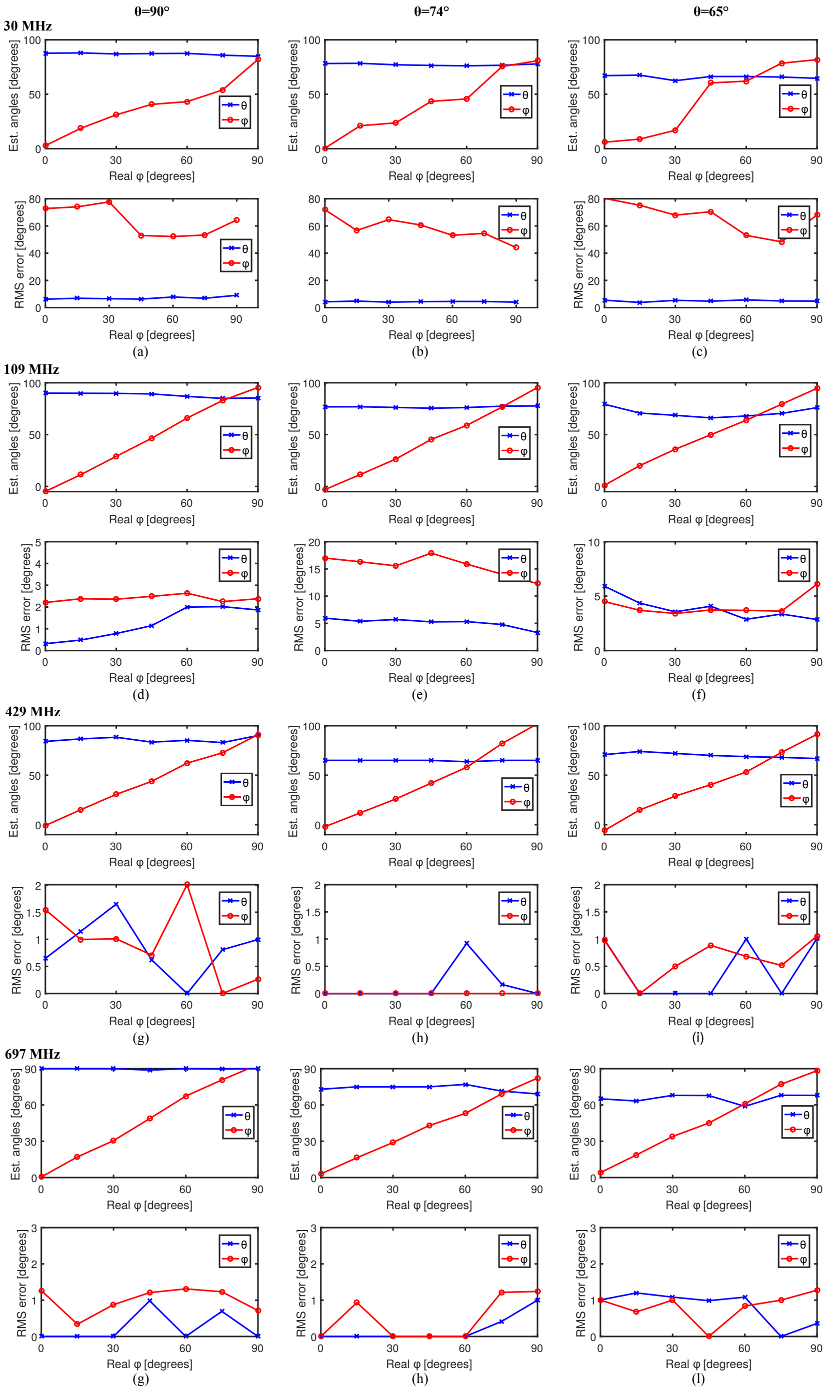

Figure 2.10: Direction finding field test results. Mean values and the RMS errors of the estimated AoAs and tilt angle at (a)–(c) 30 MHz, (d)–(f) 109 MHz, (g)–(i) 429 MHz and (j)–(l) 697 MHz. The left column shows results with antenna putting on the ground; the middle column shows those on the 3rd floor of a nearby garage; the right column shows those on the 5th floor of the garage.

3 DESIGN OF PLATFORM-BASED HF DIRECTION-FINDING ANTENNAS USING THE CHARACTERISTIC MODE THEORY

3.1 Introduction

Direction finding (DF) systems are widely used at the high frequency (HF), very high frequency (VHF), and ultra high frequency (UHF) bands. Determining the direction of arrival and locating the source of the emitter are extremely useful in many surveillance, electronic warfare support, rescue, navigation, and geolocation applications among others. However, due to the large wavelengths of electromagnetic waves at HF frequencies (3–30 MHz), it is often challenging to deploy DF arrays having physically-large receiving elements on platforms. In such situations, platform-based HF antennas are often electrically small and suffer from the well-known limitations of electrically-small antennas such as narrow bandwidth and low radiation efficiency (Chu, 1948; Harrington, 1960; Yaghjian and Best, 2005). However, some of the deficiencies of electrically-small antennas can be compensated by exploiting the presence of the platform and using it as a major part of the antenna.

The concept of employing the platform itself as the antenna has been examined before. Chen and Wang (2015b) excited radiating currents on a ship to achieve certain desired radiation patterns. In the papers authored by Shih and Behdad (2017), Shih and Behdad (2016), and Li and Behdad (2017), the platform was excited as a radiating part of the antenna, and hence, enhanced the bandwidth of HF and VHF antennas. Similarly, in antenna designs for cell phones, multiple characteristic modes of the handset's chassis and/or ground plane were also exploited to achieve multi-band features and enhanced bandwidth (Miers et al., 2013; Rahola and Ollikainen, 2006). Moreover, the orthogonality feature of these chassis modes has been widely employed in MIMO antenna design to reduce mutual coupling, and to improve the independence of the radiation patterns between the MIMO antennas (Kishor and Hum, 2013; Chaudhury et al., 2007; Li et al., 2014). These papers successfully employed the characteristic mode (CM) theory to design platform-based antennas with improved performance levels compared to what could be achieved from standalone antennas. However, these prior works did not examine the use of characteristic mode theory in designing platform-based DF systems. Svantesson (2000), and Pöhlmann et al. (2017), investigated utilizing multi-mode antennas for DF purposes. In fact, a platform-based antenna array can be thought of as a special type of multi-mode antenna that uses the platform as the multi-mode radiator. However, these previous studies neither investigated the design of multi-mode antennas specially suitable for DF nor used a real platform as the main radiator. Similarly, in the study reported by Corbin (2011), the strategic placement of monopoles on an airplane was investigated as a means of enhancing the DF accuracy. The DF accuracy improvements were attributed to the positive effects of the platform. However, deliberately employing the platform's CM as the effective elements of a DF array was not investigated. More importantly, none of the above mentioned papers did consider the impact of the polarization of impinging waves and the field of view (FoV) of the DF system. These two factors are essential parameters of platform-based DF systems, particularly those mounted on airborne platforms. Failure to consider these issues may dramatically degrade the performance of a DF system in realistic operational environments.

In this chapter, I propose a systematic method for exploiting the characteristic modes of a platform and use them as effective elements of a platform-based DF antenna array operating at the HF band. In this approach, the outline of which I first reported by Ma and Behdad (2018a), I first use the characteristic mode theory to identify the significant CMs of a platform at the desired operating frequency. Subsequently, a subset of the CMs that provides the lowest Cramer-Rao bound (CRB) is selected for DF. In this approach, I assume that each CM is one element of the DF array. The CRB is a good predictor of the angle-of-arrival (AoA) estimation accuracy of DF systems (Weiss and Friedlander, 1991). To determine the suitable subset, I average the CRB value over the entire FoV and possible polarization states of the impinging wave. This enables us to improve the DF performance of the system while quantitatively considering the FoV and polarization.

In Section 3.2, I first review the statistical model and describe the average CRB metric used for evaluating the platform-based arrays. In Section 3.3, I describe the design approach in detail, including the mode selection procedure and coupling element design. In Section 3.4, I demonstrate the use of this design approach by performing characteristic mode analysis of a mid-size aircraft at 10 MHz. A brief discussion on tracking the CMs over a frequency range is included. I demonstrate that some of the subsets of this platform's CMs provide significant DF performance advantages over other subsets. A scaled-model prototype of this platform is also fabricated and characterized. Its measurement results are used to perform DF tests in an emulated environment. I compare the CRB values of the DF system that uses the pure CMs with those of a practically-realizable system. Both results are also compared with the CRB values of 1:100 scaled-model prototype (at the scaled frequency). Monte-Carlo tests demonstrate that the proposed approach can produce a practical platform-based DF system whose accuracy approaches that of a system using the pure CMs of the platform. In Section 3.5, the measured and simulated DF performance of this system are compared across the entire HF band.

3.2 Statistical Model and CRB of Platform-based Antenna Arrays

Statistical Model

Let us assume that the electric field of an impinging wave is denoted by:

$$\begin{aligned} E &= \hat{\theta} E_\theta + \hat{\phi} E_\phi \\ &= a(t) e^{j\omega_0 t} [\hat{\theta} \cos(\gamma) e^{j(\psi(t)+\eta)} + \hat{\phi} \sin(\gamma) e^{j\psi(t)}] \end{aligned} \tag{3.1}$$

where (as shown in Figure 3.1) $\hat{\theta}$ and $\hat{\phi}$ denote the unit vectors of elevation and azimuth angles in the spherical coordinate system, respectively; $a(t)$, ω_0, and ψ denote the amplitude, frequency, and phase of the impinging wave, respectively; γ and η are the tilt angle and the phase difference of the two components of the

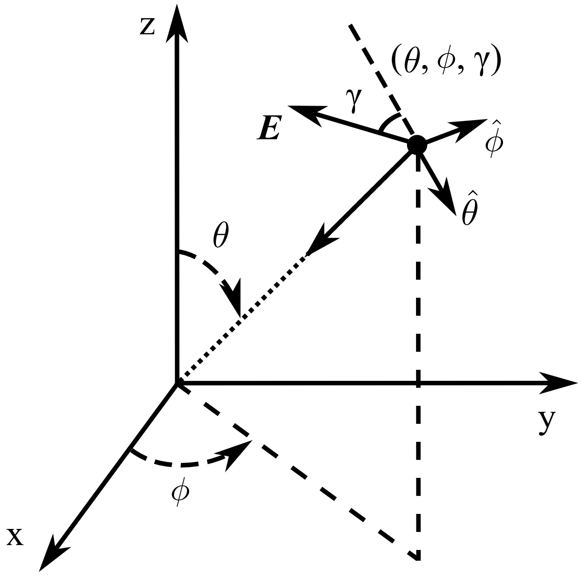

Figure 3.1: Spherical coordinate system notations. The azimuth angle ϕ, elevation angle θ, and tilt angle γ of an impinging, linearly-polarized wave are shown.

electric field of the impinging wave. The received voltages at the feed ports of an M-element antenna array are given by:

$$\mathbf{X}(t) = \mathbf{A}_\theta(\theta, \phi)\mathbf{E}_\theta(t) + \mathbf{A}_\phi(\theta, \phi)\mathbf{E}_\phi(t) + \mathbf{n}(t) \tag{3.2}$$

where $\mathbf{X}(t) = [x_1(t), x_2(t), \cdots, x_M(t)]^T$ denotes the vector of the voltages measured at the M elements of this array at time $t = 1, 2, \cdots$; $\mathbf{A}_\theta$ and $\mathbf{A}_\phi$ ($M \times N$ matrices) denote the θ and ϕ components of complex radiation patterns; N is the number of impinging waves; $\mathbf{E}_\theta(t)$ and $\mathbf{E}_\phi(t)$ (N-dimensional vectors) denote the θ and ϕ components of the N impinging waves; $\mathbf{n}(t)$ (M-dimensional vector) is assumed to be Gaussian white noise with variance matrix of $\sigma^2\mathbf{I}$ ($\mathbf{I}$ is identity matrix).

This statistical model describes an M-element array with N waves impinging on it. This array is composed of arbitrary types of antenna elements with diverse polarizations (Ferrara and Parks, 1983). Similarly, in my approach, I use one CM as one element of the platform-based antenna array. As a result, these elements usually have different polarizations and shapes of radiation patterns, making the aforementioned statistical model perfectly suitable for the platform-based antenna arrays I investigate in this work.

CRB of Platform-Based Antenna Arrays

According to Weiss and Friedlander (1991) and Ferrara and Parks (1983), the CRB of the array modeled in Section 3.2 is the inverse of the Fisher Information Matrix (FIM) which is given element-by-element by:

$$F_{mn} = K \cdot \mathbf{tr} \left\{ \mathbf{R}_x^{-1} \frac{\partial \mathbf{R}_x}{\partial p_m} \mathbf{R}_x^{-1} \frac{\partial \mathbf{R}_x}{\partial p_n} \right\} \tag{3.3}$$

where K denotes the number of snapshots, and p_m represents the m-th parameter of the model. These parameters include the AoAs of the N impinging waves denoted by $\boldsymbol{\theta} = [\theta_1, \theta_2, \cdots, \theta_N]^T$ and $\boldsymbol{\phi} = [\phi_1, \phi_2, \cdots, \phi_N]^T$, and the polarization denoted by γ and η. $\mathbf{R}_x$ is given by:

$$\mathbf{R}_x = \mathbf{A}\mathbf{R}_s\mathbf{A}^H + \sigma^2\mathbf{I} \tag{3.4}$$

where $\mathbf{R}_x$ ($M \times M$ matrix) is the covariance matrix of $\mathbf{X}$; $\mathbf{A} = [\mathbf{A}_\phi, \mathbf{A}_\theta]$ ($M \times 2N$ matrix) is the full radiation pattern; $\mathbf{R}_s$ ($2N \times 2N$ matrix) is the signal covariance matrix; and $\mathbf{R}_s \triangleq \overline{\mathbf{S}\mathbf{S}^H}$ where $\mathbf{S} = [E_\phi(t), E_\theta(t)]^T$ and the expectation operator $(\overline{\cdot})$ is with respect to time (t). Here, I assume the signals' amplitudes are wide-sense stationary random variables. After the FIM is computed, CRB is calculated by taking the inverse of the FIM as:

$$\mathbf{CRB} = \mathbf{F}^{-1}, \tag{3.5}$$

and

$$\mathbf{F} \triangleq \{F_{mn}\}. \tag{3.6}$$

Average CRB of Platform-Based Antenna Arrays

The CRB matrix of (3.5) varies with AoAs and the impinging waves' polarization states. Therefore, to be used as a figure of merit, this CRB is first averaged over the entire FoV and all possible polarization states. A weighted average may be more appropriate if the impinging wave is more likely to have a specific type of polarization. Then, the sum of this averaged CRB matrix's azimuth and elevation AoA elements can be used as a figure of merit. This idea is mathematically described as:

$$\mathbf{CRB}_{avg} \triangleq \frac{\int p(\gamma,\eta)d\gamma d\eta \int_{\Omega} \mathbf{CRB}(\theta,\phi,\gamma,\eta)\sin(\theta)d\theta d\phi}{\Omega} \tag{3.7}$$

$$\mathrm{CRB}_{AoA} \triangleq \mathrm{CRB}_{avg,\theta\theta} + \mathrm{CRB}_{avg,\phi\phi} \tag{3.8}$$

where $\mathbf{CRB}_{avg}$ denotes the weighted average CRB matrix; $\mathbf{CRB}(\theta,\phi,\gamma,\eta)$ is the CRB matrix formulated by Weiss and Friedlander (1991) and copied in (3.3)-(3.6); θ, ϕ are the elevation and azimuth AoA respectively; $p(\gamma,\eta)$ is the probability density function (PDF) of polarization states, which are assumed to be independent and identically distributed; Ω is the FoV; CRB_{AoA} is the scalar average CRB; and $\mathrm{CRB}_{avg,\phi\phi}$ and $\mathrm{CRB}_{avg,\theta\theta}$ are the ϕ and the θ components of $\mathbf{CRB}_{avg}$ respectively. $p(\gamma,\eta)$ and Ω are assumed known. For example, let us assume that there is only one linearly-polarized incident wave, and that only the accuracy of azimuth AoA is of interest. In this case, I assume $N = 1, \eta = 0$, and I only estimate ϕ. According to Weiss and Friedlander (1991), the $\mathbf{CRB}_{avg}$ should be computed for all the unknown variables, i.e. θ, ϕ, and γ. Therefore, $\mathbf{CRB}_{avg}$ is a 3×3 matrix. However, only its ϕ component (diagonal element), $\mathrm{CRB}_{avg,\phi\phi}$, will be used to evaluate the system performance. In a slightly different case, if both elevation and azimuth AoAs are of interest, I should further include the θ component of $\mathbf{CRB}_{avg}$ by calculating the CRB_{AoA} with (3.8).

3.3 Design of the Platform-Based Antenna Array

The CM theory states that a plane wave impinging on a platform induces a superposition of CMs on the platform. The weights of these CMs depend on the AoA and polarization of the incident wave (Cabedo-Fabres et al., 2007; Garbacz, 1965). As a result, by measuring these weights, the AoA and polarization state can be estimated. However, it is more practical to measure a small subset of these weights, since in practice measuring all of them requires using a significant number of coupling elements and a receiver with the same number of coherent channels. One possible approach to utilize these CMs is to measure a series of different combinations of the CMs rather than a series of pure CMs. In this case, each coupling element is designed to excite a given combination of the CMs of the platform with specific complex weights. Therefore, each CM combination performs effectively as a virtual antenna elements, and the set of the different combinations acts effectively as a virtual antenna array. Among all possible sets of different CM combinations, the one that provides the best DF performance can be identified and measured with properly designed, platform-based antennas. However, this approach requires designing platform-based antennas that can accurately excite (or receive) a given combination of pure CMs of the platform. Doing this in practice is rather challenging as the platform-based antennas must excite the desired combination of the CMs with precisely-determined complex excitation coefficients. In contrast, the excitation of the dominant CMs of the platform is a somewhat straightforward process that has been extensively investigated in the past[1]. Therefore, I propose to excite a subset of the platform's CMs (rather than a set of different combinations of the CMs) as a virtual antenna array for direction finding. Among all these subsets, the one that provides the lowest CRB should be adopted to achieve the lowest AoA estimation error for a given field of view.

This subset can be determined in two steps. First, the infinite set of CMs is

---

[1] This statement refers to situations where the coupling elements primarily excite one dominant mode of the platform and the contributions of other excited modes are small. Notice that exciting a pure CM mode of the platform without inadvertently exciting other modes (albeit less efficiently) is also a challenging task.

truncated to a finite set. All the CMs should be identified by CM analysis, and then the CMs with modal significance (MS) values smaller than a certain value are abandoned. A smaller MS value indicates that the corresponding CM is further away from resonance, tending to contribute less to the overall induced currents (Chen and Wang, 2015a). Moreover, the CMs with smaller MS values have larger quality factors (Qs). As reported by Nordebo et al. (2006), the DF accuracy benefits of including these high-Q modes can be limited by their large Qs. For a given bandwidth, these modes cannot achieve good impedance matching or SNR due to their excessively high quality factors. Consequently, the CMs with small MS values and large Qs contribute little to the improvement of CRB. Although the designer has the freedom of choosing the criterion of MS value, it is a good practice to set this value as 0.7, which corresponds to the threshold MS value above which a mode can be considered to be significant (Cabedo-Fabres et al., 2007). CMs with MS values less than 0.7 can be omitted in radiation pattern synthesis without introducing significant error (Chen and Wang, 2015a). In the second step, let us assume that the number of receivers is smaller than the number of the CMs identified in the first step. This is usually a valid assumption. A platform that is a few wavelengths long at the operating frequency usually has several CMs with MS values larger than 0.7. In such a case, scalar average of CRBs ($\mathrm{CRB}_{\mathrm{AoA}}$) of all the combinations may be computed with (3.3)-(3.8). Then, the combination with the lowest CRB value will be chosen as the one providing a good compromise between accuracy, and implementation complexity (i.e., designing coupling elements to excite the subset of modes).

After this, coupling element(s) can be designed to excite each of these CMs. In this case, the coupling element(s) used to excite each CM will interface with one channel of a multi-channel receiver. The method for designing the coupling elements to excite specific CMs has been thoroughly investigated in the past (Chen and Wang, 2015b,a; Martens et al., 2011; Cabedo Fabres, 2008; Manteuffel and Martens, 2016). Due to the limited length of the chapter, I only summarize the important conclusions of these previous works here. Specifically, to excite a given characteristic mode, an inductive coupling element (ICE) is to be placed at a location where the current density of the specific mode is strong. Alternatively, a capacitive coupling element (CCE) is to be placed where the charge density of a given mode is maximum (i.e., the current density is minimum). If no desired distribution is provided naturally by the platform, small modifications can be made to the platform to create the desired current and charge distributions. This latter point, however, will not be used as a design rule in this chapter since making fundamental structural modifications to the platform (i.e., cutting sections of the platform) may not be acceptable in many real-life applications.

3.4 Design Example: HF DF Array Design for a Medium-Size Aircraft

To demonstrate the design principles outlined before, I provide a design example in which an HF DF antenna array for a medium-size aircraft is designed. Without loss of generality, I select a twin-engine jet aircraft similar to the Boeing 737 to perform this demonstration. This aircraft has an aluminum body with a length of 42 m and a wing span of 34 m. A simplified model used in simulations is shown in Figure 3.2. Detailed dimensions of this platform may be found in a hand book published by Boeing Commercial Airplanes (2004). In this specific design example, my goal is to design a platform-based antenna array for an on-board DF system, which has a four-channel coherent receiver. Moreover, the initial design frequency of 10 MHz is chosen and the array is assumed to be used to estimate the direction of arrival of a single, randomly-polarized wave. The FoV of the DF system is assumed to be the full sphere (i.e., a solid angle of 4π Sr.).

Design Procedure

The design procedure is as follows. First, I performed CM analysis for this aircraft to find out all the CMs with MS$\geqslant$0.7 (at 10 MHz). In this example, the simplified aircraft model was simulated with FEKO 7.0 and found to have six modes with MS$\geqslant$0.7. FEKO is a commercially-available, full-wave electromagnetic simulation

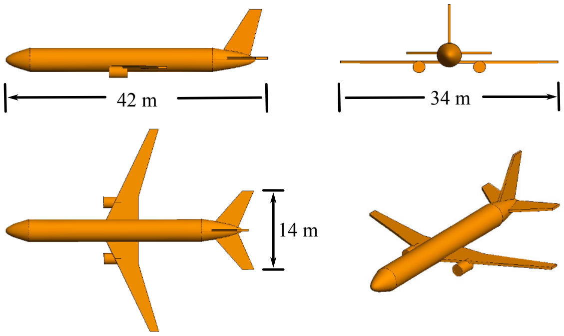

Figure 3.2: The simplified medium-size airplane model used in the present work and its dimensions.

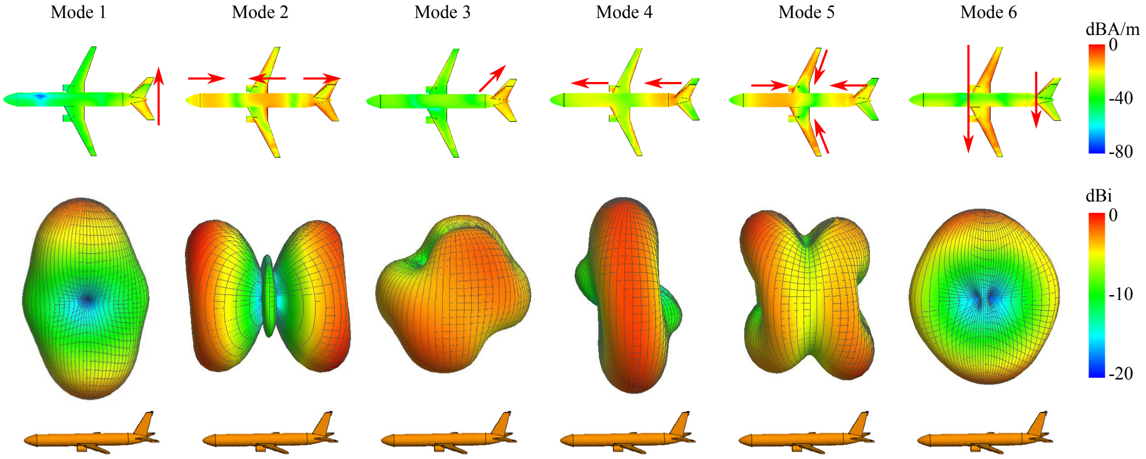

Figure 3.3: Surface current distribution and the radiation patterns of the first six significant characteristic modes (MS$\geqslant$0.7) of the platform shown in Figure 3.2 at 10 MHz. The red arrows show the directions of the electric current flow.

software. The CM analysis is done by using its built-in CM solver, where the CMs are calculated by extracting the eigen-vectors of the method-of-moments (MoM) impedance matrix. The normalized current distributions and radiation patterns of these modes are shown in Figure 3.3. FEKO 7.0's CM solver tracks the CMs over the frequency range by correlating the CMs calculated at different frequencies, according to the release note of FEKO 7.0 publised by EM Software & Systems-S.A. (Pty) (2014). However, this mode tracking issue can also be addressed by connect-

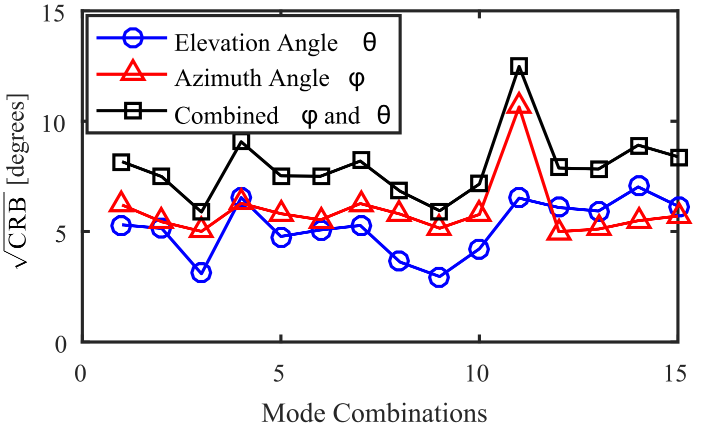

Figure 3.4: Average Cramer-Rao bound values for direction finding with different combinations of the characteristic modes. The specific modes included in each combination is provided in Appendix.

ing the decompositions of the method-of-moments (MoM) impedance matrices at adjacent frequencies with an ordinary differential equation (ODE) derived from the impedance matrix's inherent continuity over the frequency (Gohberg et al., 1986; Yang and Ajjarapu, 2007; Dieci and Eirola, 1999; Bindel et al., 2005). These ODE-based approaches can be generally separated into two categories, i.e., the continuation of invariant subspaces (Yang and Ajjarapu, 2007), and smooth matrix decomposition (Dieci and Eirola, 1999). Since I am using a commercially-available software to perform CM analysis and the design is performed at a single frequency, specific method used for mode tracking in FEKO is not of any concern in the present work.

After completing the aforementioned CM analysis, I select four modes out of the modes found out in the first step and shown in Figure 3. The selected combination needs to have the lowest CRB_{AoA} proposed in (3.8). I assume that the field of view of the DF antenna array is the full sphere, and that a single impinging wave with linear, randomly-oriented polarization has a random direction of arrival. This assumption can be mathematically expressed as $p(\gamma, \eta) = 1$, $\theta \in [0, \pi]$, $\phi \in [0, 2\pi]$ (in (3.7)), and $N = 1$. Then the $\mathbf{CRB}_{avg}$ is a 3×3 matrix with one column for θ,

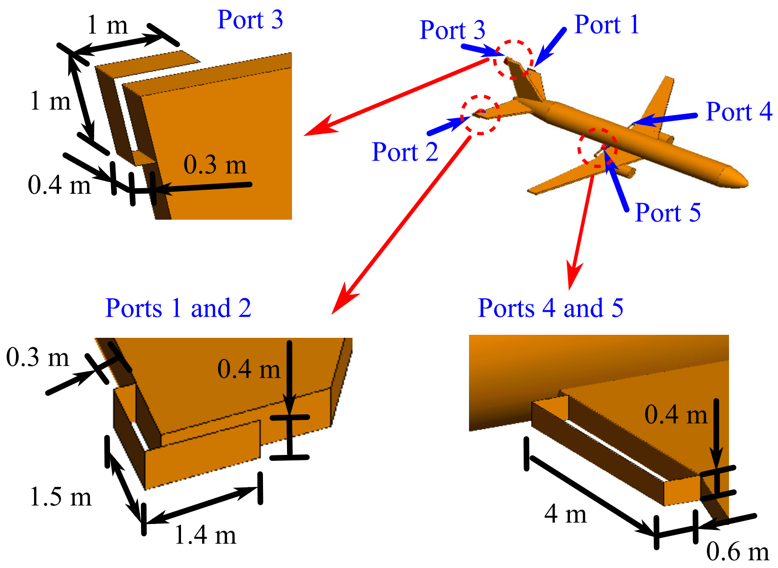

Figure 3.5: Topology of the coupling elements used to excite the desired characteristic modes of the platform and their dimensions. These coupling elements jointly excite the four selected modes (Modes 1, 2, 3, and 6).

one for ϕ, and the other for γ. In this case, there are $\binom{6}{4} = 15$ mode combinations in total. Their CRB_{AoA} values can be computed with (3.3)-(3.8). The square root of these values ($\sqrt{\text{CRB}_{\text{AoA}}}$) are shown in Figure 3.4. The different modes included in each combination indicated in Figure 4 are provided in the Appendix.

As can be seen from Figure 3.4, the $\sqrt{\text{CRB}_{\text{AoA}}}$ value varies considerably from combination to combination. In fact, the largest value is 12.5° (for Combination 11) while the smallest is 5.9° (for Combination 3). In other words, when used in a DF system, an antenna array implementing Combination 11 is expected to have twice the average error of an antenna array implementing Combination 3. In this specific example, Combination 9 has an average CRB value that is only slightly larger (0.06°) than that of Combination 3. Therefore, choosing Combination 9 may also be justifiable if exciting the specific CMs included in this subset is easier in practice than exciting the CMs of Combination 3. In this example, however, exciting Combination 9 is not any simpler than exciting Combination 3. Specifically, Combination 3 consists of Modes 1, 2, 3 and 6, whereas Combination 9 consists of Modes 1, 3, 5 and 6 (shown in Figure 3.3). As can be seen, Mode 2 has strong currents on the rear edge of the wings while Mode 3 on the front edge near the airplane body. Mode 2 shares more locations having strong current and charge distributions with Modes 1, 3, and 6, as compared with those locations that Mode 3 shares with Modes 1, 5 or 6. Coupling elements placed on these locations may be used for exciting multiple modes. Therefore, to reduce the number of coupling elements, Combination 3 is finally adopted.

In the next step of the design process, I design the coupling elements required to excite the selected modes. To reduce the number of coupling elements, these modes should share coupling elements if possible. The final design of the coupling elements is shown in Figure 3.5. The reason for adopting this specific arrangement of coupling elements is as follows. Mode 1 is a dipole mode of the horizontal stabilizers. Therefore, two CCEs are placed at the rear ends of the stabilizers, and are fed with a 180° phase difference. These CCEs may also be used to excite Modes 2 and 6 later with different feeding schemes. This is the reason that I use two CCEs rather than a single ICE placed at the rear end of the airplane body between two horizontal stabilizers. Mode 2 is the third-order resonance of the airplane body. This mode can be excited with two ICEs at the rear edges of the body (shown in Figure 3.5), together with the two CCEs for Mode 1. The two ICEs I used here will be reused for exciting Mode 6. That is why I do not place multiple ICEs along the airplane body that modal current flows along. Mode 3 is a dipole mode of the whole tail. The modal currents flow from the vertical stabilizer to horizontal stabilizers. To excite this mode, I put a new CCE at the end of the vertical stabilizer. Then, I feed this new CCE and the CCEs located on horizontal stabilizers with 180° phase difference. Mode 6, as shown in Fig 3.3, consists of two currents going through wings and horizontal stabilizers. This mode can be excited by feeding the ICEs on the wings and the CCEs on the horizontal stabilizers with 180° phase difference. No additional coupling element is needed for exciting this mode. The excitation schemes are summarized in Table 3.1. There are in total five CCEs/ICEs jointly exciting the four modes, which is an efficient way of using the coupling elements.

Table 3.1: Excitation coefficients of ports for exciting the selected CMs.

	Port 1	Port 2	Port 3	Port 4	Port 5
Mode 1	1	-1	-	-	-
Mode 2	1	1	-	1	1
Mode 3	1	1	$-\sqrt{2}$	-	-
Mode 6	-	-	-	1	-1

Table 3.2: The component values of the matching networks of the fabricated scaled model at 425, 1000 and 3000 MHz (4.25, 10 and 30 MHz respectively for the full-scale model).

Frequency [MHz]	425	1000	3000
X_1	1.5 pF	short	short
X_2	36 nH	3.0 pF	0.6 pF
X_3	36 nH	24 nH	0.9 pF
X_4	1.0 pF	short	short
X_5	36 nH	3.3 pF	0.5 pF
X_6	36 nH	24 nH	3.9 pF
X_7	short	2.0 pF	short
X_8	6.8 nH	1.5 pF	2.2 nH
X_9	4.3 pF	1.2 pF	2.7 pF

Finally, matching networks for the coupling elements are designed. A regular passive matching network composed of lumped elements is inserted right after each coupling element. The matching networks are regular L- and T-shaped matching networks composed of lumped capacitors and inductors. The design method has been well established and explained in many textbooks. Thus, I do not repeat it here for brevity. I directly provide the matching networks' topology and the values of the components in Figure 3.6 and Table 3.2. Table 3.2 lists the component values for a 1:100 scaled model.

Table 3.3: Normalized weighting coefficients of excited modes.

		Pure mode					
		1	2	3	4	5	6
Excited mode	1	1	-	-	-	-	0.5
	2	-	1	0.3	-	-	-
	3	-	0.3	1	0.3	-	-
	6	0.5	-	-	-	-	1

Other values < 0.1

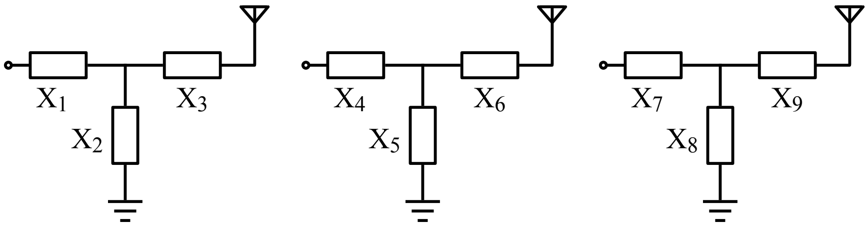

(a) (b) (c)

Figure 3.6: Topologies of the matching networks used to impedance match the coupling elements at (a) Ports 1 and 2, (b) Port 3, and (c) Ports 4 and 5.

Radiation Patterns and CRB Comparison

The radiation patterns of these excited modes were computed by FEKO 7.0 with its build-in MoM solver, instead of the CM solver. Numerical solvers using the CMs as basis functions may have a convergence problem when excitation sources are involved. This is due to the lack of CMs which can be used to describe the behavior of the source current at the feed-point location(s) (Yee and Garbacz, 1973; Cabedo-Fabres et al., 2004). However, by using regular MoM solver, I circumvented this convergence problem. These patterns are shown in Figures 3.7(a)-3.7(d), which demonstrate a good agreement with those of the selected pure modes. This can also be verified by examining the weighting coefficients of the excited modes. Weighting coefficient, in the CM theory, indicates the weights of the CM currents in the excited current. The weights of the radiated power of CMs in the total radiated power are proportional to the square of the weighting coefficients. The weighting coefficients

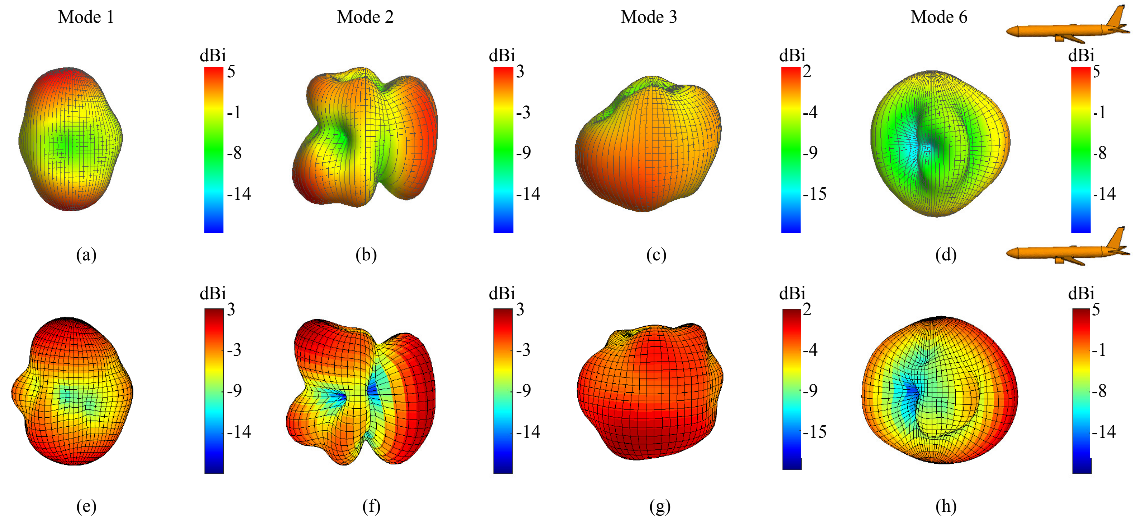

Figure 3.7: (a)-(d) Simulated realized-gain radiation patterns of the excited modes on the full-scale platform. (e)-(h) Measured realized-gain patterns of the excited modes on the scaled-model platform. The small aircraft model on the right hand side of each row shows the relative orientation of the radiation patterns with respect to the platform.

are shown in Table 3.3 (each row of these coefficients has been normalized to the largest value of the row). As shown in Table 3.3, the weights of radiated power contributed by undesired modes are less than 25%.

A 1:100 scaled model of the aircraft was 3-D printed in plastic and covered with copper tape. The scaled coupling elements were also fabricated and mounted on the corresponding locations on the platform as shown in Figure 3.5. Photographs of this fabricated prototype are shown in Figure 3.8. The matching networks were placed right next to the coupling elements (as shown in Figure 3.8) and are embedded within the hollow 3-D printed platform and shielded from the outside environment by the metallic outer surface of the platform. Their topologies and the component values are shown in Figure 3.6 and Table 3.2. Coaxial cables were used to connect the matching networks to the feed ports in the belly area of the aircraft. The feeding coaxial cables are also embedded within the hollow 3-D printed airframe and only the connectors are outside (see Figure 3.8) to allow for interfacing with the test

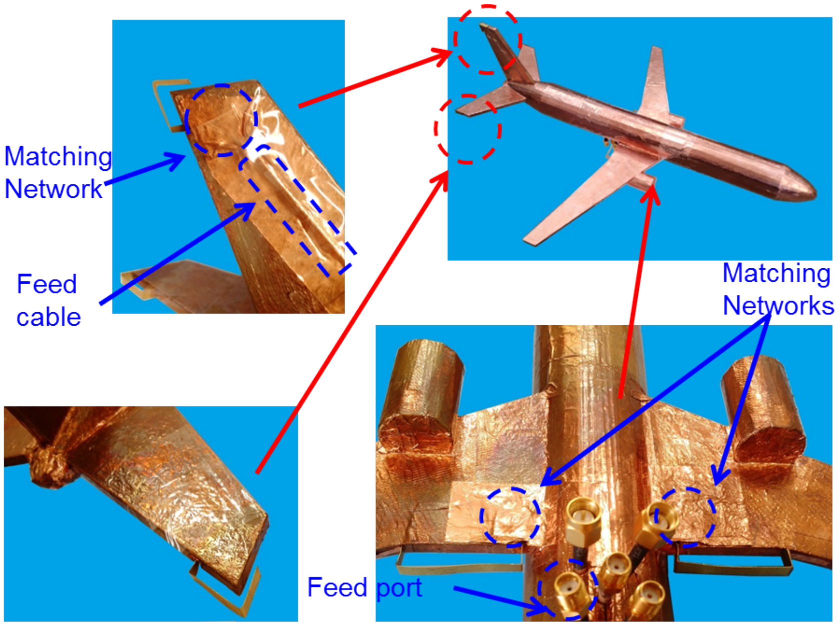

Figure 3.8: Photographs of a 1:100 scaled-model fabricated prototype. The body is 3-D printed in plastic and covered with copper tape. Passive matching networks are embedded in the body next to the coupling elements. Feed ports are placed beneath the airplane's belly and connected to the matching networks with coaxial cables, which are also embedded inside the hollow platform.

setup.

In the measurements, I fed the coupling elements with commercially available 2-way 0° and 180° power splitters (i.e., Mini-Circuits ZX10-2-252-S+ and ZFSCJ-2-232-S+ respectively). Specifically, as shown in Figure 3.9(b), Modes 1 and 6 were excited with a 180° power splitter, respectively. To measure Mode 2, I did two sets of measurements and then summed the results. In one measurement, I fed Ports 1 and 2 with a 0° power splitter. In the other one, I fed Ports 4 and 5 with a 0° power splitter. Mode 3 was measured in a similar way. In one measurement, I fed Ports 1 and 2 with a 0° power splitter. In the other one, I fed Port 3 only. After measuring the completed three-dimensional radiation patterns (both magnitude and phase), I subtracted one field pattern from the other (coherent subtraction of the complex

Table 3.4: $\sqrt{\text{CRB}}$ of the selected pure modes, the excited modes in simulation, and the excited modes in measurement.

	Pure CMs	Excited modes (Simulation)	Excited modes (Measurement)
El. angle θ	3.1°	3.5°	3.5°
Az. angle ϕ	5.0°	5.1°	5.3°
Overall	5.9°	6.2°	6.4°

Available SNR $= 25$ dB, number of snapshots $K = 1$.

field values was performed).

The three-dimensional realized gain patterns (both magnitudes and phases) of the fabricated prototype were measured with a multi-probe near field system (SATIMO StarLab). The measurement setup is shown in Figure 3.9. Measured patterns are shown in Figures 3.7(e)-3.7(h). These measured patterns show a good agreement with the simulated ones shown in Figure 3.7(a)-(d).

Next, I calculated the CRB_{AoA} following (3.3)-(3.8). I computed the CRBs with the radiation patterns of the pure characteristic modes, the simulated radiation patterns of excited modes, and the measured 3-D radiation patterns (including the magnitude and phase information) of the fabricated scaled model. All of the CRBs were computed under the assumption of available signal-to-noise ratio (SNR) is 25 dB and the number of snapshots of $K = 1$. The available SNR is defined as the SNR that a receiver has when the realized gain of the receiving antenna is 0 dBi. Using $K = 1$ does not affect the general solutions because the CRB is inversely proportional to K (see (3.3), (3.5) and (3.6)) (Weiss and Friedlander, 1991). The results are given in Table 3.4.

As can be seen, the average CRB value (CRB_{AoA}) of the selected pure CMs, that of the excited modes in simulation, and that of the fabricated scaled model are very close to each other. Nevertheless, there is still small differences among these values. The pure CMs have the lowest CRB, which means the best AoA estimation accuracy. This is not unexpected since these pure modes are selected to do so (Figure 3.4). Since the excited modes are not 100% pure (as shown in Table 3.3), they are expected to have slightly larger CRB values. Moreover, the CRBs of the

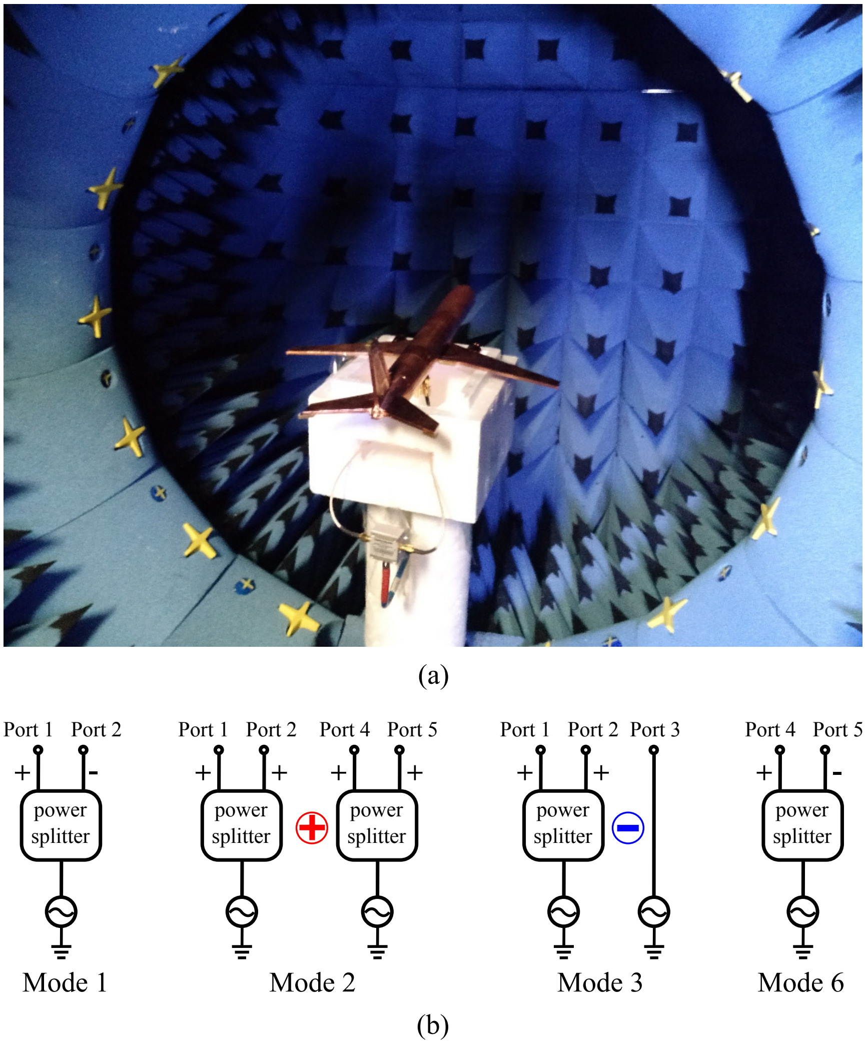

Figure 3.9: (a) Photograph of the fabricated scaled-model prototype in the spherical near-field measurement setup. (b) The feeding networks used to characterize the 3-D radiations (magnitude and phase) of the platform-based DF antenna array.

fabricated prototype are slightly larger than those of the simulated one. This slight degradation is primarily due to the losses of the matching networks and those of the power dividers used to feed multiple coupling elements. The $\hat{\theta}$ and $\hat{\phi}$ components of the average CRB (i.e. $\sqrt{\mathrm{CRB}_{avg,\theta\theta}}$ and $\sqrt{\mathrm{CRB}_{avg,\phi\phi}}$ respectively) are depicted

Table 3.5: CRB and Monte Carlo test results for three randomly selected AoAs and polarization states.

Real angles [deg.]			$\sqrt{\text{CRB}}$ [deg.]			Estimated angles [deg.]			RMS error [deg.]		
θ	ϕ	γ	θ	ϕ	γ	θ	ϕ	γ	θ	ϕ	γ
30	**60**	**60**	0.14	0.27	0.42	**30.0**	**59.9**	**60.0**	0.0	0.5	0.6
50	**70**	**60**	0.14	0.19	0.40	**50.0**	**72.0**	**60.0**	0.2	0.2	0.4
120.5	**257**	**30**	0.17	0.36	0.34	**121.4**	**256.6**	**30.1**	1.2	0.8	0.4

Available SNR = 25 dB, number of snapshots $K = 100$.

as a function of AoA in Figure 3.10. In this figure, the aircraft is heading towards $+\hat{\mathbf{y}}$ direction as shown by the blue arrows.

Note that relatively large errors can be observed in $+\hat{\mathbf{y}}$ direction. The CRB in the vicinity of this direction can be improved by using other mode combinations. For example, if I apply the proposed approach with the assumption that the FoV is a narrow band along the $+\hat{\mathbf{y}}$ direction, i.e., $\theta \in [80^\circ, 100^\circ]$ and $\phi \in [80^\circ, 100^\circ]$, Combination 7 can be found to provide an averaged CRB of 1° smaller than that of Combination 3. Moreover, for polarization tilt angle of 30° and 60°, the CRB patterns exhibit a low-error region along the $+\hat{\mathbf{y}}$ direction, rather than a high-error region along this direction as shown in Figures 3.10, 3.11 and 3.12. However, for vertically-polarized incident waves (i.e., $\gamma = 0^\circ$), the large error in the vicinity of $+\hat{\mathbf{y}}$ direction results from the physical limitations of the platform. These limitations are attributed to the fact that a vertically-polarized electromagnetic wave incoming from the front of the airplane can hardly excite currents on most parts of the airplane (except the vertical stabilizer), which are predominantly oriented perpendicular to the electric field of the incident wave.

Monte Carlo Tests

Monte Carlo tests were performed to further verify the DF capability and AoA estimation accuracy of this platform-based antenna array. These results demonstrate that: 1) This platform based DF array does not have ambiguity in DF in the proposed

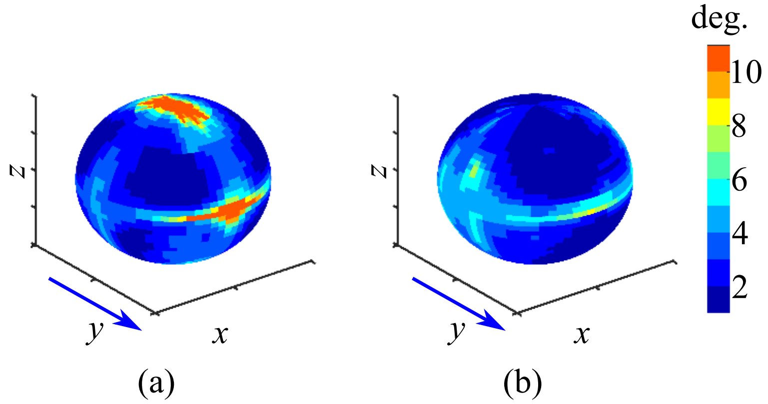

Figure 3.10: The average CRB patterns of (a) azimuth angle $\text{CRB}_{avg,\phi\phi}$ and (b) elevation angle $\text{CRB}_{avg,\theta\theta}$. Every point on the surface of the sphere corresponds to a direction of arrival with a given θ and ϕ value. Parameters of the calculation include: Available $SNR = 25$ dB and number of snapshots $K = 1$. The aircraft is heading towards $+\hat{y}$ direction (blue arrows).

FoV (4π Sr. solid angle); 2) This array can be used to estimate both the AoA and the polarization of the incoming wave; and 3) The AoA estimation root mean square errors are very close to the CRB values of the pure CM modes. These Monte Carlo tests were done with the following steps:

1. Generate signals with the measured radiation patterns at randomly selected angles (see (3.2)).
2. Add Gaussian white noises to these signals.
3. Feed the noisy signals to the MUSIC algorithm to estimate the AoA and the polarization (tilt angle in this specific case).
4. Repeat Steps 1 to 3 for N_{MC} times and calculate mean values and root mean square (RMS) errors.

In these tests, available SNR is 25 dB, the number of snapshots for each estimation (K) is 100, and the repeating time N_{MC} is 100.

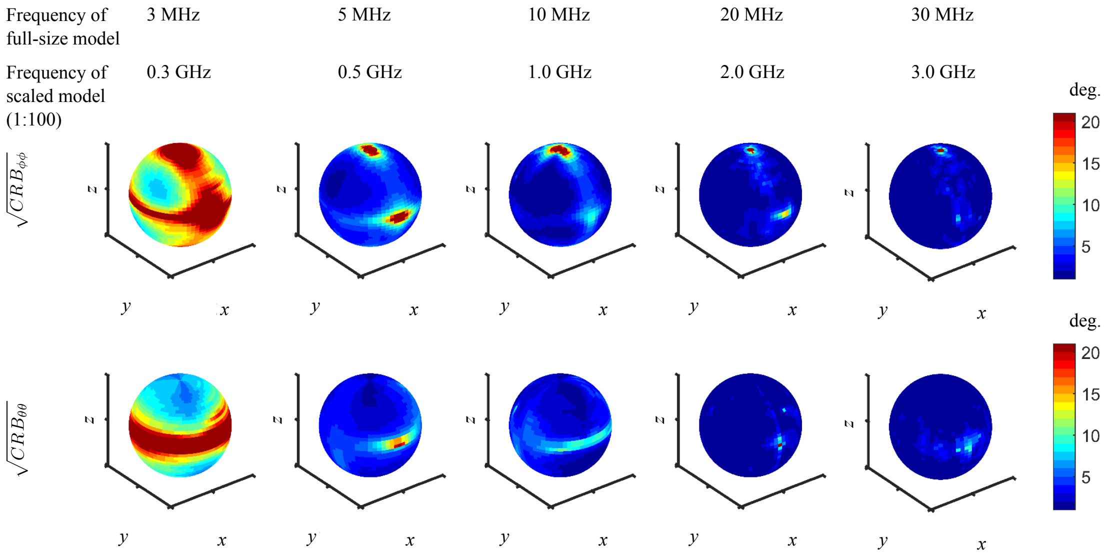

Figure 3.11: Simulated CRB patterns of the proposed DF antenna array at 3, 5, 10, 20 and 30 MHz, computed with simulated radiation patterns and averaged over tilt angle. The aircraft is heading towards $+\hat{y}$ (bottom-right) direction.

The improved MUSIC algorithm proposed by Ferrara and Parks (1983) was implemented and used to estimate AoAs and tilt angles. This algorithm is a generalization of the original MUSIC algorithm proposed by Schmidt (1986). The improved algorithm can estimate the AoA and the polarization of impinging waves using the data collected by antenna arrays composed of diversely polarized elements. Similarly, the improved algorithm is also computationally efficient. It can estimate both the AoA and the polarization by searching only along the AoA dimension (excluding the polarization dimension). More specifically, this algorithm estimates the AoA via searching, and then explicitly computes the polarization parameters with the estimated AoA. Therefore, the improved algorithm is especially suited for platform-based DF antenna arrays. This improved algorithm is able to detect multiple signals simultaneously, similar to the original MUSIC algorithm. However, this multiple signal detection capability is not investigated here.

Monte Carlo tests were performed at three randomly selected directions and

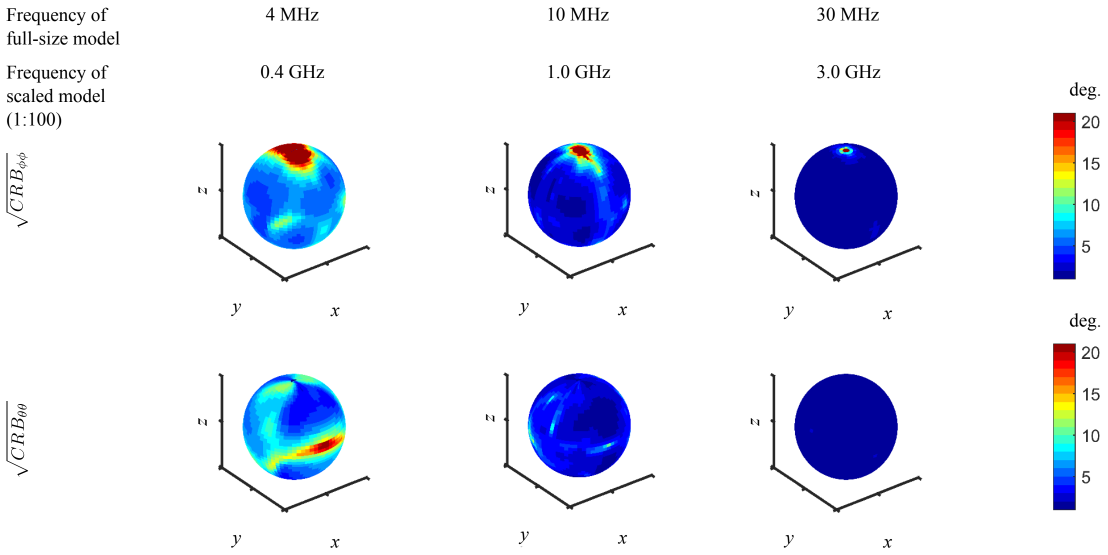

Figure 3.12: Measured CRB patterns of the fabricated scaled-model prototype of the proposed platform-based DF antenna array. The measurement are preformed at 425, 1000, 3000 MHz, corresponding to 4, 10, and 30 MHz in the full-scale model. These CRB results are averaged tilt angles (γ) of $0°, 30°, 60°$, and $90°$.

polarization states. The estimation results, as well as the corresponding CRB values are listed in Table 3.5. The mean values of the estimations are very close to the real values, showing the performance of this antenna array and that of the algorithm. The RMS errors also have a good agreement with the CRBs, indicating the efficacy of the proposed design procedure. The algorithm searched in the entire 4π Sr. solid angle, and no clue of ambiguity was observed.

The last row of Table 3.5 shows that the RMS error for this specific angle is somewhat larger than what is predicted by CRB. The reason is that, when implementing the algorithm, I used a 2° grid on even numbers to scan along θ and ϕ. As a result, an off-grid point (e.g., the one in the last row) will present larger estimation errors of a few tenths of a degree, depending on how far this point is away from the grid points. For example, in a one-dimensional estimation, using even grid points (i.e., $0°, 2°, 4°, \cdots$) a real incidence angle of 3° is estimated as either 2° or 4°. This quantization introduces an additional 1° RMS error. Whereas, if a real value is 2°, then there will be zero additional RMS error. Further, any real value between 2° and 3° will have some additional RMS error between 0° and 1°.

3.5 Characterization of the Platform-Based DF Array Over the Entire HF Band

In the previous section, I demonstrated both theoretically and experimentally the performance of a platform-based DF array optimized to operate at 10 MHz. In this section, I will investigate the performance of this platform-based DF array over the entire HF range. Simulations at different frequencies throughout the HF band were done with the MoM solver of FEKO 7.0. Then, CRB patterns were computed and are shown in Figure 3.11. In these simulations, it is assumed that the shapes and locations of the coupling elements are maintained. However, the impedance matching networks shown in Figure 3.6 are tuned to match the elements to the operating frequency. In HF systems, this task is usually accomplished by automatic impedance tuners. The patterns presented in Figure 3.11 are the θ and ϕ components of the average CRB (i.e. $\mathrm{CRB}_{avg,\theta\theta}$ and $\mathrm{CRB}_{avg,\phi\phi}$). These patterns were computed with available $SNR = 25$ dB and the number of snapshots $K = 1$. Observe that over most of the band and over the majority of the FoV, the CRB values are lower than 5°. The CRB values show differences for the different angles of incidence. The θ component of the CRB (i.e., $\mathrm{CRB}_{avg,\theta\theta}$) has a low-accuracy belt around $\theta = 90°$ at lower frequencies. The azimuth angle component (i.e., $\mathrm{CRB}_{avg,\phi\phi}$) has low-accuracy belts both around $\theta = 90°$ and $\phi = 90°$ and 270°. This implies that it is necessary to consider the FoV when I design DF antenna arrays. Different FoVs may have dramatically different CRBs, requiring different combination of CMs to approach the optimal design. Moreover, the CRB increases as frequency decreases as is naturally expected. Meanwhile, the shapes of the CRB patterns remain almost unchanged. The similar shapes imply that the actual CMs used for DF at these frequencies do not change significantly. At 10 MHz, the aircraft is about 1.4 wavelengths long and 1.1 wavelengths wide. At frequencies lower than

10 MHz, the electrical size is smaller. Thus, the CMs are not as efficiently excited as they are at higher frequencies. As a result, when the locations of coupling elements do not change, the excited CMs are not expected to significantly change over this frequency range. However, at higher frequencies, the horizontal stabilizers, which are 14 m long, become larger than half a wavelength. Then, more CMs are likely to be excited even with the same set of coupling elements. As a result, the shape of the CRB pattern gradually changes at higher frequencies. However, this does not deteriorate the accuracy of the system.

I also characterized the fabricated scaled-model prototype at 425 MHz and 3 GHz, corresponding to 4.25 MHz and 30 MHz for the full-scale platform. At each of these frequencies, I used a different set of matching networks, but used the same set of coupling elements. The fabricated prototype was not characterized at lower frequencies because the spherical near-field measurement systems used cannot operate below 408 MHz. Then, I computed CRB patterns with the measured radiation patterns, assuming that the available SNR is 25 dB and that the number of snapshots (K) is 1. The results are shown in Figure 3.12. As can be seen in Figure 3.12, CRB patterns computed with the measured radiation patterns have a good agreement with those computed with simulation results (shown in Figure 3.11). The CRB computed with the measurement results decreases as frequency increases. They also show very similar shapes to those computed with simulation results.

Finally, I compared the θ and ϕ components of the average CRBs computed with simulation and measurement results. These average CRBs are listed in Table 3.6. The CRB computed with simulation and measurement results show very good agreement. Besides, the listed $\sqrt{\mathrm{CRB}}$ is roughly inversely proportional to frequency. This lines up with the well-known conclusion that the $\sqrt{\mathrm{CRB}}$ of an uniform linear array is inversely proportional the array's length (Holder, 2014).

3.6 Conclusions

In this chapter I proposed a systematic method for designing platform-based direction finding (DF) antenna arrays. The proposed method is based on selecting

Table 3.6: Comparison of the Simulated CRB Values in the HF Band and the Measured CRB Values at the Corresponding Scaled Frequencies.

Freq. [MHz]	$\sqrt{\mathrm{CRB}_{avg,\theta\theta}}$ [deg.]		$\sqrt{\mathrm{CRB}_{avg,\phi\phi}}$ [deg.]		$\sqrt{\mathrm{CRB}_{AoA}}$ [deg.]	
	Sim.	Meas.	Sim.	Meas.	Sim.	Meas.
3	15.3	-	19.7	-	25.0	-
4	9.0	8.1	13.0	13.0	15.8	15.4
5	3.9	-	7.7	-	8.9	-
10	3.5	3.5	5.1	5.3	6.2	6.5
20	1.5	-	2.7	-	3.0	-
30	1.0	0.9	1.8	2.0	2.0	2.3

Available SNR $= 25$ dB, number of snapshots $K = 1$.

and exciting the subset of the platform's characteristic modes that provides the smallest CRB, or the lowest AoA estimation error. The mode selection procedure quantitatively considers the field of view and the polarization of the impinging waves in calculating the lowest AoA estimation error. To demonstrate the effectiveness of the proposed method, I designed and simulated a DF array designed to operate onboard a mid-size aircraft over the entire HF band. I also fabricated and measured a scaled-model prototype of this platform-based DF array, and used its measurement results to perform DF experiments in an emulated environment. The CRBs computed using the simulated and measured data were shown to agree very well with each other. Moreover, I performed Monte Carlo tests at randomly selected AoAs and polarization states. The results demonstrate that the AoA and polarization estimation errors of the proposed design can approach the lower bounds predicted by the CRB values of purely-excited characteristic modes of the platform.

An alternative approach of exploiting the platform's characteristic modes to achieve enhanced direction finding accuracy is to excite a set of different combinations of the CMs, rather than pure CMs. This approach requires having properly-designed, platform-based antennas that can accurately excite a given combination of CMs with appropriate complex weights. Each combination of this finite set can be used as an element of a platform-based DF array. In theory, a finite set of such combinations (e.g., one that includes 4 different combinations involving more than four pure CMs of the platform) may have a better DF performance compared to a similarly-sized, finite set of pure CMs of the platform. Examining the advantages of such a system over the ones presented here and investigating its implementation complexities are worthwhile research questions to address.

Selecting four modes out of six significant modes (named as Modes 1 to 6) results in 15 combinations. Each of these combinations (named as Combination 1 to 15) contains four modes which are given in Table 3.7.

Table 3.7: Characteristic modes contained in each mode combination shown in Figure 3.4.

Combination	Modes			
1	1	2	3	4
2	1	2	3	5
3	1	2	3	6
4	1	2	4	5
5	1	2	4	6
6	1	2	5	6
7	1	3	4	5
8	1	3	4	6
9	1	3	5	6
10	1	4	5	6
11	2	3	4	5
12	2	3	4	6
13	2	3	5	5
14	2	4	5	6
15	3	4	5	6

4 A SPATIALLY-CONFINED, PLATFORM-BASED HF DIRECTION FINDING ARRAY

4.1 Introduction

The high-frequency (HF) band is widely used in a variety of civil and military applications, including near-vertical incident skywave (NVIS) and maritime communications, over-the-horizon radar, and surveillance and navigation among others. Using HF frequencies is of particular interest in military communications applications due to their long range and beyond line of sight propagation characteristics. As a result, direction of arrival (DoA) estimation at HF frequencies is of particular interest in electronic warfare support applications. Performing accurate direction finding at the HF band is rather challenging due to the very long wavelengths of electromagnetic waves that range from 100 m at 3 MHz to 10 m at 30 MHz. Accurate direction finding (DF) at such frequencies requires the use of antenna arrays with relatively large individual elements and large spacing between them. However, in many applications HF DF systems need to be mobile and capable of being mounted on ground-based or airborne platforms that have limited available area to accommodate them. Such limitations restrict the sizes of the antennas and the overall aperture dimensions of mobile HF DF systems. This will in turn limit the DoA estimation accuracy of such systems. Furthermore, the presence of the supporting platform can significantly impact the performance of the HF DF system.

In the past decades, numerous papers have been published on the physical limitations on the performances of electrically-small antennas (Chu, 1948; Gustafsson et al., 2007; Hansen, 1981; Collin and Rothschild, 1964) and designs that approach these bounds (Sievenpiper et al., 2011; Noguchi et al., 2003; Best, 2005; Stuart and Best, 2008; Hong and Sarabandi, 2009; Erentok and Ziolkowski, 2008; Lee et al., 2002). Using similar method of spherical mode expansion, the limitation on DoA estimation accuracy of antenna arrays with electrically-small apertures has also been investigated by Nordebo et al. (2006), as well as a number of attempts to implementing small-aperture DoA array. Slater et al. (2013) investigated the DF capability of a small-aperture DF array composed of closely-placed small loops. Our group recently proposed compact antenna arrays that not only approach the bandwidth limit but also exhibit DF capabilities of determining both the elevation and azimuth angles of arrival (Ghaemi et al., 2018; Ma and Behdad, 2020). However, the DF accuracy of these antennas drops drastically as frequency is reduced such that the maximum linear dimension of the aperture become smaller than $\lambda_0/20$, where λ_0 is the free-space wavelength. Furthermore, as shown by Nordebo et al. (2006), electrically-small antenna arrays have an upper bound of DF accuracy set by the electrical dimensions of the aperture. One way to surpass this bound is by exploiting the platform on which the antenna is mounted and use it as part of the DF aperture. Corbin (2011) and Archer (2013) investigated development of platform-based HF DF systems that use monopole antennas and B-dot sensors distributed over a mid-sized airplane. Manteuffel and Martens (2016) excited multiple characteristic modes (CMs) of a single radiator and used them for DF purposes. This approach, however, requires significant changes to be made to the radiator itself, limiting its application to very few platforms allowing such significant structural modifications. This approach employed the CM theory that has been well established by Harrington and Mautz (1971) and Chen and Wang (2015a). By exploiting the same theory, I recently reported the design of platform-based HF antennas and demonstrated that by employing the CMs of the platform as the elements of a DF array, significant improvements on the accuracy of platform-based HF DF systems can be achieved (Ma and Behdad, 2018b). To efficiently excite the CM of the platform, electrically-small coupling elements distributed over the platform were used (Ma and Behdad, 2018b). The mounting location of each coupling element was chosen to efficiently excite the desired CM of the platform. As a result, the elements of the HF DF system reported by Ma and Behdad (2018b) were distributed over a large area of the platform. Distributing the elements of a platform-based DF array, however, may not be possible in many practical applications where only a limited area may be available to accommodate the antenna elements of a DF system.

In this chapter, I report a spatially-confined, platform-based antenna array designed with the aid of the characteristic mode theory. This array was designed having two primary objectives in mind. First, the maximum linear dimension of the array was fixed at 3 m, which corresponds to $0.1\lambda_0$ at 10 MHz. Secondly, despite its spatially-confined nature, the array was designed to excite multiple CMs of the platform to achieve enhanced bandwidth and DF accuracy as pointed out by Ma and Behdad (2018b). In other words, the primary goal of this design was to achieve most of the performance gains obtained by a design similar to that reported by Ma and Behdad (2018b) with a spatially-confined, platform-based DF array with a maximum linear dimension of 3 m. I used a simplified model of a mid-size passenger airplane as a representative platform and developed four antenna arrays for different promising mounting locations on the platform. The bandwidth and DF accuracy of these designs were compared with the theoretical bounds of a standalone optimum array possessing the same volume as discussed by Nordebo et al. (2006). The simulation results demonstrated that the Cramer-Rao bound (the lower bounds of DoA estimation) of the proposed platform-based arrays can surpass the theoretical limit of the Cramer-Rao bound (CRB) of any standalone array possessing the same volume. Then, I fabricated and measured a scaled model of one of the proposed designs with the broadest bandwidth and lowest CRB value. Measurement results agree well with the simulations and demonstrate that the proposed array can achieve DF accuracy 15% better than the theoretical limit while having a significantly enhanced bandwidth compared to what is achievable from the same array when the platform is not exploited.

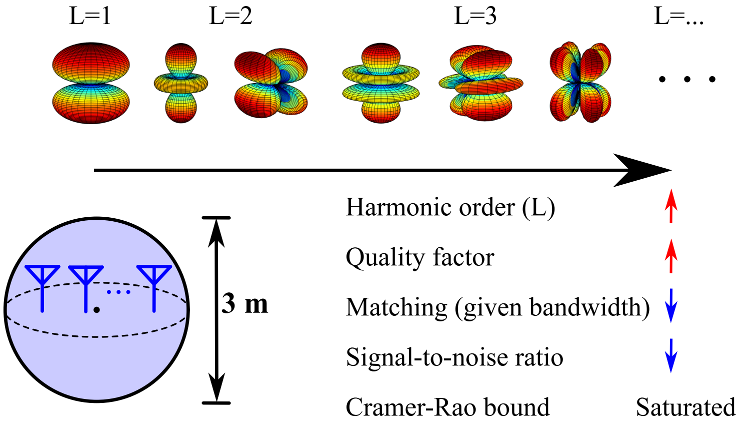

Figure 4.1: The direction finding accuracy of an antenna array circumscribed in a sphere with a fixed radius has a physical limit. The limit is approached by accounting for the contributions to the DF accuracy of all spherical harmonics of the sphere excited by an optimum array. As the higher-order harmonics have very large quality factors or poor matching over a given bandwidth, they contribute little to improving the DF accuracy.

4.2 Design Procedure and Comparison with the Theoretic Limits

Theoretical limits of the DF accuracy of a spherical aperture with a 3 m diameter

The lower bound of the DoA estimation error of an arbitrary antenna array occupying a spherical aperture and located in free space was derived by Nordebo et al. (2006). In this analysis, the radiation patterns of the array enclosed in a virtual sphere were expressed as a superposition of an infinite number of spherical harmonics. The lower bound of the DoA estimation error of such an idealized system is then obtained by assuming that all these spherical harmonics can be measured without loss. In practice this lower bound of electrically-small arrays can be calculated by accounting for a finite number of these harmonics. The convergence of the calculation can be intuitively interpreted as follows. On the one hand, as shown in Figure 4.1, the higher the order of the spherical harmonic is, the more rapidly its radiation pattern changes as a function of angle. Therefore, including higher-order harmonics can increase DF accuracy. On the other hand, however, the quality factor of the harmonics increase drastically as the order of the harmonic increases (Collin and Rothschild, 1964). As a result, based on Fano's theory (Fano, 1950), higher-order harmonics have poorer impedance matching over a given bandwidth. Specifically, the transmission of the L^{th} order harmonics is expressed as:

$$|t_L| \leqslant \sqrt{1 - e^{-\frac{-2\pi}{Q_L}\frac{1-B^2/4}{B}}} \tag{4.1}$$

where Q_L is the Q-factor of the L^{th} order harmonics and B is the bandwidth. In other words, the large Q-factor of a higher-order harmonic causes them to be received with a reduced efficiency due to the significant mismatch loss that occurs over a given, fixed bandwidth. This in turn reduces the signal-to-noise ratio of these modes. Therefore, the higher the order of the mode is, the smaller its contribution to the DoA estimation will be. This results in the convergence of the calculation of the lower bound error.

For example, for any antenna array that is circumscribed by a virtual sphere of 3 m diameter, the averaged CRB is calculated following this process and the results are presented in Table 4.1. In this analysis, I have assumed that 6, 16, and 30 vector spherical harmonics are used to perform DoA estimation at 3, 10 and 30 MHz. Recalling that the vector spherical harmonics with the same order have three orientations and two polarizations, the number of harmonics with order of 1, 2 and 3 is 6, 10 and 14, respectively. In our analysis, the 6, 16 and 30 vector spherical harmonics are all the harmonics with the order up to 1, 2 and 3, respectively. In the calculation, the number of time samples of the signal used to perform DF (i.e., snapshots) is assumed to be 1, and available signal-to-noise ratio (SNR) is 25 dB. The available SNR is defined as the SNR after analog-to-digital converter when the antenna gain is 0 dBi. The system bandwidth is assumed to be 3%. As can be seen, at a given frequency, as the number of vector spherical harmonics used to perform

Table 4.1: Cramer-Rao bound (CRB) of array confined by a virtual sphere of 3m diameter in HF band

Frequency	Fractional bandwidth	$\sqrt{\text{CRB}}$ limit Different number of harmonics 6	 16	 30
3 MHz	3%	57.1°	57.0°	57.0°
10 MHz	3%	14.2°	14.0°	14.0°
30 MHz	3%	13.0°	6.19°	6.07°

Available SNR is 25 dB, number of snapshots is 1.

DoA estimation increases, the averaged CRB value decreases and converges to its final value. This verifies the preceding qualitative analysis. Additionally, given the sphere's fixed physical dimensions, the final converged CRB value is smaller at higher frequencies, indicating a lower DoA estimation error bound. This results from larger electrical dimension and better impedance matching of the higher-order modes that occur when the aperture's electrical dimension increases.

Design procedure

In designing the proposed spatially-confined DF array, I followed two primary design objectives. First, the entire DF array must be spatially confined and have a maximum linear dimension less than 3 m. Secondly, the array must be capable of efficiently exciting multiple characteristic modes of the platform. To accomplish these goals, I used the theory of characteristic modes as a tool in the design process. Characteristic modes of a platform constitute an orthogonal set of surface current distributions, and any excited current can be expressed as a superposition of the all the CMs. Specifically, the location of the spatially-confined array is first determined by selecting the locations where multiple significant characteristic modes have strong surfaces current or high charge densities. A significant mode is defined as one having a modal significance value larger than 0.7 (Harrington and Mautz, 1971). Significant modes are the primary contributors to the total radiation or DF accuracy of a platform-based antenna employing electrically-small coupling

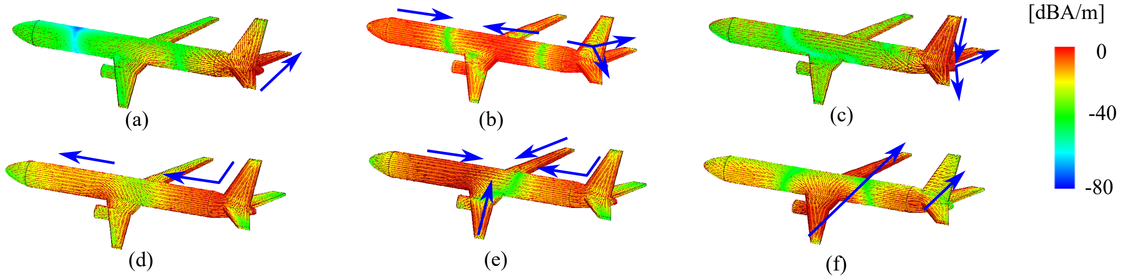

Figure 4.2: Surface current distribution of the significant characteristic modes of a mid-sized passenger airplane at 10 MHz. The blue arrows highlight the directions of the current flow. (a)-(f) corresponds to the first six most-significant characteristic modes.

elements. The radiation patterns of a platform-based antenna can be approximated by a superposition of the significant characteristic modes of the platform with reasonable accuracy (Chen and Wang, 2015a). Therefore, as the first step of the design process, the locations in which multiple significant CMs of the platform may be excited must be identified. Subsequently, the antenna elements of the array are designed to effectively excite these CMs. Two types of antennas (or coupling elements) are generally used for exciting CMs of the platform. These include capacitive coupling elements (CCE) and inductive coupling elements (ICE) (Martens et al., 2011). A CCE is a small monopole and usually placed at locations where the CM intended to be excited has a large charge density or weak surface current density. An ICE is often in the form of a small half loop and is usually placed at locations where the CM intended to be excited has a strong surface current density or magnetic field.

In our specific example of a simplified mid-size aircraft, I first performed characteristic mode analysis with Altair FEKO, a commercial electromagnetic simulation software. The analysis results indicated the existence of six significant modes at 10 MHz. The normalized current distributions of these modes (Modes 1 to 6) are depicted in Figures 4.2(a)–4.2(f) respectively, where the color on the airplane surface shows the current density and the blue arrows highlight the primary current flows and their directions. Modes 1 and 3 are respectively horizontal and vertical dipole modes on the airplane tail. Modes 2 and 4 are dipole modes along the airplane body. Mode 5 is a combined dipole mode on the airplane body and the wings. Mode 6 is a combination of dipole modes on the airplane wings and the horizontal stablizers. Notice that Modes 2, 4, 5 and 6 have relatively strong current densities at the intersection of the wings and body. Therefore, this part of the undercarriage of the airplane (shown in Figures 4.3(a) and 4.3(b)) is a candidate location for placing the DF array. In addition to this location, the significant modes have either strong current or strong charge densities along the vertical stabilizer, making this location another suitable candidate location to mount the DF array. After determining these two locations, in the next step, I investigated two specific coupling element designs that can excite the CMs of the platform around each location. These designs are shown in Figure 4.3. The designs were specifically placed near the front and rear edges of the wings and the horizontal stabilizers underneath the aircraft where the current densities of the platform's CMs are stronger than the nearby locations. The stronger current densities make it easier for the couping elements to excite the platform's CMs. All these arrays are composed of four coupling elements, which can be enclosed in a virtural sphere with a diameter of 3 m. The arrays shown in Figure 4.3(a)–4.3(c) are composed of four half loops (or ICEs) placed at locations where Modes 1–6 have strong current densities flowing along the edges of the wings and horizontal stablizers and/or along the body. The width and diameter of these half loops are respectively 0.4 m and 1.4 m. The ICEs 1 and 2 in both Designs A and B are employed to excite Modes 5 and 6, which have strong surface current densities flowing along the wings. Similarly, the ICEs 3 and 4 in Designs A–C are used to excite Modes 2, 4 and 5, and the ICEs 1 and 2 in Design D are used to excite Modes 1, 2, and 3. The design shown in Figure 4.3(d) is composed of three half loops (or ICEs) and one top-loaded monopole (or CCE). The CCE is for coupling to Mode 2, where it has weak current density (and strong charge density).

As an example, let us look closer at the design shown in Figure 4.3(d). The dimensions of this design as well as the locations of the feeds used to excite each element are shown in Figure 4.4. The structure was simulated in FEKO and the nor-

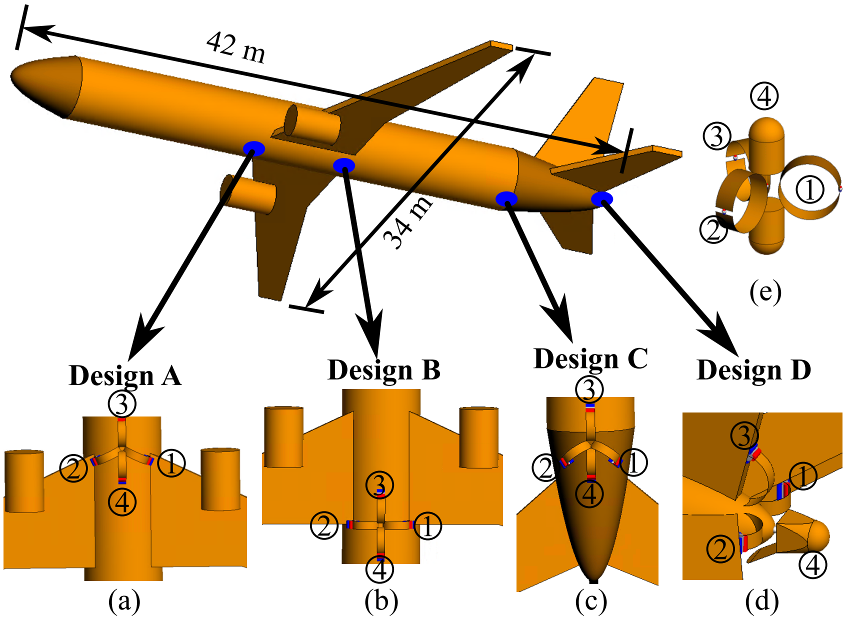

Figure 4.3: Platform-based, spatially-confined DF arrays placed at different locations on the platform. (a)–(b) Either DF array is composed of four half loops placed in the midsection of the aircraft. (c) The DF array is composed of four half loops placed near the tail of the airplane. (d) The DF array is composed of three half loops and one monopole placed on the aircraft's rear end. (e) The standalone version of the DF array shown in part (d). The array consists of the elements used in part (d) along with their mirror images. The numbers in the circles indicate the numbers of the specific coupling elements.

malized modal weighting coefficients (MWCs) of the different CMs were obtained when each of the coupling elements are excited (see Figure 4.5(d)). The normalized MWCs show the relative excitation coefficients of each CM when a given coupling element is excited. The results shown in Figure 4.5(d)) demonstrate that Modes 1, 2, 3, and 5 are primarily excited by these four coupling elements. Similar conclusion can be obtained by analyzing the normalized weighting coefficients of the other three designs as depicted in Figures 4.5(a)–4.5(c).

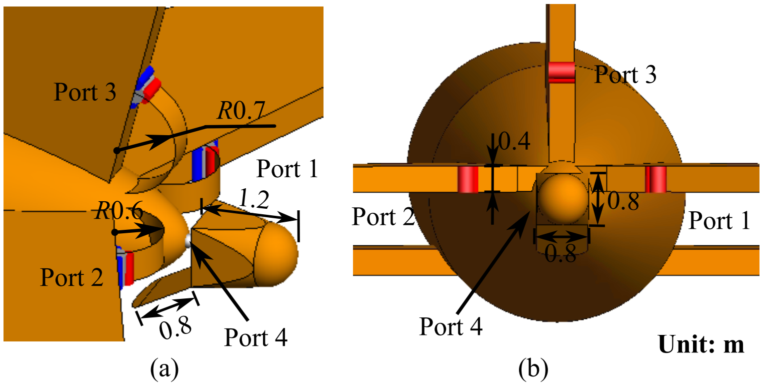

Figure 4.4: (a) Perspective and (b) rear view of the spatially-confined antenna array placed in the rear end of the aircraft. Dimensions of the elements are marked in meters.

Comparison of DF accuracy

To evaluate the DF accuracy of the proposed platform-based, compact antenna arrays, I compare their Cramer-Rao bound (CRB) with each other and with the theoretical limits of CRBs of standalone arrays possessing the same volume (as discussed in Section 4.2), as well as our previously published design composed of distributed coupling elements on the same aircraft (Ma and Behdad, 2018b). Table 4.2 compares the averaged CRB values of the platform-based DF arrays shown in Figure 4.3(a)-4.3(d), the standalone array shown in Figure 4.3(e), the distributed platform-based DF array presented by Ma and Behdad (2018b), and the theoretical limit on the lower bound of the CRB of any standalone array with a maximum linear dimension of 3 m. The standalone array shown in Figure 4.3(e) is similar to a standalone version of the array used in Design D (plus its mirror image) without the presence of the platform. It has the same maximum linear dimension of 3 m as do all the spatially-confined arrays in Designs A-D. The only line item in Table II that does not have the 3-m size limitation, is the distributed array reported by Ma and Behdad (2018b). This is provided here to simplify the comparison of the performance of the present work with that of our prior work. The averaged CRB was calculated following the approach reported byWeiss and Friedlander

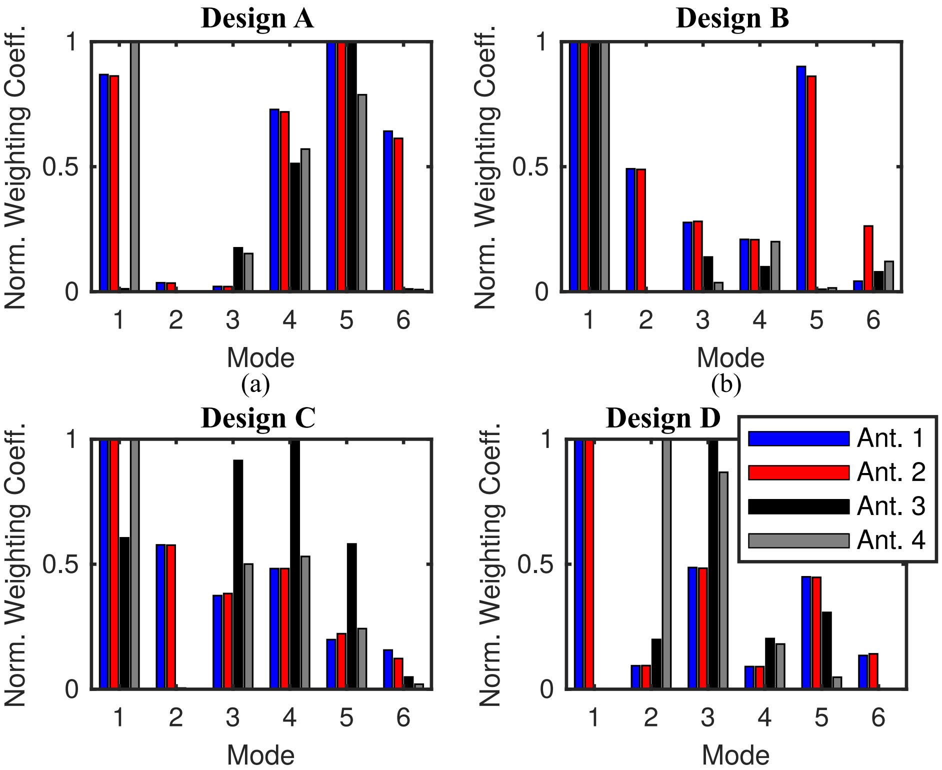

(a) (b) (c) (d)

Figure 4.5: Simulated nomalized modal weighting coefficients of all the significant CMs of the platform excited by DF array Designs A–D shown in Figure 4.3. (a)–(d) demonstrate the results of Designs A–D, respectively.

(1991) and Ma and Behdad (2018b). Specifically, for each design, I first calculated the realized-gain patterns (both magnitude and phase) of the antenna elements using FEKO. Then, based on the radiation patterns, I calculated the CRB at each direction (every 2° of the 4π steradian), assuming 0.25 ms of sampling time and 25 dB of available SNR. In the calculation, the number of snapshots is determined following $K = BT$ where B and T are respectively antenna bandwidth and sampling time. For example, $T = 0.25$ ms and 4% bandwidth at 10 MHz, the number of snapshots is 100. This is a reasonable choice in many practical applications. Finally, I averaged these CRB values over the entire sphere and listed the square root of the averaged values in Table 4.2. Note that the platform-based designs achieved

Table 4.2: Comparison of the DF performance of Designs A-D with theoretical limitations and other relevant DF arrays of interest.

Design	-10 dB bandwidth	Avg. $\sqrt{\text{CRB}}$	No. of antennas	Max. linear dimensions $[\text{m}]$
A	1.2%	1.74°	4	3.0
B	1.7%	1.35°	4	3.0
C	0.7%	3.08°	4	3.0
D	4.0%	1.30°	4	3.0
S.A. Array	0.16%	19.1°	4	3.0
Ma and Behdad (2018b)	3.0%	0.59°	4	24.3
Theo. limit	4.0%	1.51°	$\geqslant 16$	3.0

The available SNR is 25 dB, the sampling time is 0.25 ms and the operating frequency is 10 MHz.

lower CRB (or better DF accuracy) and wider bandwidth than does the standalone antenna array. Also, the platform-based arrays can achieve better DF accuracy with fewer number of antennas than any standalone antenna array possessing the same volume and having the same bandwidth. Furthermore, the platform-based array with distributed antennas proposed by Ma and Behdad (2018b) has better DF accuracy than the spatially-confined arrays. This is because distributing the elements over the platform allows for selecting the optimum location for coupling to each characteristic mode without any constraints. This, however, comes at the expense distributing the elements of the array over a significantly larger area (e.g., maximum linear dimension of 3 m in the present work vs. 24.3 m in our previous work (Ma and Behdad, 2018b)). As observed from Table II, among the spatially-confined designs, Design D can achieve better DF accuracy and a wider bandwidth than the others.

4.3 Scaled Model Fabrication and Experimental Characterization

Scaled model fabrication

I fabricated and measured a 1:100 scaled version of Design D, which is the design with the lowest CRB and the broadest bandwidth. The scaling factor of 1:100 was chosen based on the frequency of operation and the maximum dimensions of the antenna under test that our near-field spherical measurement system can support. Specifically, our near-field system can perform measurements in the 600 MHz – 18 GHz frequency range and can accommodate antennas that can be enclosed by a virtual sphere with the diameter up to 45 cm. Based on this, a scaling factor of 1:100 results in a prototype dimension of 42 cm × 37 cm that is near the maximum size our system can accommodate. This also scales the operating frequency of 10 MHz to a scaled frequency of 1 GHz, making the scaled frequency fall within the range of measurement of our near-field system.

The airplane model and the CCE of the array were first 3-D printed in plastic material and then covered with copper tape. The ICEs of the array were made by bending thin copper strips into shape. The coupling elements were connected to matching circuits located immediately at the feed terminals and matched to 50 Ω. These matching circuits are regular L-shaped, lumped-element matching networks implemented on 1 cm × 1 cm printed circuit boards (PCBs), which were placed inside the airplane model right next to the coupling elements. Photos of the fabricated prototype and matching circuits are shown in Figure 4.6.

S-parameter measurement

The S-parameters of this prototype array were measured by using a four-port vector network analyzer (Agilent N5225A), where the Ports 1-4 were connected respectively to the coupling elements 1 to 4. The measured results are shown in Figure 4.7. In this figure, the solid curves show the reflection coefficients and the

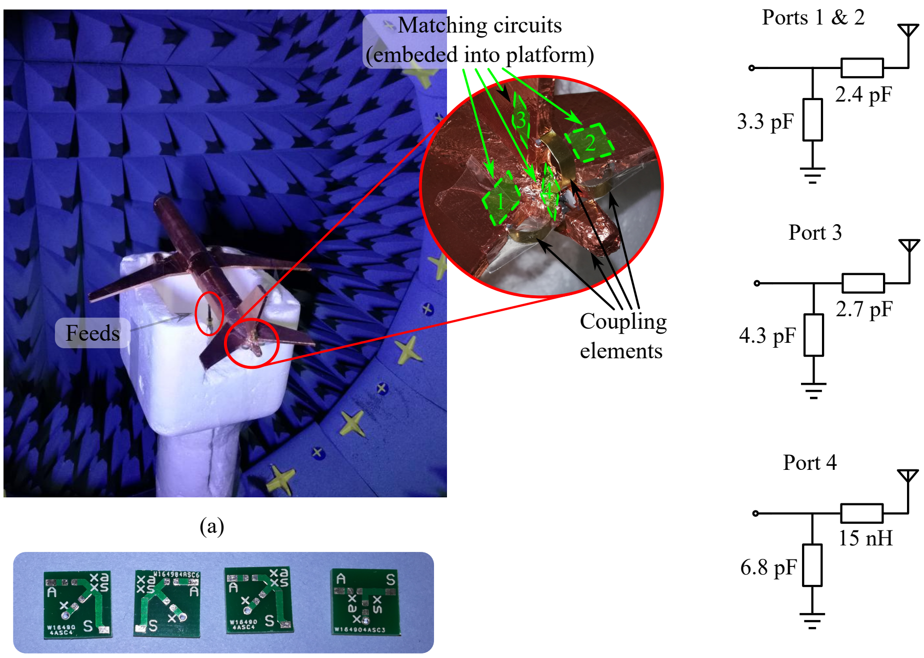

(a)

(b)

(c)

Figure 4.6: Photograph of (a) the fabricated prototype of Design D placed in a near-field anechoic chamber, Satimo StarLab Version E, and (b) the impedance matching circuits placed next to the coupling elements. The topology and component values of the matching circuits used in the measurement are illustrated in (c).

dashed curves show the mutual coupling. The S_{23} and S_{24} curves are very similar to S_{13} and S_{14}, respectively, because of symmetry and are omitted for brevity. Note that the overlapped frequency range where all array elements' reflection coefficients are below -10 dB (defined as the -10 dB bandwidth of the antenna array) is 5.4% (or 54 MHz centered at about 1 GHz) as compared to the simulation result of 4.0%. This slightly wider bandwidth is attributed to the loss of the matching networks, which were assumed to be lossless in the simulations. The measured maximum realized gains of the antennas are 1.7–2.0 dB lower than the simulation results assuming lossless matching network. When the loss of the matching networks and those of the cables used between the antenna feed points and the calibration reference plane of the measurements are taken to account, this difference between the measurement

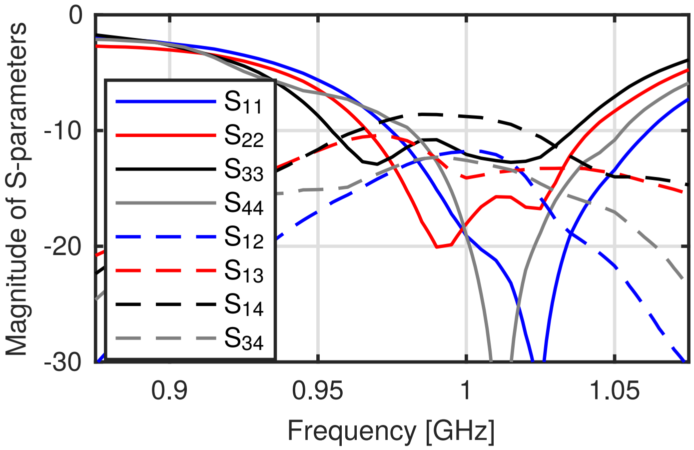

Figure 4.7: The measured S-parameters of the scaled-model version of the platform-based DF array (Design D). The port numbers are defined in Figure 4.4.

and simulation realized gains reduces to 1.0-1.4 dB. The remaining difference is likely due to the tolerances of the lumped element components used in the matching network as well as the losses of the printed circuit board on which the matching networks are fabricated, which were not taken into account in the simulations. Over the operating frequency band, the mutual coupling between Ports 1 and 4 (or the elements on the horizontal stablizer and the tail end) is below -8.6 dB, and those between other ports are below -12 dB. The mutual coupling is primarily a result of the small aperture size and the shared CMs excited by different array elements (as shown in Figure 4.5). This relatively low level of mutual coupling is good for DF accuracy since it reduces the radiation efficiency degradation and improves the diversity of the array elements' radiation patterns.

Radiation pattern measurements and CRB calculation

The radiation pattern and efficiency of the fabricated prototype were measured by using a spherical near-field measurement system (Satimo StarLab Version E). The measurement setup is shown in Figure 4.6(a). In this setup, I first connected one of the antenna ports to the feed of the Satimo StarLab and terminated the rest of the ports to 50 Ω loads. Then, I recorded both the magnitude and phase of the θ and ϕ components of the realized gain. The phase is defined as the phase of the electric fields in the farfield. Both phase and magnitude of the gain are important in the direction-finding process as they both will be used in determining the direction of arrival and the CRB value of the DF system. Next, I repeated this for each port of the antenna array. The magnitudes of the measured realized-gain radiation patterns are plotted in Figures 4.8(e)–4.8(h). For comparison, the simulated radiation patterns are plotted in Figures 4.8(a)–4.8(d). Observe that the measured and simulated radiation patterns are rather similar to each other. The differences observed between them are attributed to the presence of the coaxial cables and connectors used to feed the antenna, which protrude from the undercarriage of the scaled-model aircraft prototype. These cables and connectors are not included in the simulations. The measured maximum realized gain is 1.0-1.4 dB lower than the simulation after taking into account the loss of the matching circuits, the coaxial cables connecting the matching circuits and the feed ports, and the SMA connectors in simulation. This difference can be attributed to the difference of the shapes of the measurement and simulation patterns and the tolerance of components and materials. Note that the shape of the measured pattern of Port 4 is slightly different from that of the simulated one while the shapes of the measured patterns of the rest ports agree well with that of the simulated ones. This difference is attributed to the presence of the coaxial cable protruding from the undercarriage of the airplane model. Specifically, as shown in Figure 4.5(d), Port 4 excites a significant amount of Mode 2 that has strong currents following along the undercarriage area of the airplane model. On the other hand, Ports 1–3 strongly excite Modes 1, 3 and 5 that have very week current following along the undercarriage area. As a result, the perturbation introduced by the coaxial cables protruding the carriage area is relatively strong to Port 4 but not for Ports 1–3.

The measured total efficiency is between 36% to 48%. The factors that impact the radiation efficiency and contribute to its reduction include the material loss of copper and the losses of the matching circuits and coaxial cables. Another factor that impacts the efficiency is the power coupled to the other ports of the array and

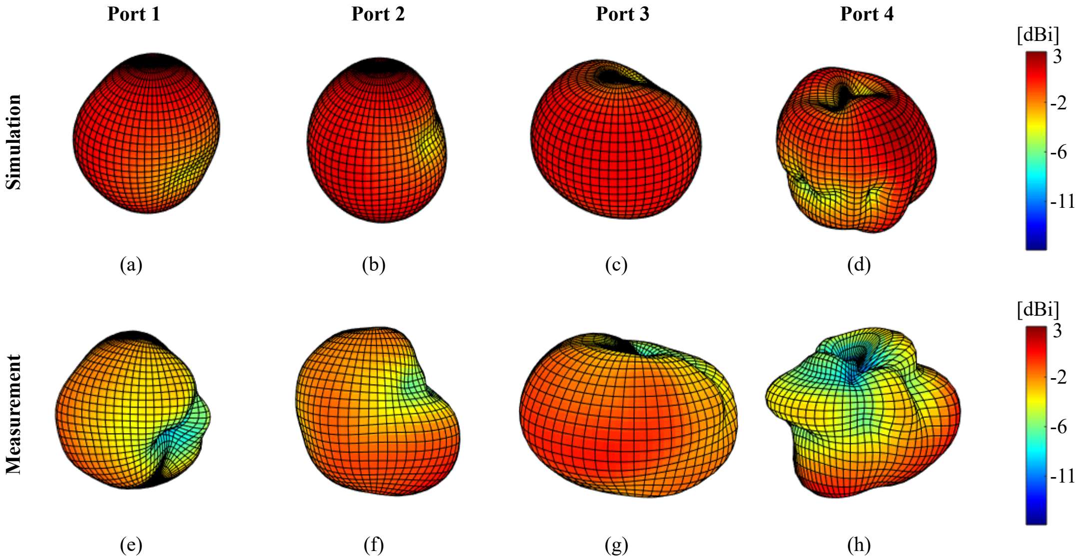

Figure 4.8: (a)-(d) Simulated and (e)-(h) measured realized gain radiation patterns of the fabricated prototype at 1 GHz.

dissipated in the termination loads due to mutual coupling.

Using the measured and simulated realized gain patterns, I calculated the CRB for estimating both elevation and azimuth angles of arrival in the full sphere. I assumed 25 dB of available SNR and 0.25 ms of sampling time (or 100 samples per estimation). The CRB results are plotted in Figure 4.9. Note that along most of the directions, the CBR value is below 1°, indicating a very good direction finding accuracy provided by the proposed design. Furthermore, the CRB patterns in simulations and measurements look very similar to each other. They all have relatively high CRB values (depicted in red color) in the front, top and bottom directions of the aircraft. This is because that the proposed array has relatively low gain towards these directions.

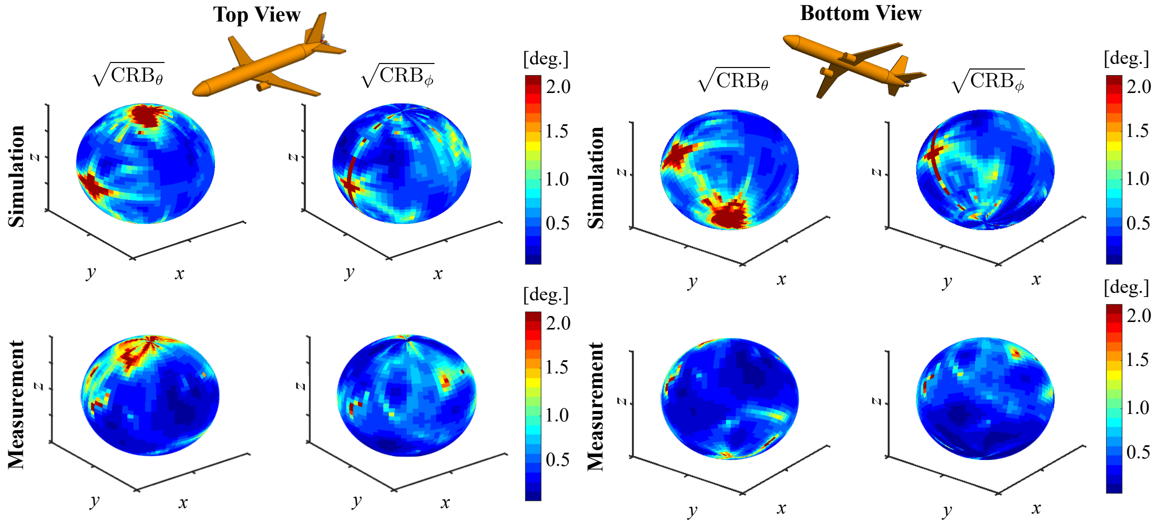

(a) (b)

Figure 4.9: (a) Top and (b) bottom view of Cramer-Rao bound (CRB) patterns of elevation (θ) and azimuth (ϕ) angle of arrival estimation errors calculated with simulated and measured radiation patterns. The simulations and measurements were conducted at 10 MHz and 1 GHz respectively. The available SNR is 25 dB. The sampling time is 0.25 ms and the antenna bandwidth is 400 kHz or 4% at 10 MHz for the simulations, and 2.5¯s and 40 MHz at 1 GHz for the measurements.

Direction-of-arrival estimation

To demonstrate the DF capability of the proposed design, I conducted Monte-Carlo tests at multiple, randomly-selected direction-of-arrivals for different polarizations of the incident waves. In each test, I assumed a single incident wave. The specific steps of the Monte-Carlo test are as follows:

1. Select a direction-of-arrival (DoA) and polarization of the incident wave.
2. Determine the signals received by the antennas using the measured complex gain patterns of the antennas discussed in Section 4.3 and add noise to the received signals.
3. Perform DoA and polarization estimation using the multiple signal classification (MUSIC) algorithm.

4. Repeat Steps 2 and 3 for 100 times and record the estimation results.

In Step 2, the signals and noise are generated following (4.2).

$$\mathbf{X}(t) = \mathbf{A}_\theta(\theta_i, \phi_i)E_\theta(t) + \mathbf{A}_\phi(\theta_i, \phi_i)E_\phi(t) + \mathbf{n}(t) \tag{4.2}$$

where $\mathbf{X}(t) = [x_1(t), x_2(t), x_3(t), x_4(t)]^T$ is the vector of the voltages measured at the receivers connected to the four antenna elements at time $t = 1, 2, \cdots, T$; $\mathbf{A}_\theta(\theta_i, \phi_i)$ and $\mathbf{A}_\phi(\theta_i, \phi_i)$ (4×1 vectors) denote the elevation (θ) and azimuth (ϕ) components of the measured complex realized-gain patterns at the DoA (θ_i, ϕ_i) of the incident wave. Here I assumed a single incident wave in each test. $E_\theta(t)$ and $E_\phi(t)$ denote the θ and ϕ components of the incident wave. $E_\theta(t)$ and $E_\phi(t)$ describe the polarization (denoted by γ) of the incident wave following $E_\theta/E_\phi = \cos(\gamma)$. $\mathbf{n}(t)$ (four-dimensional vector) is assumed to be Gaussian white noise with variance matrix of $\sigma^2\mathbf{I}$ ($\mathbf{I}$ is identity matrix) and σ^2 is the noise power. Here, I assumed unit signal power (i.e., $E_\theta^2 + E_\phi^2 = 1$), and that the noise power is $\sigma^2 = 1/\text{SNR}$. The SNR is defined as the signal-to-noise ratio at the receiver given antenna realized gain of 0 dBi, and was selected as 25 dB. Finally, the sampling time T was selected as 0.25 ms, resulting in the number of snapshots of $K = BT = 100$ where $B = 400$ kHz (i.e., 4% at 10 MHz) is the array's bandwidth. The selected T and K values are reasonable in practical applications and give small estimation errors. To conclude, I emulated the noisy received signal at a randomly-selected DoA and polarization, with the measured radiation patterns and properly assumed SNR and sampling time.

In Step 3, I used a specialized version of MUSIC algorithm (Ferrara and Parks, 1983) that is computationally efficient and suitable for antenna arrays with diversely-polarized antenna elements. The MUSIC algorithm was proposed by Schmidt (1986). It is a well-known super-resolution algorithm that can achieve DoA estimation accuracy better than diffraction limit at high SNR and its accuracy can approach the theoretical bounds predicted by CRB with large number of snapshots (Weiss and Friedlander, 1991). The specialized version of MUSIC algorithm reported by Ferrara and Parks (1983) estimates the DoA under unknown polarization of the incident waves with searching only in the elevation and azimuth angles. This

Table 4.3: Monte-Carlo tests results at three randomly selected directions of arrival and polarizations of incident waves. $\sqrt{\text{CRB}}$ at corresponding DoA and root-mean-square errors of the Monte-Carlo tests are also listed for comparison.

Frequency	Test	Real DoA and pol.			$\sqrt{\text{CRB}}$			Est. DoA and pol.			RMS error		
		θ	ϕ	γ	θ	ϕ	γ	θ	ϕ	γ	θ	ϕ	γ
425 MHz	#1	**70°**	**44°**	**60°**	1.27°	1.42°	1.56°	**69.80°**	**45.24°**	**59.50°**	5.09°	6.25°	2.54°
	#2	**120°**	**100°**	**0°**	2.26°	9.28°	20.4°	**119.62°**	**95.51°**	**8.12°**	10.60°	14.51°	20.36°
	#3	**30°**	**260°**	**30°**	1.15°	5.31°	6.02°	**42.36°**	**219.1°**	**48.35°**	20.98 °	75.90°	24.36°
1 GHz	#4	**70°**	**44°**	**60°**	0.17°	0.09°	0.19°	**69.76°**	**43.76°**	**59.73°**	1.0°	0.75°	1.35°
	#5	**120°**	**100°**	**0°**	0.15°	0.90°	0.11°	**119.4°**	**99.60°**	**0.78°**	1.17°	3.78°	0.55°
	#6	**30°**	**260°**	**30°**	0.05°	0.10°	0.50°	**30.06°**	**259.9°**	**29.80°**	0.24°	0.62°	4.16°
3 GHz	#7	**70°**	**44°**	**60°**	0.06°	0.02°	0.12°	**69.83°**	**43.96°**	**60.26°**	1.55°	0.24°	1.63°
	#8	**120°**	**100°**	**0°**	0.09°	0.11°	0.61°	**120.0°**	**100.0°**	**2.51°**	0.23°	0.14°	1.74°
	#9	**30°**	**260°**	**30°**	0.17°	0.32°	0.59°	**30.63°**	**260.0°**	**29.11°**	2.49°	4.87°	6.73°

approach generates a MUSIC spectrum following (4.3) and (4.4).

$$\det\{\mathbf{A}(\theta,\phi)^*\mathbf{E}_{N_0}\mathbf{E}_{N_0}^*\mathbf{A}(\theta,\phi) - \lambda\mathbf{A}(\theta,\phi)^*\mathbf{A}(\theta,\phi)\} = 0 \tag{4.3}$$

$$sp_{MU}(\theta,\phi) = [\text{min root of (4.3)}]^{-1} \tag{4.4}$$

where $\mathbf{A}(\theta,\phi) = [\mathbf{A}_\theta(\theta,\phi), \mathbf{A}_\phi(\theta,\phi)]$ is a 4×2 matrix and $\mathbf{E}_{N_0}$ contains the noise eigenvectors spanning the noise subspace defined in regular MUSIC algorithm (Schmidt, 1986). The approach reported by Ferrara and Parks (1983) is more computationally efficient than the regular MUSIC algorithm as the former dose not search in the polarization dimension. After getting the estimated DoA (denoted by $(\hat{\theta},\hat{\phi})$), the polarization is calculated by solving the quadratic equation system (4.5) that has an explicit solution.

$$\mathbf{A}(\hat{\theta},\hat{\phi})^*\mathbf{E}_{N_0}\mathbf{E}_{N_0}^*\mathbf{A}(\hat{\theta},\hat{\phi})\mathbf{k} = \lambda_{\min}\mathbf{A}(\hat{\theta},\hat{\phi})\mathbf{A}(\hat{\theta},\hat{\phi})\mathbf{k} \tag{4.5}$$

where $\lambda_{\min}$ and $\mathbf{k} = [k_1, k_2]^T$ are the smaller eigen-value and the corresponding eigen-vector. Then, the polarization (γ) is determined with $\tan(\gamma) = k_2/k_1$.

In three randomly-selected DoAs and polarizations of incident waves, the Monte Carlo test results are summarized in Table 4.3. In this table, I list the mean values

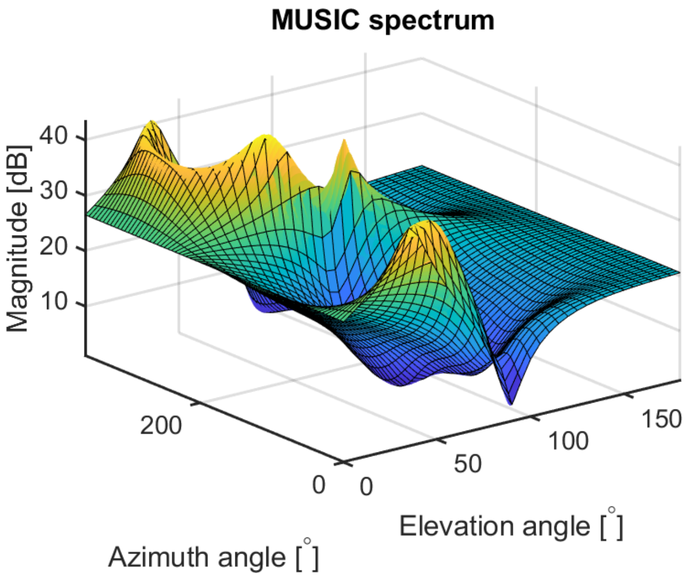

Figure 4.10: A representative MUSIC spectrum observed in Monte-Carlo Test no. 3 at 3 MHz. Multiple peaks presented in the spectrum indicate the emerging of ambiguity.

and root-mean-square (RMS) errors of the estimated DoAs and polarizations, as well as CRB in corresponding directions and polarizations for comparison. Note that the mean values of the DoA and polarization are very close to the real ones, indicating that the proposed design can be effectively used in DF applications, and that the selected MUSIC algorithm is suitable for platform-based DF arrays. Besides, the RMS errors of the Monte-Carlo tests are larger than but reasonably close to the $\sqrt{\mathrm{CRB}}$, and they vary with the same trend. This demonstrates that the proposed design can achieve similar DF accuracy as predicted by the theoretical bounds.

4.4 DF accuracy at other frequencies in the HF band

To evaluate the DF accuracy of the proposed spatially-confined DF array at other HF frequencies, I tuned the matching circuits to match Design D shown in Figure 4.3(d) at 3 MHz and 30 MHz. Then, I simulated the radiation patterns of all array elements using FEKO and computed the CRB patterns at these frequencies. The CRB patterns at 3, 10 and 30 MHz are compared in Figure 4.11(a). Note that the CRB values at 3 MHz are significantly higher than those at 10 and 30 MHz. This is because the modal significance values of the platforms characteristic modes are significantly smaller at this frequency resulting in their inefficiency excitation. Characteristic mode analysis with FEKO showed that, at 3 MHz, only Modes 1 and 2 are excited by the array with normalized weighting coefficients larger than 0.5. This is in contrast to the results obtained at 10 MHz (see Figure 4.5) where four modes are excited with normalized excitation coefficients greater than 0.5. At 30 MHz, the CRB values are comparable to those obtained at 10 MHz and do not show a significant improvement. At higher frequencies, excitation of higher-order modes is easier as their modal significance values are higher. Excitation of these modes can, in principle, enhance the DF accuracy of the array. However, due to the spatially-confined nature of the proposed array and its limited volume, the antenna array still excites a significant amount of lower-order modes at 30 MHz similar to what it does at 10 MHz. Therefore, the CRB values at 30 MHz are comparable with those at 10 MHz. Nevertheless, the CRB values are generally very low (better than 1°) over most of the 4π Sr. field of view. The CRB patterns calculated with using measurement radiation patterns of the 1:100 scaled prototype at 425 MHz, 1 GHz and 3 GHz (corresponding to 4.25, 10 and 30 MHz of the full-scale model) are shown in Figure 4.11(b). These results agree well with the simulation results. The measurement was not conducted at 300 MHz (corresponding to 3 MHz in simulation) because the lowest frequency that our anechoic chamber can measure is 425 MHz.

Also, I conducted Monte-Carlo tests at 3 and 30 MHz following the same procedure described in Section 4.3. The results are shown in Table 4.3. Note that, except for Test no. 3, the mean values and errors of the estimated angles of arrival in the Monte-Carlo tests agree very well with the real angles of arrival and the CRB values. The reason for the failure in Test no. 3 is the emerging of ambiguity. To demonstrate the ambiguity, a representative MUSIC spectrum observed in Test no. 3 is depicted

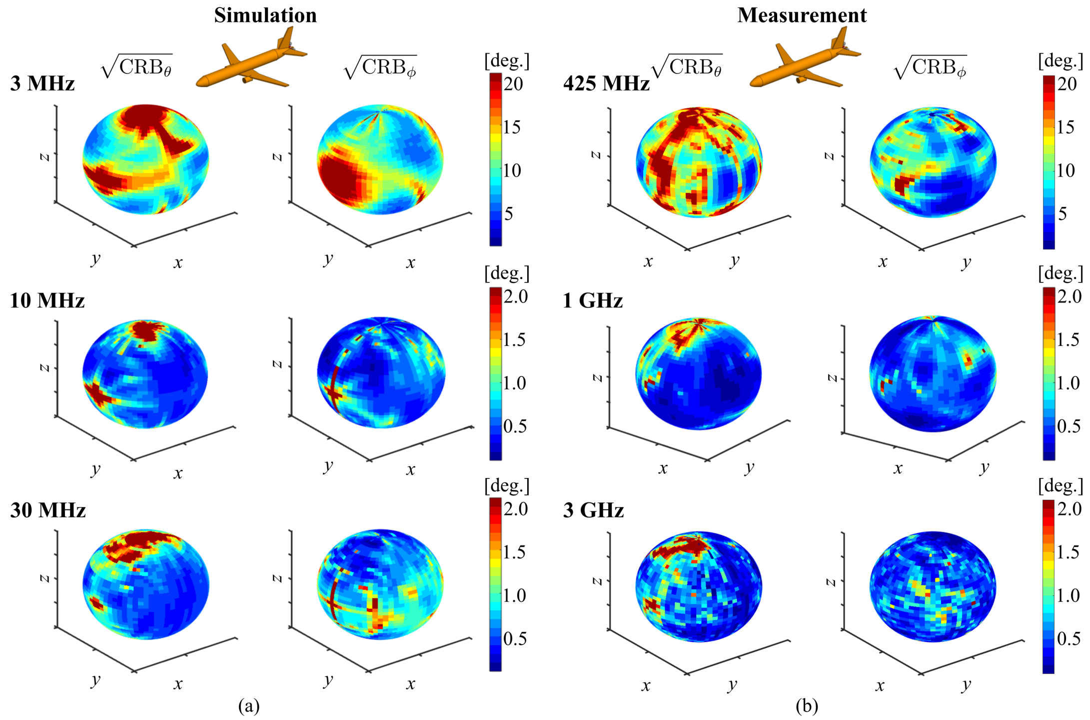

(a) (b)

Figure 4.11: Cramer-Rao bound (CRB) patterns of elevation (θ) and azimuth (ϕ) angle of arrival estimation errors calculated with (a) simulated radiation patterns at 3, 10 and 30 MHz and (b) measured radiation patterns of the 1:100 scaled prototype at 425 MHz, 1 GHz and 3 GHz (corresponding to 4.25, 10 and 30 MHz of the full-scale model). The available SNR is 25 dB, the number of snapshots is 100.

in Figure 4.10. In this spectrum, an isolated peak is presented away from the real DoA (i.e., azimuth and elevation angles of 260° and 30°), and a wide ridge that has multiple small local maxima is centered at the real DoA. In the presence of different specific noise, the heights of the isolated peak and the local maxima on the ridge may vary and one of them will win randomly when the highest peak is chosen as the estimated DoA. This causes the estimated DoA to jump between these peaks for the different DoA runs of the Monte-Carlo simulations, explaining the failure of DF in Test no. 3. From the view of DF array design, the ambiguity is caused by the small number of excited characteristic modes.

4.5 Conclusions

I presented a spatially-confined, platform-based, HF antenna array that has enhanced impedance bandwidth and can achieve a better average Cramer-Rao bound compared to the lowest CRB theoretically achievable from any standalone antenna array occupying the same volume. The proposed four-element array has a maximum linear dimension of 3 m and was strategically placed at a location on the platform that allows it to excite multiple significant characteristic modes at the desired frequency of operation. Compared with the theoretical limit of the CRB value of any standalone array occupying the same volume, the proposed array's CRB is lower by about 15%. A scaled model prototype was fabricated and its S-parameters and radiation patterns were measured. The direction-finding performance of this fabricated prototype was characterized in an emulated environment using its measured and simulated radiation patterns. The measurement and simulation results were in a very good agreement. Moreover, I conducted Monte-Carlo tests with the measured radiation patterns for randomly selected directions-of-arrival and polarizations of incident waves. The test results verified the DF capability of the proposed array. Finally, DF performance of the proposed array at other frequencies in the HF band was evaluated using numerical simulations.

5 A COMPACT, BROADBAND, MULTIBEAM VHF/UHF ANTENNA ARRAY FOR DIRECTIONAL NETWORKING AND DIRECTION FINDING APPLICATIONS

5.1 Introduction

The frequency band 225–400 MHz is widely used in land, maritime, airborne and satellite communication and navigation operated by the military and government agencies in North Atlantic Treaty Organization (NATO) member nations and many other nations all over the world. Typical applications include the ILS Glideslope navigation systems, Army's Area Common User System for land mobile and fixed communication, and many air-ground-air communication extensively used by the military agencies and U.S. Cost Guard (National Telecommunication and Information Administration, 2014). In these wireless communication systems, directional antennas and directional networking techniques are promising approaches of increasing the channel capacity, reducing the probability of detection/interception, and monitoring cooperative and uncooperative sources. While commercial directional antennas, such as log periodic antennas (Kathrein Scala, 2020) and spiral antennas (M2 Antenna Systems, 2020), can cover the frequency band and provide narrow beamwidth, they usually have a large dimension of around two wavelengths at the center frequency (2 m). As a result, a practical array composed of several these antennas can hardly be deployed on high-mobility military trucks.

Over last two decades, many compact antennas having directional radiation patterns have been reported. Among them, Huygens source antennas that possess a volume with the maximum dimension less then 0.9 wavelength at center frequency can provide cardioid-shaped patterns over up to nearly an octave frequency band (Luk and Wong, 2006; Seo and Kishk, 2011; Li and Luk, 2012; Wong et al., 2008; Luk and Wu, 2012). Huygens source antennas radiate a cardioid-shaped pattern with gain up to 5 dBi, by combining a figure-eight shaped pattern of a electric dipole and a omni-directional pattern of a collocated, perpendicularly-oriented magnetic dipole. Luk and Wu (2012) summarized a variety of state-of-the-art wideband Huygens source antennas. The dimension of the Huygens source antennas can further go down to less then 0.2 wavelength at the center frequency by employing miniaturization techniques and introducing resonant structures inspired by frequency selective surfaces (Tang et al., 2016; Jin and Ziolkowski, 2010; Best, 2010; Tang et al., 2017). However, the small dimension comes at a price of narrow bandwidth. Aside from Huygens source antennas, the self-grounded bow-tie antenna was reported to have cardioid-shaped pattern with a compact size (Yang and Kishk, 2012; Raza et al., 2014). This antenna has simpler structure and much wider bandwidth than the wideband Huygens source antennas but with slightly larger dimension. However, similar to the Huygens source antennas, its beam points towards the broadside of the ground plane, making it unfavorable to the most majority of ground-to-ground and ground-to-air applications in the 225–400 MHz band. To compensate this issue, electrically steerable passive array radiator (ESPAR) antennas are a good alternative (Kawakami and Ohira, 2005; Ojiro et al., 2001; Alshami et al., 2009; Schlub et al., 2003; Schlub and Thiel, 2004). An ESPAR antenna is composed of a single active radiator and several passive elements placed around the active radiator. The passive elements are terminated to electronically-controllable reactors or PIN diodes. By tuning the passive elements' terminations, people can steer the beam direction in the azimuth plane. ESPAR antennas are also suitable for direction of arrival (DoA) estimation (Taillefer et al., 2005; Rzymowski et al., 2016). Compared with steering figure-eight shaped pattern that is commonly-used in small-aperture DoA (Mingjian Li, 2018; Ghaemi et al., 2018),the ESPAR antennas have irreplaceable advantage of no ambiguity because of its directional patterns. However, ESPAR antennas usually have limited bandwidth of less than 20%. Our group proposed a wideband antenna featured as low-profile and vertically polarized directional radiation (Ghaemi and Behdad, 2016). This antenna steers the cardioid-shaped pattern towards four directions by giving different phase of excitation to its four loop-like elements. However, both ESPAR antennas and our design can radiate a single beam at a time. This makes them unable to simultaneously communicate with multiple users in different directions, leaving them unfavorable for directional networking applications.

In this chapter, I proposed a compact, broadband, multibeam VHF/UHF antenna array by strategically arranging multiple electric and magnetic dipoles/monopoles in a compact volume. This array can cover the 225–400 MHz frequency band and simultaneously transmit/receive via eight independent beams with vertical polarization. It is suitable for both directional networking and direction finding applications. The maximum linear dimension of a single element of the array is less then half wavelength at the center frequency while the gain is enhanced by more than 2 dB compared with typical Huygens source antennas. Using this antenna to create an eight-element uniform circular array, I was able to fit the entire array in a 4×4×1 ft^3 volume. Simulation results of a single antenna element and the array were reported with and without the presence of realistic earth surface. Further, the DoA capability were investigated by using Cramer-Rao bound and Monte-Carlo experiments.

5.2 Antenna Element Design

Let's start from a single antenna design befor employing it to create an eight-element uniform circular array. I first determine an initial dimension for the single-element design. As shown in Figure 5.1, due to simple geometry relationship, I assume a single antenna element should fit in a volume of 50×30×30 cm^3, so that a uniform circular array composed of eight such antennas can fit in a 4×4×1 ft^3 (121×121×30 cm^3) volume.

The antenna element design is inspired by Huygens source antennas. Huygens source antennas combine a figure-eight shaped and an omni-directional radiation patterns and create a cardioid-shaped radiation pattern of 5 dBi. To increase the gain, as shown in Figure 5.2, I employ two electric monopoles to create an elliptical pattern for more gain along the broadside of the two-element array. Besides, a magnetic dipole is lifted up above the ground plane, such that the magnetic dipole together with its mirror can create a figure-eight shaped pattern with more gain in the azimuth plane. Then, I combine the elliptical and the higher-gain, figure-eight

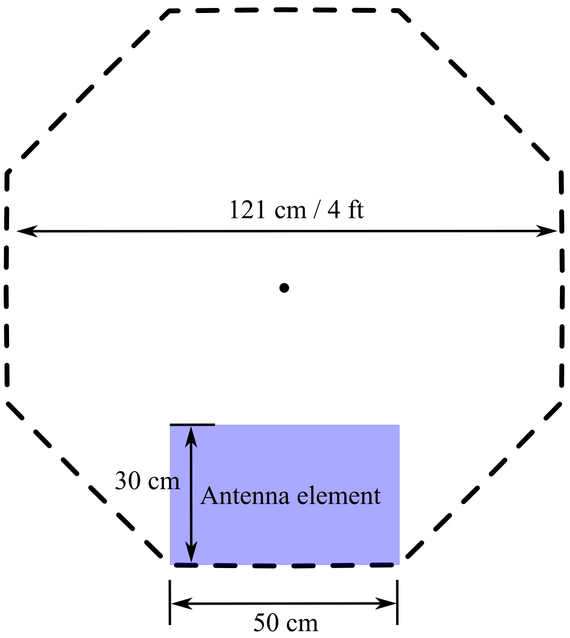

Figure 5.1: The area possessed by a single antenna element.

shaped patterns and create a cardiod-shaped pattern with greater gain and vertical polarization in the azimuth plane.

Initial design

This idea was implemented straightforwardly in the design shown in Figure 5.3. This antenna is composed of a two monopoles shorted to the ground and marked by red arrows, and a loop on top of the monopoles. For wider bandwidth, the monopoles are in triangular shape and the loop tappers from feed point to full width of 31 cm. The loop creates a horizontally oriented magnetic dipole denoted by blue arrow in Figure 5.3. The dimensions of the antenna are marked in Figure 5.3.

Full wave simulations was performed by using CST Microwave Studio. In the simulations, the antenna is made of perfect electric conductor as metal in the VHF/UHF band has very low loss. The antenna was placed on top of an infinite PEC ground plane. The reflection coefficients is shown in Figure 5.4. The -10

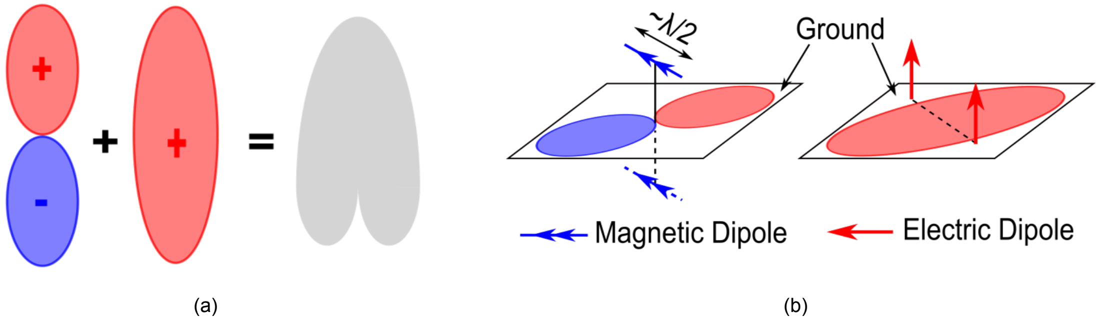

Figure 5.2: (a) Combining an elliptical pattern and an figure-eight pattern with higher gain in the azimuth plane can create a cardioid-shaped pattern with higher gain than conventional Huygens source antenna. (b) Magnetic dipole together with its mirror can create a figure-eight shaped pattern with more gain in the azimuth plane. Two monopoles can create an elliptical pattern with more gain along the broadside of the two-element array.

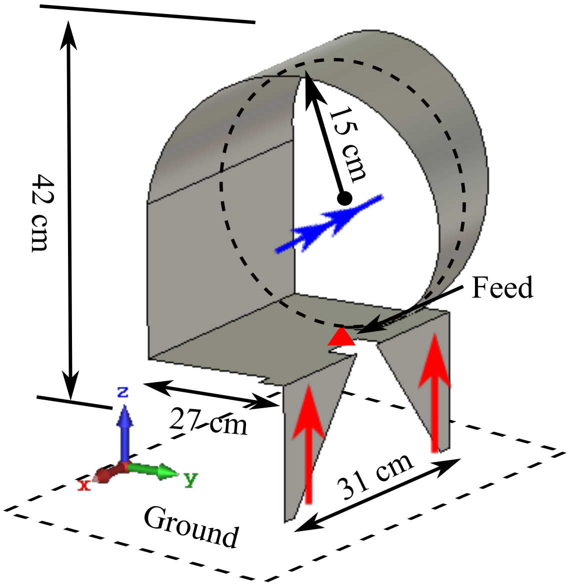

Figure 5.3: Perspective view and dimensions of the design composed of two monopoles and a lifted loop.

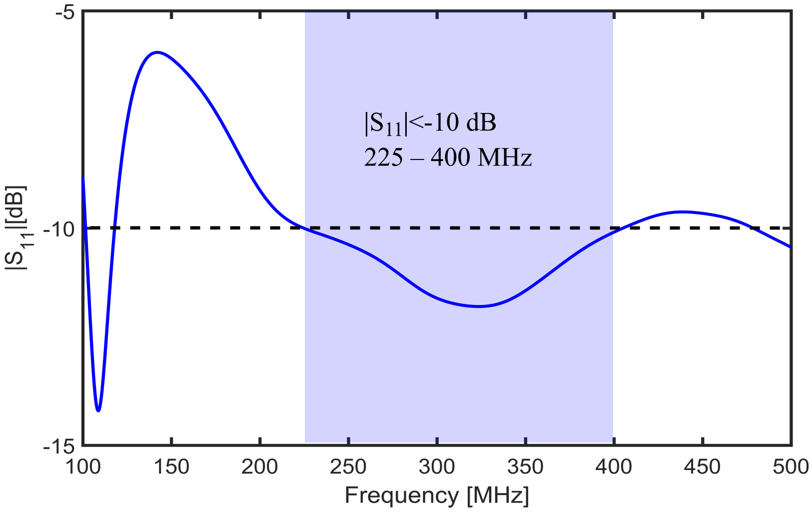

Figure 5.4: Magnitude of reflection coefficients of the proposed design shown in Figure 5.3.

dB bandwidth covers the 225–400 MHz band. The realized gain patterns in the azimuth and elevation planes are shown in Figure 5.5. This antenna is vertically polarized in the azimuth plane. The realized gain ranges from 4.9 to 7.2 dBi and the front-to-back ratio from 8 to 24 dB.

However, the gain is only slightly higher than that of a classic Huygens source (i.e., 5 dBi), especially at higher frequencies. The reason is illustrated in Figure 5.6(a) showing the 3D radiation pattern at 350 MHz with infinite PEC ground plane. Note that the maximum radiation direction direction is in the azimuth plane, but there is undesired strong radiation in the region highlighted by a red circle. This issue exacerbates when using a finite ground plane in practical applications. In the case of using a 3.6×3.6 m^2 rectangular ground plane, the beam even splits as shown in Figure 5.6(b).

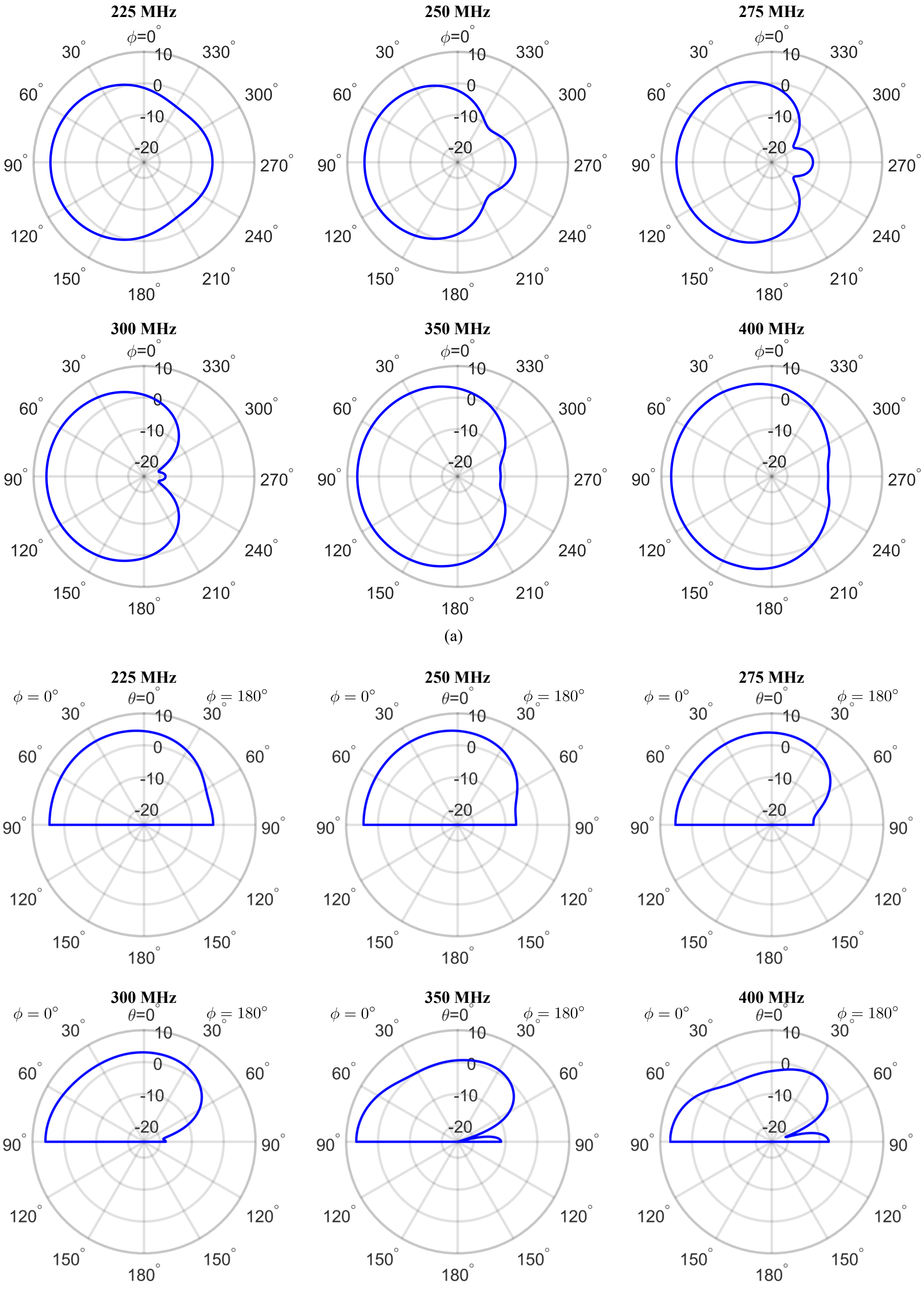

(a)

(b)

Figure 5.5: Radiation patterns in the (a) azimuth and (b) elevation planes.

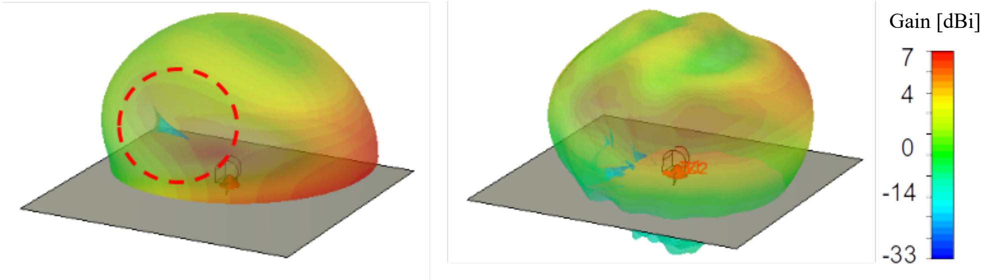

(a) (b)

Figure 5.6: 3D radiation pattern at 350 MHz with (a) infinite PEC ground plane and (b) 3.6×3.6 m^2 rectangular ground plane. The red circle in (a) highlights the region with undesired high gain.

A design with higher gain

To further increase the gain and heal the splitted beam, I lowered the loop and put the monopole in the front of the loop. The side and front views of this design are shown in Figure 5.7(a) where the antenna is placed on a circular-shaped ground plane with diameter of 2 m. The dimension of the ground plane is chosen such that it can be easily installed on commonly used military trucks. The reflection coefficients shown in Figure 5.8 demonstrate a good impedance matching in the 225–400 MHz band. The antenna is vertically polarized in the azimuth plane. The gain in the frequency band ranges from 7.0 to 7.6 dBi (as shown in Figure 5.10), which is about 0.4-2.1 dB greater than the initial design. The realized-gain patterns in azimuth and elevation planes at representative frequencies in the 225–400 MHz band are shown in Figure 5.9(a). Note that the take-off angle is about 40 degree. The large take-off angle results from the finite size of the ground plane and can reduce the again in the azimuth plane. In some ground-to-ground communications where ground wave dominates, it is favorable to have greater gain in the azimuth plane and smaller take-off angle.

To reduce the take-off angle, skirted ground was employed. This design with a 2 m diameter ground plane is named as Design A whereas that with a skirted ground plane is named as Design B. Their structure and dimensions are compared in Fig-

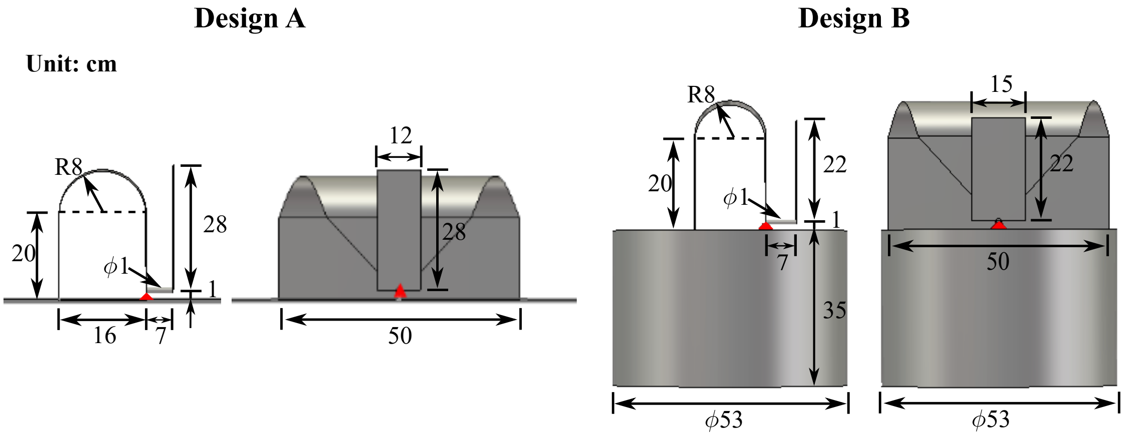

(a)

(b)

Figure 5.7: The side and front views of the revised design with higher gain on top of (a) a circular-shaped ground plane with diameter of 2 m and (b) a skirted ground plane.

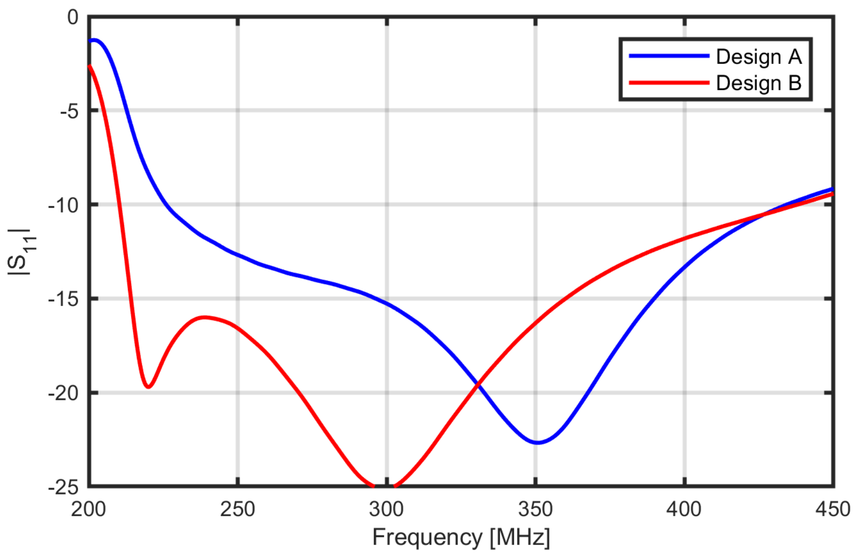

Figure 5.8: Magnitude of S_{11} of the Designs A and B shown in Figure 5.7.

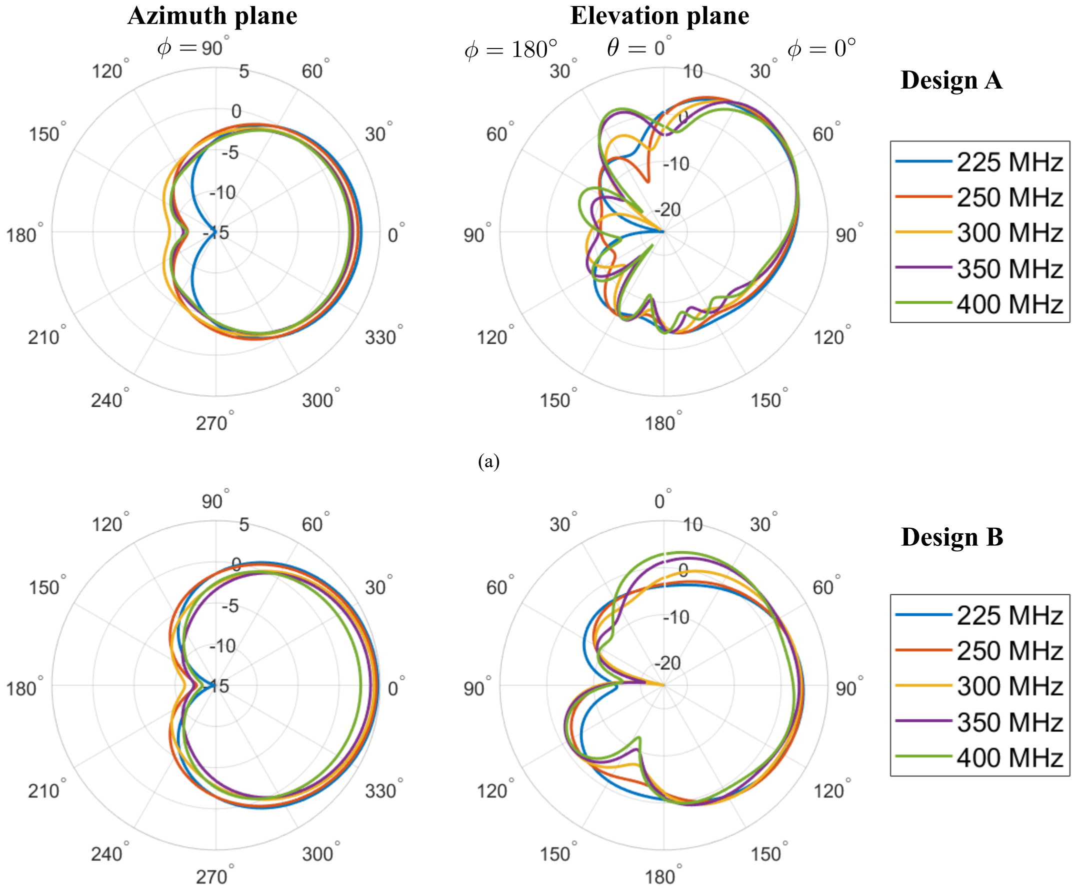

(a)

(b)

Figure 5.9: Realized-gain patterns in azimuth and elevation planes of (a) Design A and (b) Design B.

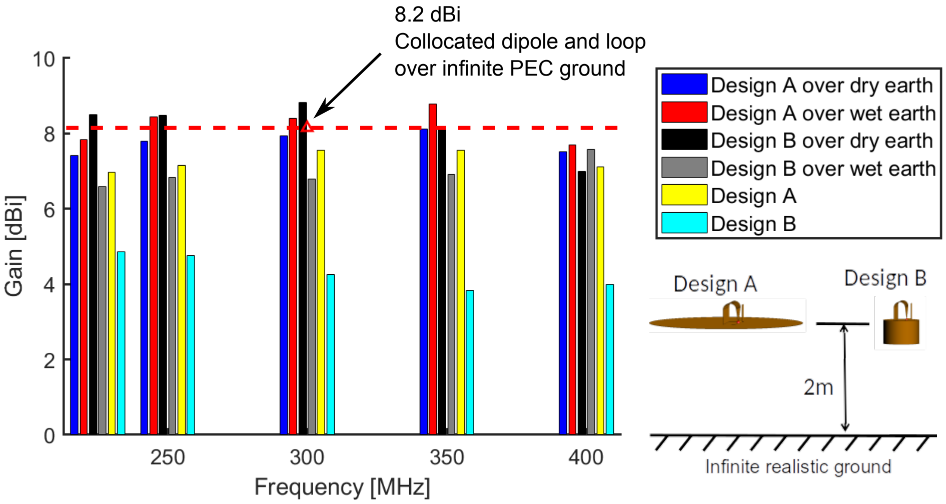

Figure 5.10: Comparison of gains of Designs A and B in different earth surface conditions.

ure 5.7. Design B is taller in height because of the height of the skirted ground. The realized-gain patterns in azimuth and elevation planes at representative frequencies in the 225–400 MHz band are shown in Figure 5.9(b). Note that the maximum radiation directions in the frequency band are in the azimuth plane, and the gain in the azimuth plane increases by around 2 dB compared with Design A.. However, the maximum gain drops by around 3 dB as compared in Figure 5.10. This results from more radiation below the ground in the case of using skirted ground as its diameter is much smaller than 2 m (shown in Figure 5.7(b)).

5.3 Effect of realistic earth surface

In the applications when the antenna is deployed on top of ground vehicles, the presence of realistic earth surface have considerable impact on the radiation pattern of the antenna. In the VHF/UHF frequency band, the realistic earth surface can be modeled as an infinite-large flat ground plane with infinite thickness composed of the realistic earth material. The dielectric properties of realistic earth surface varies considerably as a function of the composite, moisture and temperature among others. The dielectric properties of realistic earth surface has been thoroughly modeled by International Telecommunication Union (ITU) in Recommendation ITU-R P.527-4 (ITU Recommendation, 2017). I chose dry and wet silty loam as the representative earth surfaces and simulate, with Altair FEKO, the radiation pattern where the Designs A and B are placed 2 m above the earth surface. The 2 meter height is chosen as it is a rough estimate of the height of a military truck. The specific relative permittivity of these two types of earth surfaces is plotted in Figure 5.11. The wet earth are more conductive with greater permittivity (ϵ'). This agrees with the intuition that water itself has greater permittivity and that water contents can enhance earth conductivity by resolving mineral materials. The 3-D radiation patterns at 300 MHz in different earth surface conditions are compared in Figure 5.12. Note that, due to the infinite size of the realistic earth surface, radiation below the ground is zero. However, it is still a directional pattern. Besides, because of the finite conductivity of the earth surface, there is a small take-off angle, even for the design with skirted ground. Further, ripples along the elevation angle can be observed as the distance between antenna to the earth surface is two wavelength.

The realized gain values over the frequency band are compared in Figure 5.10. Observe that the gain increases when the realistic earth surface presents in the presence of earth surfaces as they rejected radiation below horizon. Note that Design A has higher gain than Design B and is less effected by the variation of earth condition, making it more desirable for directional networking applications. As a result, Design A is selected for further investigation.

Three key parameters to impedance matching of Design A was investigated. They are the radius of loop (denoted by R), the diameter of the pole connecting the loop and the monopole in the front(denoted by ϕ), and width of the monopole in the front (denoted by W). The magnitude of S_{11} with different values of these parameters is plotted in Figure 5.13. To summarize, larger radius of loop results in smaller reactance and smaller reflection. Moreover, Lager diameter of the pole connecting the loop and the monopole improves matching at lower frequencies but increases cut off frequency in the lower end. Besides, wider monopole has lower

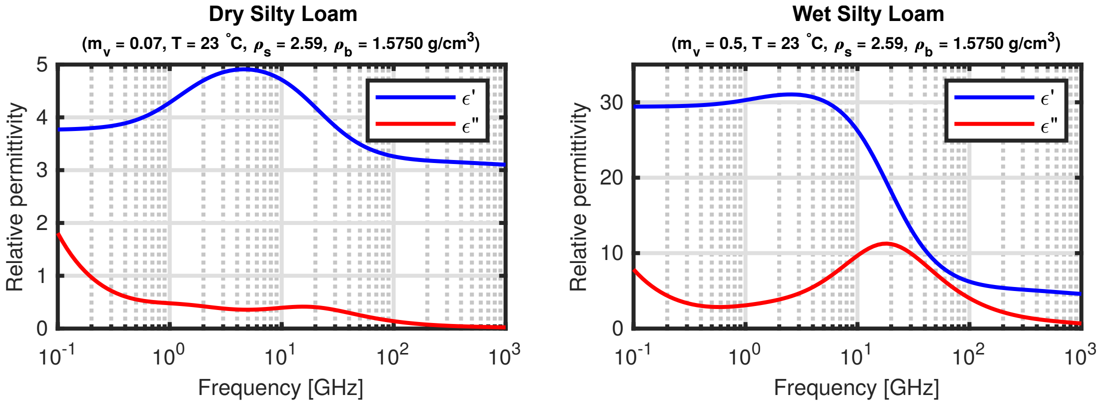

(a)

(b)

Figure 5.11: Relative permittivity of (a) wet silty loam and (b) dry silty loam, where m_v denotes the volumetric water content, T is temperature, ρ_s denotes the specific gravity of the dry mixture of soil constituents, and ρ_b denotes the bulk density of the soil.

cut off frequency in the lower end.

5.4 Array simulation

A uniform circular array composed of eight Design As is employed to generate eight independent beam. The array structure and its dimensions are demonstrated in Figure 5.14. The array is mounted on a circular-shaped ground plane with a diameter of 2 m. A few changes were made to the original Design A to fit it in the array environment. Specifically, the back side of the loop in Design A was made narrower, so that the array can fit in a 4 ft×4 ft area. Also, the dimensions of the antennas were slightly modified for enhanced impedance matching in the array environment.

Simulations were performed with using Altair FEKO, a full-wave electromagnetic simulation software, assuming no earth surface presented. The simulation S-parameters are depicted in Figure 5.15. For brevity and symmetry, only some of the S-parameters were shown. Note that the -10 dB bandwidth is 225–450 MHz

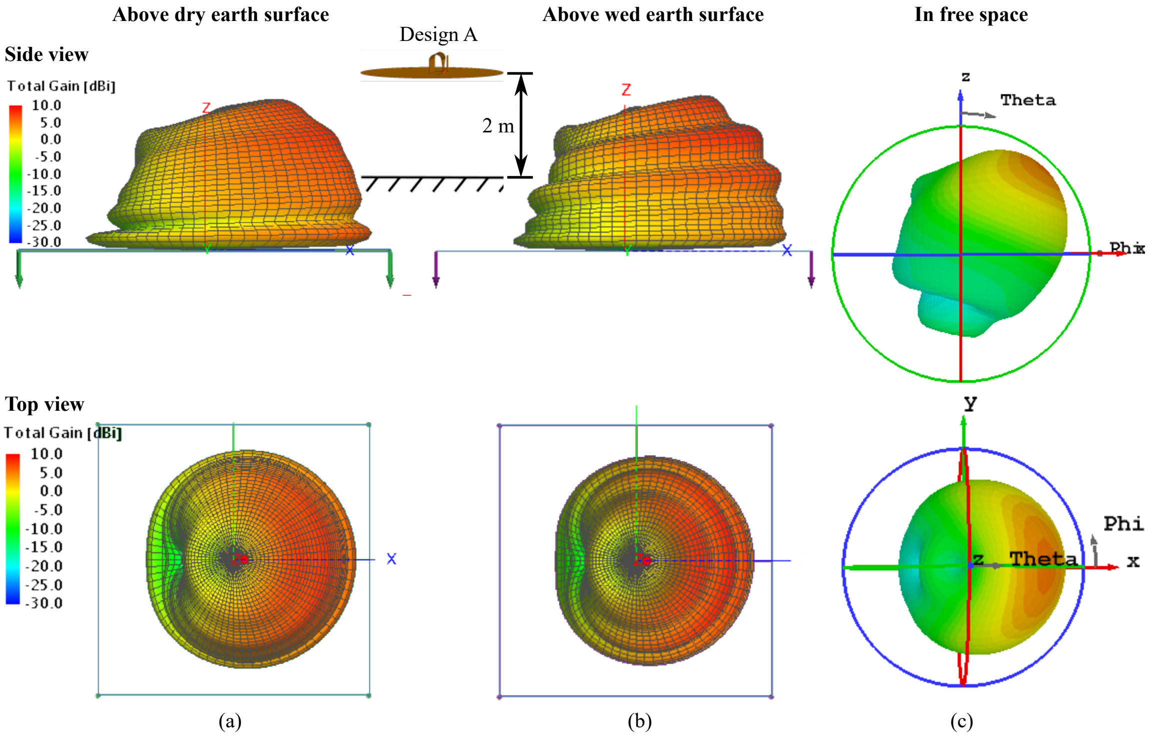

Figure 5.12: 3-D realized-gain patterns of Designs A and B placed 2 m above (a) dry and (b) wet earth surfaces, and (c) those without the presence of earth surface.

with a good isolation of more than 15 dB between elements. Realized gain patterns in the azimuth and elevation planes are shown in Figure 5.16. For symmetry and brevity, patterns of the rest elements were omitted. As can be seen, the antenna radiates directional patterns. The front-to-back ratio is greater than 12 dB and the gain ranges 3.7–6.7 dBi in the frequency band. The gain is 0.9-3.3 dB lower than that of a standalone antenna because of the influence of the nearby elements in the array environment. Besides, the antenna is still vertically polarized in the azimuth plane.

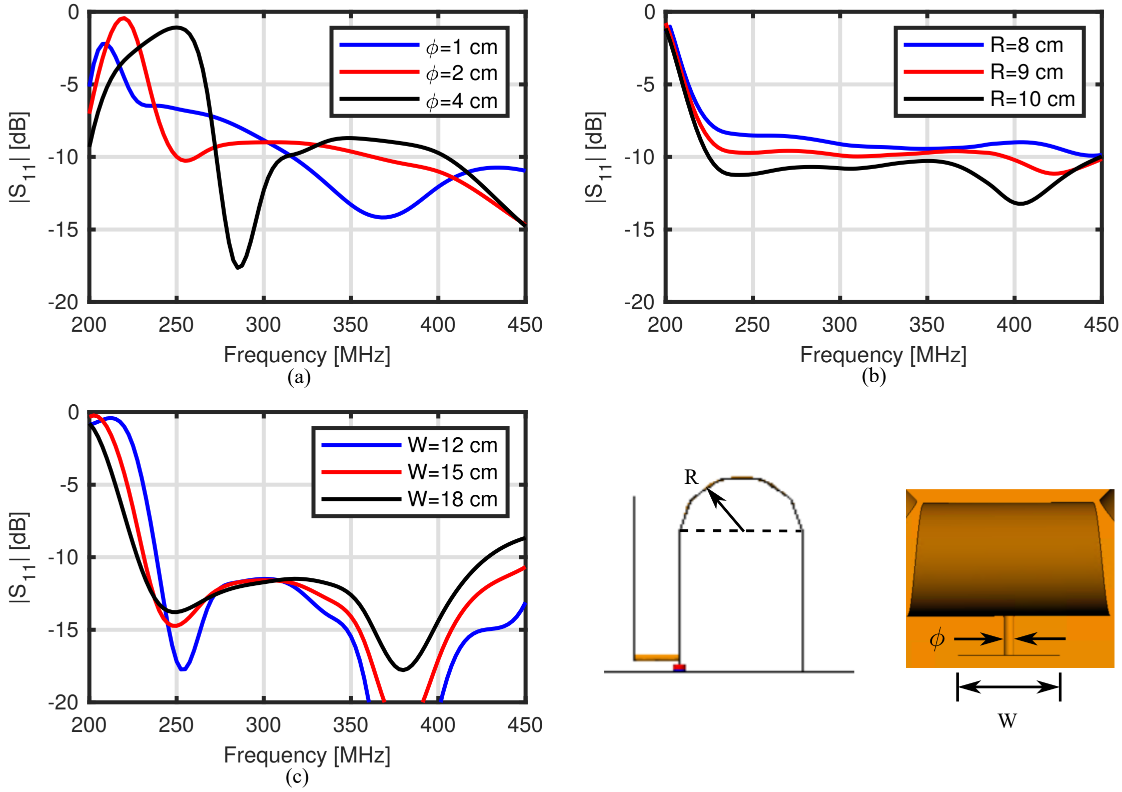

(a) (b) (c)

Figure 5.13: Magnitude of S_{11} with different values of (a) the radius of the loop (R), (b) the diameter of the pole connecting the loop and the monopole in the front (D), and (c) the width of the monopole in the front (W).

5.5 Characterization of direction finding capability

Using the simulation radiation patterns, the Cramer-Rao bounds in the azimuth plane were calculated. The results are shown in Figure 5.17, at five representative frequencies in the band of 225–400 MHz and under three signal-to-noise ratios (SNR) ranging in 0–20 dB. I assumed eight incoherent receivers, so only the magnitude of the patterns was used. Note that the CRB varies periodically as a function of azimuth angle. The period is 45 degree which agree with the rotational symmetry of the eight-element uniform circular array. For different SNR and frequencies, the averaged CRB over the azimuth angle of 0°–360° were shown in Figure 5.18. Note

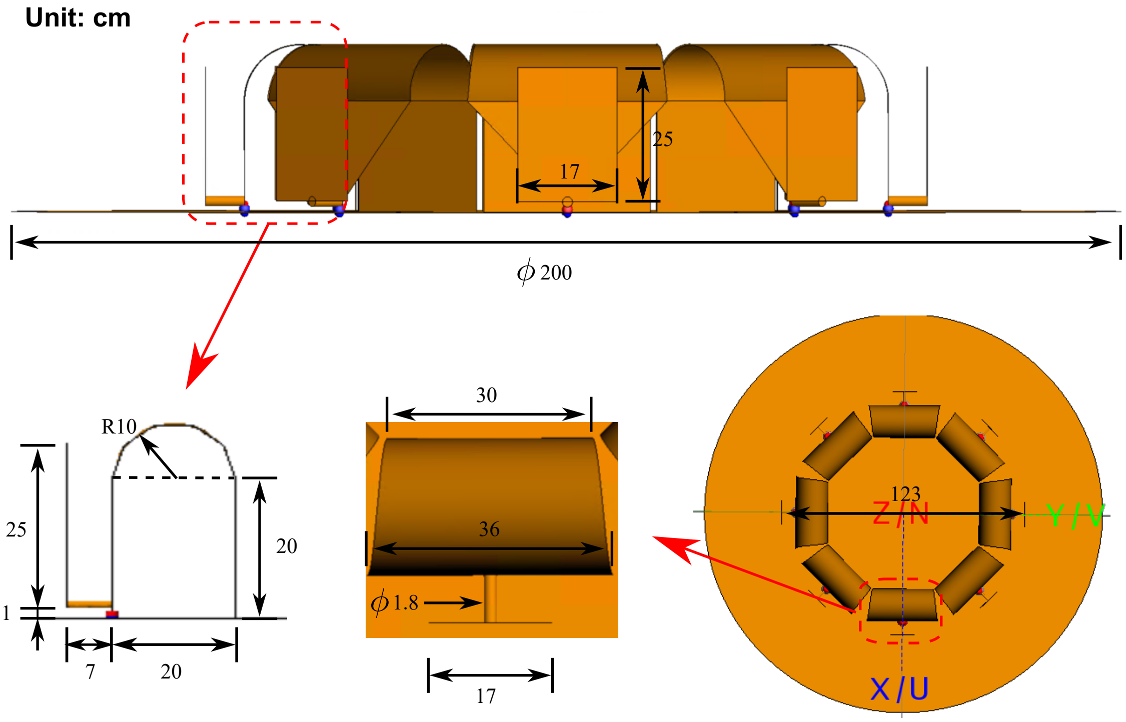

Figure 5.14: Side and top view of the array and antenna elements. Dimensions are marked in centimeter.

that, as expected, the averaged CRB decreases as the SNR goes higher. Besides, the CRB at higher frequencies is smaller because of greater gain and directionality. An exception is that the CRB at 250 MHz is lower than that at 225 MHz, though they are rather close. Part of the reason can be attributed to that the phase between antenna elements was not employed. The phase variation at higher frequencies is more than that at lower frequencies. This larger phase variation conveys more directional information at higher frequencies. The other reason is that the realized gain at 250 MHz is equal or lower than that at 250 MHz. Lower CRB results from not only the faster angular variation of the patterns but also greater absolute value of gain. As shown in Figure 5.16(a), the variation of the radiation pattern 250 MHz is slightly faster than that at 225 MHz, or narrower beam width. However, the

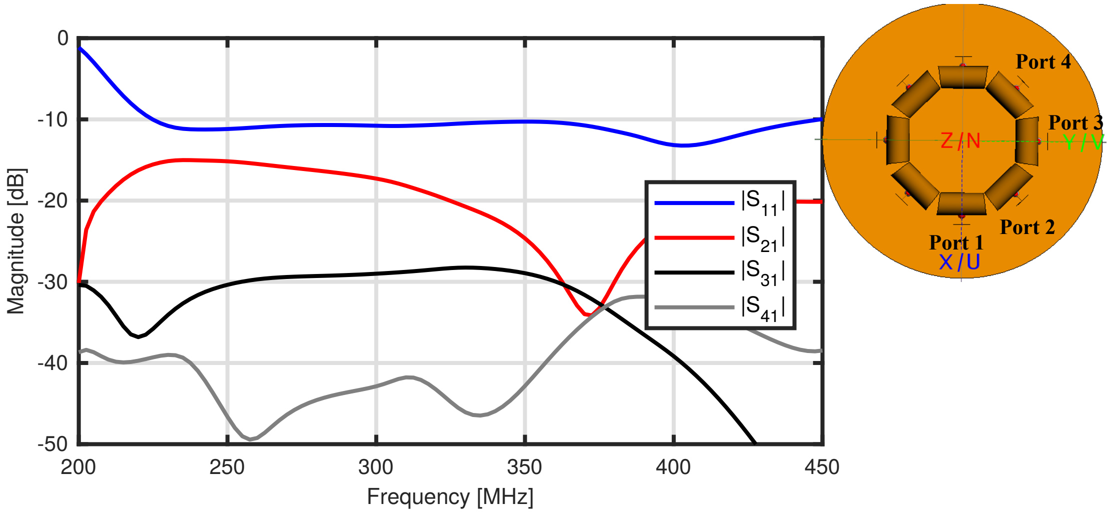

Figure 5.15: Simulation S-parameters of the antenna array.

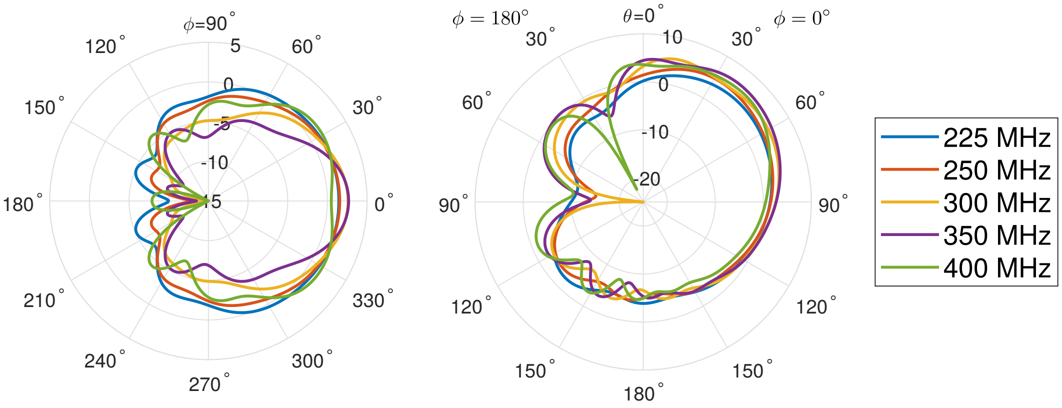

(a)

(b)

Figure 5.16: Realized gain patterns of an antenna element in the array environment in the (a) azimuth and (b) elevation planes. Patterns of the rest elements are omitted because of symmetry and brevity.

realized gain at 250 MHz is considerably lower in from 30° to 330°. The lower gain results in lower SNR, diminishing the contribution from faster angular variation of the pattern.

Monte-Carlo experiments were then performed at 10 randomly-selected azimuth angles. For each angle of arrival, it was done as follows:

1. Simulate signal at the AoA using the simulation radiation patterns.
2. Add Gaussian white noise based on the pre-selected SNR.
3. Employ MUSIC algorithm to estimate the AoA.
4. Repeat Steps 1–3 for 500 times and calculate mean and root-mean-square error (RMSE) of the estimated AoAs.

In these experiments, I assumed a single impinging wave with vertical polarization. Also, 100 samples were used for each estimation. The results under SNR of 0, 10 and 20 dB and at frequencies of 225, 250 300, 350 and 400 MHz are shown in Figure 5.17. As can be seen, the RMSEs are slightly higher than the $\sqrt{\mathtt{CRB}}$ and the difference between the mean value of the estimated AoA and the real AoA (defined as bias) is very small. The results demonstrate a good DF accuracy at low SNR over a wide frequency band.

5.6 Conclusion

A compact, broadband, multibeam VHF/UHF antenna array was developed for directional networking and direction finding applications. The array can generate eight independent beams in the frequency range of 225–400 MHz. The array possesses a volume of $4\times4\times1$ ft^3 and is installed on a circular-shaped ground plane with diameter of 2 m. Simulation results demonstrated that the single antenna element can generate gain of 7.0–7.6 dBi over the 225–400 MHz band while each element of the array can generate 3.7–6.9 dBi gain because of the adverse influence of the nearby array elements. The DF accuracy of the antenna array was characterized

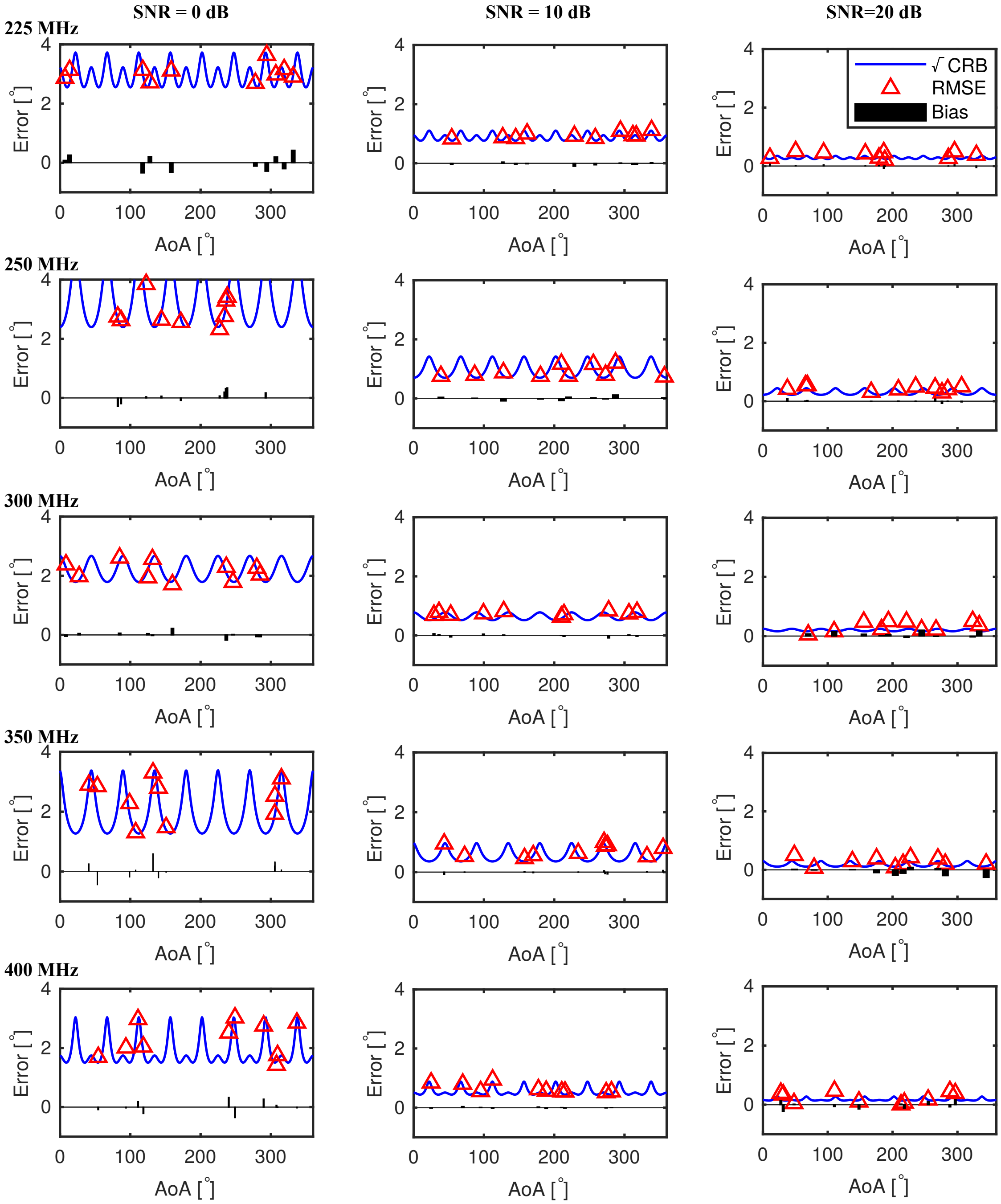

Figure 5.17: Cramer-Rao bounds (CRB) and root mean square error (RMSE) and bias of Monte-Carlo experiments at ten randomly-selected angles of arrivals (AoAs) in the azimuth plane were depicted. The results under SNR of 0, 10 and 20 dB and at frequencies of 225, 250 300, 350 and 400 MHz are shown. The number of snapshot is 100.

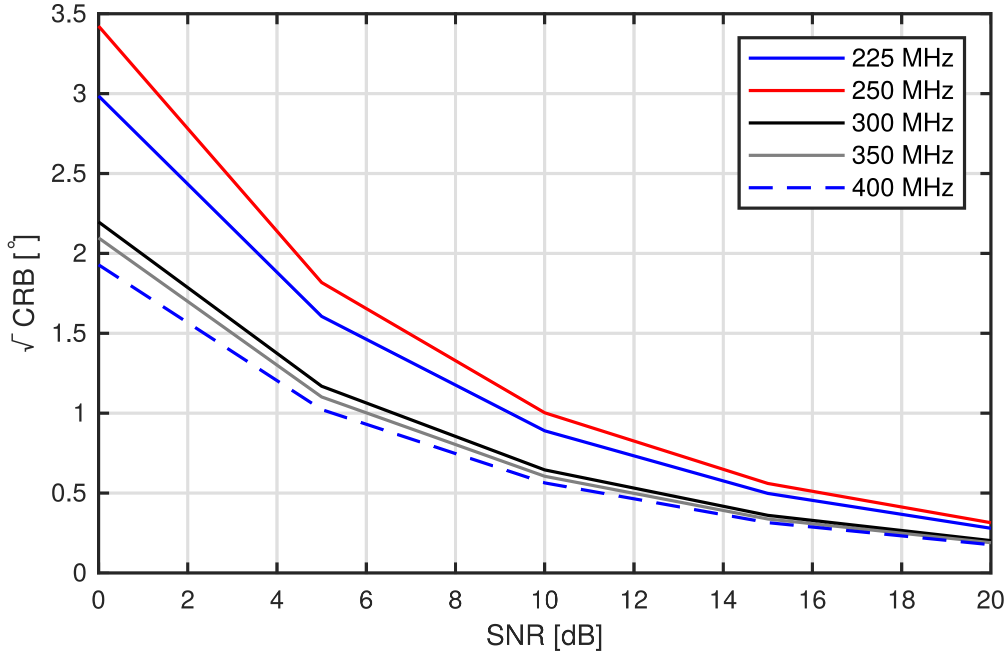

Figure 5.18: CRB at different frequencies and SNRs. The CRB is averaged over the azimuth angle of 0°–360°. The number of snapshot is 100.

in a wide range of frequency, SNR, and angle of arrivals with using Cramer-Rao bounds and Monte-Carlo experiments. The results demonstrate that the array can provide a good DF accuracy at low SNR over the entire 225–400 MHz band.

6 FUTURE WORK

In this dissertation, I have investigated approaches for developing wideband, small-aperture antenna arrays for direction of arrival estimation applications. These approaches include optimizing array geometry and antenna structure as discussed in Chapter 1, employing the platform characteristic modes in Chapters 2 and 3, and using multibeam array with multiple cardioid-shaped radiation patterns as discussed in Chapter 4. However, the research can be extended in the following topics: wideband design methodology and effect of mutual coupling.

The approaches used in previous chapters relies on examining the DF performance at multiple discrete frequencies over the operating frequency band. For example, in Chapters 2 and 3, the characteristic mode (CM) theory was employed to analyze and guide the DF array design at multiple frequencies in the HF band. However, CMs change gradually as a function of frequency, making it difficult to select one set of CMs that is suitbale for the entire band. Besides, optimization performed at one frequency may compromise the effort at other frequencies. These observations strongly imply that the frequency domain may not be the simplest perspective for designs with bandwidth over multiple octaves. Therefore, it is favorable to create a novel perspective that explicitly involves bandwidth and builds a direct connection between antenna structure change to the DF accuracy over the entire frequency band instead of multiple discrete frequencies.

Mutual coupling is another important factor that can greatly influence the accuracy of DF systems. However, electrically small antennas tend to have strong coupling among the antennas in the same array and between the antennas and the ambient environment. While the unexpected mutual coupling is usually harmful to DF accuracy in practical DF systems deployed in unknown environment, the success of the platform-based DF arrays discussed in Chapters 2 and 3 depends on wisely exploiting the coupling between the DF array and the platform. As a results, systematic investigation on the effect of mutual coupling in small-aperture DF arrays is of great practical importance and is highly likely to produce novelty.

REFERENCES

Adcock, Frank. 1919. Improvement in means for determining the direction of a distant source of electromagnetic radiation. *British patent* 130490.

Akaike, Hirotugu. 1974. A new look at the statistical model identification. *IEEE transactions on automatic control* 19(6):716–723.

Alrmah, Mohamed A, Stephan Weiss, and Sangarapillai Lambotharan. 2011. An extension of the MUSIC algorithm to broadband scenarios using a polynomial eigenvalue decomposition. In *Signal processing conference, 2011 19th european*, 629–633. IEEE.

Alshami, B., H. Aboulnour, and M. Dib. 2009. Design of a broadband espar antenna. In *2009 mediterrannean microwave symposium (mms)*, 1–6.

Archer, Michael D. 2013. High frequency magnetic field direction finding using MGL-S9A B-dot sensors. Master's thesis, Air Force Inst of Tech Wright-Patterson AFB OH Graduate School of Engineering and Management.

Bailey, MC, TG Campbell, CJ Reddy, RL Kellogg, and Phuc Nguyen. 2012. Compact wideband direction-finding antenna. *IEEE Antennas and Propagation Magazine* 54(6):44–68.

Balanis, Constantine A. 2016. *Linear wire antennas*, chap. 4, 203–210. John Wiley & Sons.

Barabell, Arthur. 1983. Improving the resolution performance of eigenstructure-based direction-finding algorithms. In *Acoustics, speech, and signal processing, ieee international conference on icassp'83.*, vol. 8, 336–339. IEEE.

Bellini, Ettore, and Alessandro Tosi. 1909. System of directed wireless telegraphy. US Patent 943960.

Best, S. R. 2010. Progress in the design and realization of an electrically small huygens source. In *2010 international workshop on antenna technology (iwat)*, 1–4.

Best, Steven R. 2005. Low Q electrically small linear and elliptical polarized spherical dipole antennas. *IEEE Transactions on Antennas and Propagation* 53(3): 1047–1053.

Bindel, David S, James W Demmel, Mark J Friedman, Willy JF Govaerts, and Yuri A Kuznetsov. 2005. Bifurcation analysis of large equilibrium systems in MATLAB. In *International conference on computational science*, 50–57.

Boeing Commercial Airplanes. 2004. Boeing 737 airplane characteristics for airport planning.

Cabedo Fabres, Marta. 2008. Systematic design of antennas using the theory of characteristic modes. Ph.D. thesis, Departament de Comunicacions, Universitat Politècnica de València.

Cabedo-Fabres, Marta, Eva Antonino-Daviu, Alejandro Valero-Nogueira, and Miguel Ferrando Bataller. 2007. The theory of characteristic modes revisited: A contribution to the design of antennas for modern applications. *IEEE Antennas and Propagation Magazine* 49(5):52–68.

Cabedo-Fabres, Marta, Alejandro Valero-Nogueira, JI Herranz-Herruzo, and M Ferrando-Bataller. 2004. A discussion on the characteristic mode theory limitations and its improvement for the effective modeling of antennas and arrays. In *Antennas and propagation society international symposium, 2004. ieee*, vol. 1, 121–124. IEEE.

Carter, G Clifford. 1993. *Coherence and time delay estimation: an applied tutorial for research, development, test, and evaluation engineers*. IEEE.

Chandran, Sathish. 2005. *Advances in direction-of-arrival estimation*. Artech House.

Chaudhury, Shameem Kabir, Werner L Schroeder, and HJ Chaloupka. 2007. MIMO antenna system based on orthogonality of the characteristic modes of a mobile device. In *Antennas, 2007. inica'07. 2nd international itg conference on*, 58–62. IEEE.

Chen, Yikai, and Chao-Fu Wang. 2015a. *Characteristic modes: Theory and applications in antenna engineering*. Hoboken, NJ: John Wiley & Sons.

———. 2015b. HF band shipboard antenna design using characteristic modes. *IEEE Transactions on Antennas and Propagation* 63(3):1004–1013.

Chen, Zhizhang, Gopal Gokeda, and Yiqiang Yu. 2010. *Introduction to direction-of-arrival estimation*. Artech House.

Chu, Lan Jen. 1948. Physical limitations of omni-directional antennas. *Journal of Applied Physics* 19(12):1163–1175.

Collin, R., and S. Rothschild. 1964. Evaluation of antenna Q. *IEEE Transactions on Antennas and Propagation* 12(1):23–27.

Corbin, Clair F. 2011. High frequency direction finding using structurally integrated antennas on a large airborne platform. Master's thesis, Air Force Inst of Tech Wright-Patterson AFB OH Graduate School of Engineering and Management.

Dieci, Luca, and Timo Eirola. 1999. On smooth decompositions of matrices. *SIAM Journal on Matrix Analysis and Applications* 20(3):800–819.

Drosopoulos, A, and S Haykin. 1992. Adaptive radar parameter estimation with thomson's multiple window method. *Adaptive radar detection and estimation* 7: 381–459.

Du, K-L, AKY Lai, KKM Cheng, and MNS Swamy. 2002. Neural methods for antenna array signal processing: a review. *Signal Processing* 82(4):547–561.

EM Software & Systems-S.A. (Pty). 2014. *Release notes for FEKO suite 7.0*. www.feko.info.

Erentok, Aycan, and Richard W Ziolkowski. 2008. Metamaterial-inspired efficient electrically small antennas. *IEEE Transactions on Antennas and Propagation* 56(3): 691–707.

Fano, Robert M. 1950. Theoretical limitations on the broadband matching of arbitrary impedances. *Journal of the Franklin Institute* 249(1):57–83.

Ferrara, E, and T Parks. 1983. Direction finding with an array of antennas having diverse polarizations. *IEEE Transactions on Antennas and Propagation* 31(2):231–236.

Garbacz, RJ. 1965. Modal expansions for resonance scattering phenomena. *Proceedings of the IEEE* 53(8):856–864.

Garmatyuk, Dmitriy S, and Ram M Narayanan. 2002. ECCM capabilities of an ultrawideband bandlimited random noise imaging radar. *IEEE Transactions on Aerospace and Electronic Systems* 38(4):1243–1255.

Ghaemi, K., and N. Behdad. 2016. A low-profile, wideband antenna with vertically polarized directional radiation. *IEEE Antennas and Wireless Propagation Letters* 15: 1093–1096.

Ghaemi, Kasra, Ruyu Ma, and Nader Behdad. 2018. A small-aperture, ultrawideband HF/VHF direction finding system for unmanned aerial vehicles. *IEEE Transactions on Antennas and Propagation*.

Gohberg, Israel, Peter Lancaster, and Leiba Rodman. 1986. *Invariant subspaces of matrices with applications*. Philadelphia: SIAM Publications.

Gustafsson, Mats, Christian Sohl, and Gerhard Kristensson. 2007. Physical limitations on antennas of arbitrary shape. In *Proceedings of the royal society of london a: Mathematical, physical and engineering sciences*, vol. 463, 2589–2607. The Royal Society.

Guy, JRF, and DEN Davies. 1983. Studies of the adcock direction finder in terms of phase-mode excitations around circular arrays. *Radio and Electronic Engineer* 53(1):33–38.

Hansen, R. C. 1981. Fundamental limitations in antennas. *Proceedings of the IEEE* 69(2):170–182.

Harrington, R., and J. Mautz. 1971. Computation of characteristic modes for conducting bodies. *IEEE Transactions on Antennas and Propagation* 19(5):629–639.

Harrington, Roger F. 1960. Effect of antenna size on gain, bandwidth, and efficiency. *J. Res. Nat. Bur. Stand* 64(1):1–12.

Haykin, Simon, and KJ Ray Liu. 2010. *Handbook on array processing and sensor networks*, vol. 63. John Wiley & Sons.

Henault, S, S Rajan, R Inkol, S Wang, and YMM Antar. 2008. Impact of elevation angle variations in wideband adcock direction finders subject to mutual coupling. In *Antennas and propagation society international symposium, 2008. ap-s 2008. ieee*, 1–4. IEEE.

Holder, E. Jeff. 2014. *Angle-of-arrival estimation using radar interferometry: Methods and applications*. Edison, NJ: SciTech Publishing.

Hong, Wonbin, and Kamal Sarabandi. 2009. Low-profile, multi-element, miniaturized monopole antenna. *IEEE Transactions on Antennas and Propagation* 57(1): 72–80.

ITU Recommendation. 2017. Electrical characteristics of the surface of the earth. *ITU-R P. 527-4*.

Jenkins, Herndon H. 1991. *Small-aperture radio direction-finding*. Artech House on Demand.

Jin, P., and R. W. Ziolkowski. 2010. Metamaterial-inspired, electrically small huygens sources. *IEEE Antennas and Wireless Propagation Letters* 9:501–505.

Kathrein Scala. 2020. Kathrein-scala - cl7-300 - 225-400 9.5dbi log periodic antenna. https://www.neobits.com/kathrein_scala_cl7_300_225_400_9_5dbi_log_periodic_p9866177.html. [Online; accessed 07/29/2020].

Kawakami, H., and T. Ohira. 2005. Electrically steerable passive array radiator (espar) antennas. *IEEE Antennas and Propagation Magazine* 47(2):43–50.

Kelso, John M. 1972. Measuring the vertical angles of arrival of HF skywave signals with multiple modes. *Radio Science* 7(2):245–250.

Kishor, Krishna Kumar, and Sean Victor Hum. 2013. A two-port chassis-mode MIMO antenna. *IEEE Antennas and Wireless Propagation Letters* 12:690–693.

Kratschmer, G. 2010. Introduction into theory of direction finding. *Radiomonitoring and Radiolocation* 2011:2011.

Krim, Hamid, and Mats Viberg. 1996. Two decades of array signal processing research: the parametric approach. *IEEE signal processing magazine* 13(4):67–94.

Lee, MT, KM Luk, KW Leung, and MK Leung. 2002. A small dielectric resonator antenna. *IEEE Transactions on Antennas and Propagation* 50(10):1485–1487.

Li, Hui, Zachary Thomas Miers, and Buon Kiong Lau. 2014. Design of orthogonal MIMO handset antennas based on characteristic mode manipulation at frequency bands below 1 ghz. *IEEE Transactions on Antennas and Propagation* 62(5):2756–2766.

Li, Jian, and RT Compton. 1991. Angle and polarization estimation using ESPRIT with a polarization sensitive array. *IEEE Transactions on Antennas and Propagation* 39(9):1376–1383.

Li, M., and K. Luk. 2012. A wideband dual-polarized antenna with very low back radiation. In *2012 asia pacific microwave conference proceedings*, 61–63.

Li, Mingjian, and Nader Behdad. 2017. Dual-band platform-mounted HF/VHF antenna design using the characteristic mode theory. *IET Microwaves, Antennas & Propagation*.

Liang, X, and YWM Chia. 2001. New precision wideband direction finding antenna. *IEE Proceedings-Microwaves, Antennas and Propagation* 148(6):363–364.

Liberal, Iñigo, Diego Caratelli, and Alexander Yarovoy. 2011. Conformal antenna array for ultra-wideband direction-of-arrival estimation. *International Journal of Microwave and Wireless Technologies* 3(4):439–450.

Luk, K., and B. Wu. 2012. The magnetoelectric dipole—a wideband antenna for base stations in mobile communications. *Proceedings of the IEEE* 100(7):2297–2307.

Luk, Kwai-Man, and Hang Wong. 2006. A new wideband unidirectional antenna element. *Int. J. Microw. Opt. Technol.* 1(1):35–44.

M2 Antenna Systems. 2020. 225-400-8, 225-400 mhz spiral antenna. https://www.m2inc.com/FG2254008. [Online; accessed 07/29/2020].

Ma, CW, and CC Teng. 1999. Fuzzy neural network approach for 2-d direction finding in multipath environments. *IEE Proceedings-Radar, Sonar and Navigation* 146(2):78–83.

Ma, Ruyu, and Nader Behdad. 2018a. Design of platform-based HF direction finding antennas using the characteristic mode theory. In *Applied computational electromagnetics society symposium (aces), 2018 international*, 1–2.

———. 2018b. Design of platform-based hf direction-finding antennas using the characteristic mode theory. *IEEE Transactions on Antennas and Propagation* 67(3): 1417–1427.

———. 2020. Broadband, small-aperture direction-finding array with azimuth and elevation estimation capability. *IEEE Transactions on Antennas and Propagation* 68(4):3163–3175.

Manteuffel, D, and R Martens. 2016. Compact multimode multielement antenna for indoor UWB massive MIMO. *IEEE Transactions on Antennas and Propagation* 64(7):2689–2697.

Martens, Robert, Eugen Safin, and Dirk Manteuffel. 2011. Inductive and capacitive excitation of the characteristic modes of small terminals. In *Antennas and propagation conference (lapc), 2011 loughborough*, 1–4. IEEE.

Meloling, John H, John W Rockway, Michael P Daly, Aldo R Monges, Jeffery C Allen, W Rick Nielsen, P Michael McGinnis, Ronald B Thompson, and Nazia A

Mozaffar. 2016. A vector-sensing antenna system: A high-frequency, vector-sensing array based on the two-port loop antenna element. *IEEE Antennas and Propagation Magazine* 58(6):57–63.

Miers, Zachary, Hui Li, and Buon Kiong Lau. 2013. Design of bandwidth-enhanced and multiband MIMO antennas using characteristic modes. *IEEE Antennas and Wireless Propagation Letters* 12:1696–1699.

Mingjian Li, Nader Behdad, Ruyu Ma. 2018. A compact, low-cost UWB direction finding system using a switched beam antenna. *IEEE Antennas and Propagation Magazine*.

National Telecommunication and Information Administration. 2014. Federal government spectrum use reports 225 mhz to 5 ghz as of 11/14/2014. Tech. Rep. [Online; accessed 07/29/2020].

Noguchi, Keisuke, Shin-Ichi Betsudan, Takashi Katagi, and Motoo Mizusawa. 2003. A compact broad-band helical antenna with two-wire helix. *IEEE Transactions on Antennas and Propagation* 51(9):2176–2181.

Nordebo, Sven, Mats Gustafsson, and Jonas Lundback. 2006. Fundamental limitations for DOA and polarization estimation with applications in array signal processing. *IEEE Transactions on Signal Processing* 54(10):4055–4061.

Ojiro, Y., H. Kawakami, K. Gyoda, and T. Ohira. 2001. Improvement of elevation directivity for espar antennas with finite ground plane. In *Ieee antennas and propagation society international symposium. 2001 digest. held in conjunction with: Usnc/ursi national radio science meeting (cat. no.01ch37229)*, vol. 4, 18–21 vol.4.

Peavey, David, and Tokunbo Ogumfunmi. 1997. The single channel interferometer using a pseudo-doppler direction finding system. In *Acoustics, speech, and signal processing, 1997. icassp-97., 1997 ieee international conference on*, vol. 5, 4129–4132. IEEE.

Plapous, Cyril, Jun Cheng, Eddy Taillefer, Akifumi Hirata, and Takashi Ohira. 2004. Reactance domain music algorithm for electronically steerable parasitic array radiator. *IEEE Transactions on Antennas and Propagation* 52(12):3257–3264.

Pöhlmann, Robert, Siwei Zhang, Thomas Jost, and Armin Dammann. 2017. Power-based direction-of-arrival estimation using a single multi-mode antenna. *arXiv preprint arXiv:1706.09690*.

Preston, Stephanie L, David V Thiel, Trevor A Smith, Steven G O'Keefe, and Jun Wei Lu. 1998. Base-station tracking in mobile communications using a switched parasitic antenna array. *IEEE Transactions on Antennas and Propagation* 46(6):841–844.

Rahola, Jussi, and Jani Ollikainen. 2006. Optimal antenna placement for mobile terminals using characteristic mode analysis. In *Antennas and propagation, 2006. eucap 2006. first european conference on*, 1–6.

Ramos, Javier, Cherian P Mathews, and Michael D Zoltowski. 1999. FCA-ESPRIT: A closed-form 2-D angle estimation algorithm for filled circular arrays with arbitrary sampling lattices. *IEEE transactions on signal processing* 47(1):213–217.

Raza, H., A. Hussain, J. Yang, and P. Kildal. 2014. Wideband compact 4-port dual polarized self-grounded bowtie antenna. *IEEE Transactions on Antennas and Propagation* 62(9):4468–4473.

Remez, Jacob, and Erez Ben-Ari. 2009. Low-loss wideband multimodal interferometric antenna for DOA in azimuth and elevation. *IEEE antennas and wireless propagation letters* 8:898–902.

Rissanen, Jorma. 1978. Modeling by shortest data description. *Automatica* 14(5): 465–471.

Roy, Richard, and Thomas Kailath. 1989. ESPRIT-estimation of signal parameters via rotational invariance techniques. *IEEE Transactions on acoustics, speech, and signal processing* 37(7):984–995.

Rzymowski, M., P. Woznica, and L. Kulas. 2016. Single-anchor indoor localization using espar antenna. *IEEE Antennas and Wireless Propagation Letters* 15:1183–1186.

San Antonio, Geoffrey, William W Lee, and Mark Parent. 2013. High frequency vector sensor design and testing. In *Radio science meeting (usnc-ursi nrsm), 2013 us national committee of ursi national*, 1–1. IEEE.

Schlub, R., Junwei Lu, and T. Ohira. 2003. Seven-element ground skirt monopole espar antenna design from a genetic algorithm and the finite element method. *IEEE Transactions on Antennas and Propagation* 51(11):3033–3039.

Schlub, R., and D. V. Thiel. 2004. Switched parasitic antenna on a finite ground plane with conductive sleeve. *IEEE Transactions on Antennas and Propagation* 52(5): 1343–1347.

Schlub, Robert, and David V Thiel. 2004. Switched parasitic antenna on a finite ground plane with conductive sleeve. *IEEE Transactions on antennas and propagation* 52(5):1343–1347.

Schmidt, Ralph. 1986. Multiple emitter location and signal parameter estimation. *IEEE transactions on antennas and propagation* 34(3):276–280.

Schwarz, Gideon, et al. 1978. Estimating the dimension of a model. *The annals of statistics* 6(2):461–464.

Seo, H., and A. A. Kishk. 2011. Wideband linear and dual-polarized antenna based on huygens' source principle. In *2011 xxxth ursi general assembly and scientific symposium*, 1–4.

Shieh, Ching-Sung, and Chin-Teng Lin. 2000. Direction of arrival estimation based on phase differences using neural fuzzy network. *IEEE Transactions on antennas and propagation* 48(7):1115–1124.

Shih, Ting-Yen, and Nader Behdad. 2016. Bandwidth enhancement of platform-mounted HF antennas using the characteristic mode theory. *IEEE Transactions on Antennas and Propagation* 64(7):2648–2659.

———. 2017. Design of vehicle-mounted, compact VHF antennas using characteristic mode theory. In *Antennas and propagation (eucap), 2017 11th european conference on*, 1765–1768.

Sievenpiper, Daniel F, David C Dawson, Minu M Jacob, Tumay Kanar, Sanghoon Kim, Jiang Long, and Ryan G Quarfoth. 2011. Experimental validation of performance limits and design guidelines for small antennas. *IEEE Transactions on Antennas and Propagation* 60(1):8–19.

Slater, Matthew J, Christopher D Schmitz, Michael David Anderson, Douglas L Jones, and Jennifer T Bernhard. 2013. Demonstration of an electrically small antenna array for UHF direction-of-arrival estimation. *IEEE Transactions on Antennas and Propagation* 61(3):1371–1377.

Steiner, F. 1960. Wide-base doppler very-high-frequency direction finder. *IRE Transactions on Aeronautical and Navigational Electronics* (3):98–105.

Stuart, Howard R, and Steven R Best. 2008. A small wideband multimode antenna. In *Antennas and propagation society international symposium, 2008. ap-s 2008. ieee*, 1–4. IEEE.

Sun, Chen, Akifumi Hirata, Takashi Ohira, and Nemai C Karmakar. 2004. Fast beamforming of electronically steerable parasitic array radiator antennas: Theory and experiment. *IEEE Transactions on Antennas and Propagation* 52(7):1819–1832.

Svantesson, Thomas. 2000. Multimode based direction finding. In *Signals, systems and computers, 2000. conference record of the thirty-fourth asilomar conference on*, vol. 1, 595–599. IEEE.

Taillefer, E., A. Hirata, and T. Ohira. 2005. Direction-of-arrival estimation using radiation power pattern with an espar antenna. *IEEE Transactions on Antennas and Propagation* (2):678–684.

Taillefer, Eddy, Akifumi Hirata, and Takashi Ohira. 2005. Direction-of-arrival estimation using radiation power pattern with an ESPAR antenna. *IEEE Transactions on Antennas and Propagation* 53(2):678–684.

Taillefer, Eddy, Wataru Nomura, Jun Cheng, Makoto Taromaru, Yoichiro Watanabe, and Takashi Ohira. 2008. Enhanced reactance-domain ESPRIT algorithm employing multiple beams and translational-invariance soft selection for direction-of-arrival estimation in the full azimuth. *IEEE Transactions on Antennas and Propagation* 56(8):2514–2526.

Tang, M., H. Wang, and R. W. Ziolkowski. 2016. Design and testing of simple, electrically small, low-profile, huygens source antennas with broadside radiation performance. *IEEE Transactions on Antennas and Propagation* 64(11):4607–4617.

Tang, M., B. Zhou, and R. W. Ziolkowski. 2017. Low-profile, electrically small, huygens source antenna with pattern-reconfigurability that covers the entire azimuthal plane. *IEEE Transactions on Antennas and Propagation* 65(3):1063–1072.

Tayem, Nizar, and Hyuck M Kwon. 2005. L-shape 2-dimensional arrival angle estimation with propagator method. *IEEE transactions on antennas and propagation* 53(5):1622–1630.

Terman, Frederick Emmons. 1955. Electronic and radio engineering.

Travers, Douglas N, and Stuart M Hixon. 1966. Abstracts of the available literature on radio direction finding 1899-1965. Tech. Rep., Southwest Research Inst. San Antonio TX.

Van Veen, Barry D, and Kevin M Buckley. 1988. Beamforming: A versatile approach to spatial filtering. *IEEE assp magazine* 5(2):4–24.

Weiss, Anthony J, and Benjamin Friedlander. 1991. Performance analysis of diversely polarized antenna arrays. *IEEE Transactions on Signal Processing* 39(7): 1589–1603.

Wolff, Christian. 2017. Radar Basics - UWB-Radar. `http://www.radartutorial.eu/02.basics/UWB%20Radar.en.html`. [Online; accessed 11/16/2017].

Wong, H., K. Mak, and K. Luk. 2008. Wideband shorted bowtie patch antenna with electric dipole. *IEEE Transactions on Antennas and Propagation* 56(7):2098–2101.

Wong, Kainam T, and Michael D Zoltowski. 1997. Uni-vector-sensor ESPRIT for multisource azimuth, elevation, and polarization estimation. *IEEE Transactions on Antennas and Propagation* 45(10):1467–1474.

———. 2000. Closed-form direction finding and polarization estimation with arbitrarily spaced electromagnetic vector-sensors at unknown locations. *IEEE Transactions on Antennas and Propagation* 48(5):671–681.

Yaghjian, Arthur D, and Steven R Best. 2005. Impedance, bandwidth, and Q of antennas. *IEEE Transactions on Antennas and Propagation* 53(4):1298–1324.

Yang, Dan, and Venkataramana Ajjarapu. 2007. Critical eigenvalues tracing for power system analysis via continuation of invariant subspaces and projected arnoldi method. *IEEE Transactions on Power Systems* 22(1):324–332.

Yang, J., and A. Kishk. 2012. A novel low-profile compact directional ultra-wideband antenna: The self-grounded bow-tie antenna. *IEEE Transactions on Antennas and Propagation* 60(3):1214–1220.

Yee, A, and R Garbacz. 1973. Self-and mutual-admittances of wire antennas in terms of characteristic modes. *IEEE Transactions on Antennas and Propagation* 21(6):868–871.

Zoltowski, Michael D, Martin Haardt, and Cherian P Mathews. 1996. Closed-form 2-D angle estimation with rectangular arrays in element space or beamspace via unitary ESPRIT. *IEEE Transactions on Signal Processing* 44(2):316–328.

Zoltowski, Michael D, and Kainam Thomas Wong. 2000. ESPRIT-based 2-d direction finding with a sparse uniform array of electromagnetic vector sensors. *IEEE Transactions on Signal Processing* 48(8):2195–2204.